University of Antwerp

Modelling *in vitro* cancer treatment with a plasma jet

simulations on macro- and microscopic scale

Thesis submitted for the degree of
Doctor of Science: Chemistry
at the University of Antwerp
to be defended by

Pepijn Heirman

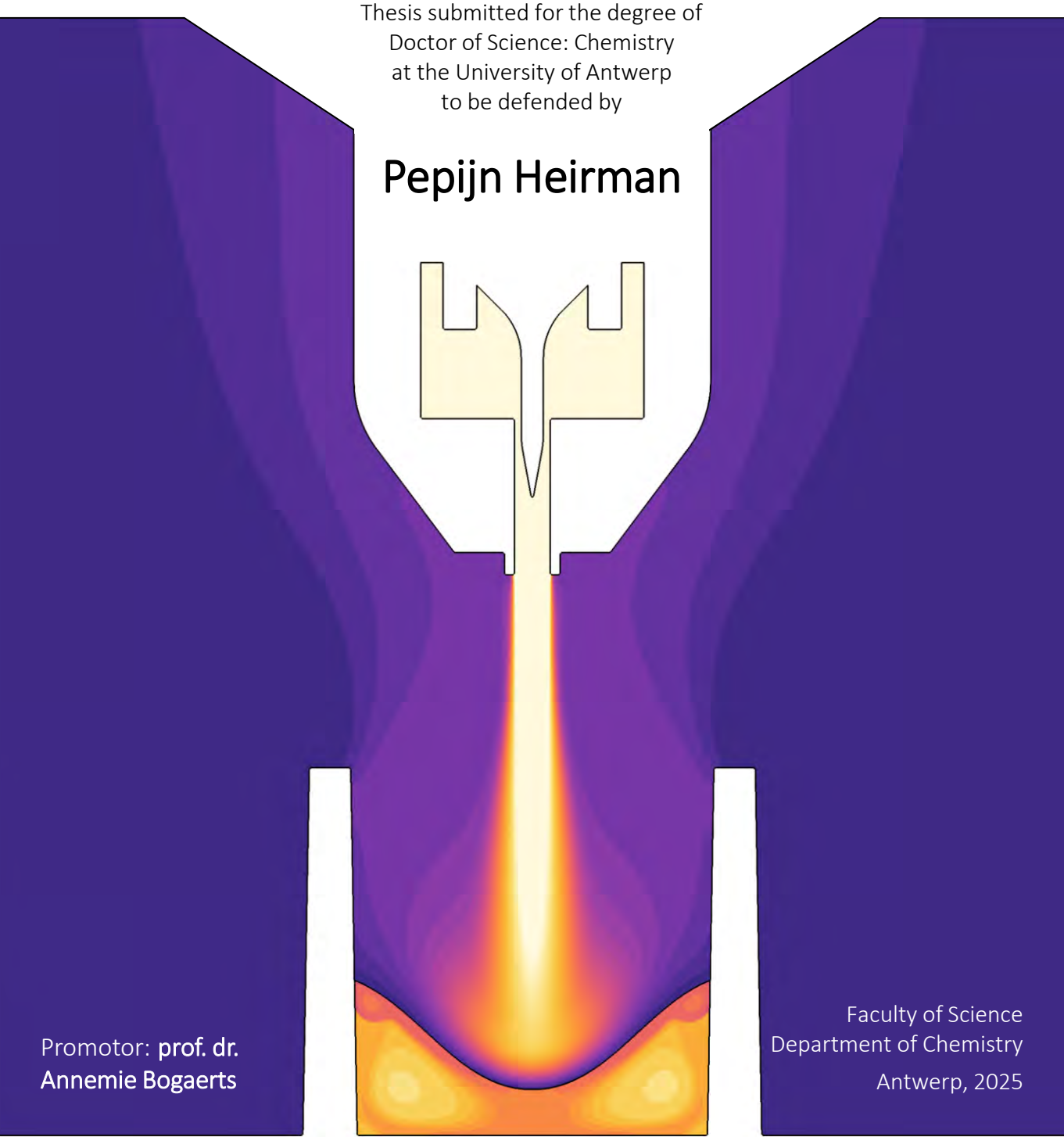

Promotor: **prof. dr. Annemie Bogaerts**

Faculty of Science
Department of Chemistry

Antwerp, 2025

Faculteit Wetenschappen
Departement Chemie

Modelling *in vitro* cancer treatment with a plasma jet: simulations on macro- and microscopic scale

Proefschrift voorgelegd tot het behalen van de graad

Doctor in de Wetenschappen: Chemie

Aan de Universiteit Antwerpen

Te verdedigen door

Pepijn Heirman

Promotor:
prof. dr. Annemie Bogaerts

Antwerpen, 2025

De doctoraatsonderzoeker en promotor verklaren dat het doctoraatsonderzoek werd uitgevoerd volgens de principes van de wetenschappelijke integriteit, zoals vermeld in het algemeen doctoraatsreglement en algemeen charter van de doctorandus van UAntwerpen en het integriteitscharter voor doctorandi en promotoren verbonden aan de Universiteit Antwerpen.

Dutch title: Modelleren van *in vitro* kankerbehandeling met een plasmajet: simulaties op macro- en microscopische schaal.

Het onderzoek in deze thesis werd gefinancierd door FWO (Grant ID 1100421N)

For part of this thesis, computational resources and services were provided by the HPC core facility CalcUA (Universiteit Antwerpen), and VSC (Flemish Supercomputer Center).

Universiteit Antwerpen
Faculteit Wetenschappen
Groenenborgerlaan 171, 2610, Antwerpen, België

Onderzoekgroep PLASMANT
Plasma Lab for Applications in Sustainability and Medicine – ANTwerp

Members of the Jury

Chair

Prof. dr. Erik Neyts
Modelling and Simulation in Chemistry (MOSAIC)
University of Antwerp, Belgium

Promotor

Prof. dr. Annemie Bogaerts
Plasma Lab for Applications in Sustainability and Medicine – Antwerp (PLASMANT)
University of Antwerp, Belgium

Members

Prof. dr. Siegfried Denys
Antwerp engineering, photoelectrochemistry and sensing (A-PECS)
University of Antwerp, Belgium

Prof. dr. Evelien Smits
Center for Oncological Research (CORE)
University of Antwerp, Belgium

Prof. dr. Jan Van Dijk
Elementary Processes in Gas Discharges (EPG)
Eindhoven University of Technology, The Netherlands

Dr. Eric Robert
Research Group on the Energetics of Ionized Media (GREMI)
University of Orléans, France

Dr. Kristian Wende
Leibniz Institute for Plasma Science and Technology (INP)
Greifswald, Germany

Summary

Research into new or improved cancer treatments forms a large and important field in science. Indeed, despite the broad range of available treatments, mortality in cancer patients remains high, as do the side effects of current treatment methods. Since the discovery, almost 30 years ago, that cold atmospheric plasma (CAP) can inactivate bacteria, research in the field of plasma medicine has expanded into a wide range of possible biomedical applications. This includes research into various strategies to treat cancer, as CAP was shown later to both have the ability to kill cancer cells as well as induce an immune response against them. While much progress is made with *in vivo* studies, which are crucial to progress the field to a clinical setting, *in vitro* research remains the basis on which understanding of the possible effects of plasma treatment on cells is built. Beyond experiments, computer simulations can provide fundamental insight into underlying mechanisms that are out of reach with experimental methods.

In this thesis, we develop a 2D-axisymmetric fluid model, to investigate the transport phenomena that occur during the treatment of a well plate with a plasma jet, as commonly done for experimental *in vitro* research.

By applying this model to investigate how different setup geometries may influence the treatment, more specifically the chosen well type and the use of a gas shield around the plasma jet, we find that this choice has a substantial effect. Our focus for this lies on the mixing of the plasma jet effluent with the ambient N_2, O_2 and H_2O, which drives formation of the reactive species in the plasma that act as the main effectors of CAP treatment. While the well type determines the amount of ambient gas that mixes with the effluent, a gas shield causes a mixing behaviour that differs from that when the jet operates in open air. These are important insights to consider, especially with increasing attention for standardisation and comparability of experimental work in the field. Indeed, a lack of uniformity in literature can make results difficult to directly compare to one another.

Building on these findings, we perform a systematic study on the effect of the design of a shielding gas device, as many different designs have been depicted in literature since its introduction into the field. These simulations show that not only do specific design parameters of the gas shield significantly change the conditions in the plasma effluent, the efficacy in shielding the effluent from the ambient (i.e., the original intent of a gas shield) is also affected, leading to some designs that do not function as intended at all.

Apart from investigating transport phenomena in the gas phase, we also apply our model to investigate the transport of reactive species from the gas phase to the treated liquid. Many different boundary conditions have been used in various published multidimensional plasma-liquid models to describe dissolution of reactive species into a treated liquid. However, we discover that none of these interfacial boundary conditions are able to reproduce experimental measurements for all relevant species. Specifically, we find that accuracy strongly depends on the solubility of the species in question. Consequently, we propose a first step toward a more accurate description of this phenomenon by combining film theory with the mass accommodation coefficient.

Finally, while the 2D-axisymmetric fluid model can simulate the physical phenomena that occur in the studied system, and allows us to study to what degree the treatment might be affected by various parameters, such a modelling approach is not suitable to elucidate the actual, biological effects that plasma treatment may induce in treated (cancer) cells. To gain insight into such effects, we may instead use molecular dynamics simulations, as done for the final part of this thesis. Specifically, we focus on the immunotherapeutic potential of CAP treatment by modelling the effect of CAP-induced oxidation on HLA-E and HLA-Cw4, two protein ligands that are important for the crosstalk between cancer cells and natural killer (NK) cells. By comparing our simulations to experimental results, this data demonstrates the complex chemical and biological interactions between CAP and cancer cells, with regard to NK cell recognition, and provides an interesting starting point for further research.

Taken together, the findings presented in this thesis provide a deeper insight into the *in vitro* treatment of cancer cells with a plasma jet on both a macroscopic and microscopic scale. We investigate various ways in which the chosen setup geometry can influence the treatment itself. It is important to keep these effects in mind as a source of variation in experiments, along with other determining parameters, both when conducting experiments and when comparing them among each other. Moreover, the importance of benchmarking and comparison between computational results is underlined. Finally, we shed some light onto the immunotherapeutic potential of CAP treatment, and point toward possible paths for future research.

Samenvatting

Onderzoek naar nieuwe of verbeterde kankerbehandelingen vormt een groot en belangrijk wetenschappelijk onderzoeksveld. Ondanks de brede waaier aan beschikbare behandelingen, blijft sterfte onder kankerpatiënten immers hoog, en geven de behandelingsmethoden significante bijwerkingen. Sinds de ontdekking, intussen bijna 30 jaar geleden, dat koud atmosferisch plasma bacteriën onschadelijk kan maken, is onderzoek in het veld van plasmageneeskunde gegroeid tot een breed spectrum van mogelijke biomedische toepassingen. Dit omvat, onder andere, onderzoek naar verschillende strategieën om kanker te behandelen, aangezien aangetoond werd dat plasmabehandeling zowel in staat is kankercellen te doden alsook een immuunreactie tegen hen op te wekken. Er wordt veel vooruitgang geboekt in dit onderzoeksveld aan de hand van *in vivo* studies, dewelke cruciaal zijn voor de klinische vooruitgang van deze behandeling. Toch blijft *in vitro* onderzoek aan de basis liggen van het bestuderen welke mogelijke effecten plasmabehandeling heeft op behandelde cellen. Op zijn beurt kunnen computersimulaties ons fundamenteel inzicht geven in de onderliggende mechanismen van deze behandeling die niet verkregen kunnen worden met experimentele methoden.

In deze thesis ontwikkelen we een 2D-axisymmetrisch vloeistofdynamica model, met als doel het onderzoeken van de transportfenomenen die voorkomen tijdens de behandeling van een wellplaat met een plasma jet, zoals typisch gedaan wordt tijdens *in vitro* onderzoek.

Met dit model onderzoeken we hoe een verschil in de geometrie van de behandelingsopstelling de behandeling kan beïnvloeden, meer specifiek het gekozen type wellplaat en het al dan niet gebruiken van een gasschild. Hierbij vinden we dat deze keuzes een substantieel effect hebben. Onze focus ligt hier bij de vermenging van het effluent van de plasma jet met de N_2, O_2 en H_2O in de omgevingslucht, hetgeen de vorming van reactieve deeltjes veroorzaakt die verantwoordelijk zijn voor de effecten van de behandeling. We vinden zo dat het gekozen type wellplaat bepaalt hoeveel gas er met het effluent kan mengen, terwijl een gasschild de grootte van deze vermenging verandert ten opzichte van wanneer de jet zich simpelweg in de omgevingslucht bevindt. Deze inzichten zijn belangrijk om in het achterhoofd te houden, zeker aangezien standaardisatie en vergelijkbaarheid van experimenteel werk recent meer aandacht krijgen in het veld. Het rechtstreeks vergelijken van resultaten wordt immers bemoeilijkt door een gebrek aan overeenstemming tussen experimentele methoden.

Voortbouwend op deze bevindingen onderzoeken we systematisch wat het effect is van het ontwerp van een gasschild, aangezien sinds de introductie van het gebruik hiervan in het veld er al verschillende ontwerpen in de literatuur zijn weergegeven. Deze simulaties tonen dat het specifieke ontwerp van het gasschild niet alleen de omstandigheden in het effluent van de plasma jet sterk kan beïnvloeden, maar ook de effectiviteit waarmee het gasschild het plasma van de omgevingslucht afschermt. Dat laatste is immers het originele doeleinde van het gebruik van een gasschild, terwijl we hier vinden dat sommige ontwerpen niet werken zoals bedoeld.

Naast het onderzoeken van transportfenomenen in de gasfase, passen we ons model ook toe om het transport van reactieve deeltjes van het gas naar de vloeistoffase te bestuderen. In verschillende gepubliceerde modellen voor plasma-vloeistof interactie worden andere formules gebruikt om de oplossing van reactieve deeltjes in de behandelde vloeistof te beschrijven. We ontdekken echter dat geen van de geteste formules in staat zijn om experimentele metingen te reproduceren voor alle relevante moleculen. Specifiek vinden we dat hun accuraatheid sterk afhangt van de oplosbaarheid van elke specifieke molecule. We stellen hier bijgevolg een eerste stap voor naar een meer accurate beschrijving van dit transport, gebaseerd op de combinatie van filmtheorie en de massa-accommodatie coëfficiënt.

Ten slotte, hoewel ons vloeistofdynamica model de fysische fenomenen die in het bestudeerde systeem voorkomen kan simuleren, en het ons toelaat te onderzoeken hoe de behandeling beïnvloed kan worden door verschillende parameters, kan deze computationele techniek geen informatie verschaffen over de eigenlijke, biologische effecten van de plasmabehandeling. Om hier inzicht in te krijgen, kunnen we in plaats daarvan gebruik maken van moleculaire dynamica. Dit doen we hier voor het laatste deel van deze thesis. Specifiek focussen we op het immunotherapeutische potentieel van plasmabehandeling door te onderzoeken hoe door plasma veroorzaakte oxidatie twee proteïnen beïnvloedt die belangrijk zijn voor de communicatie tussen kankercellen en NK-cellen, namelijk de proteïnen HLA-E en HLA-Cw4. Door onze simulaties te vergelijken met experimentele resultaten, demonstreren we de complexe chemische en biologische interactie tussen plasma en kankercellen, wat betreft de herkenning van kanker door NK-cellen. Deze resultaten bieden een interessant startpunt voor toekomstig onderzoek.

Alles samen presenteren de bevindingen in deze thesis een dieper inzicht in de *in vitro* behandeling van kankercellen met een plasma jet op zowel macroscopische als microscopische schaal. We onderzoeken verschillende manieren waarop de geometrie

van de gekozen opstelling de behandeling zelf kan beïnvloeden, hetgeen samen met andere bepalende parameters belangrijk is om in gedachten te houden bij zowel het uitvoeren als vergelijken van experimenten. Ook benadrukken we het belang van validatie en vergelijking van computationele resultaten. Ten slotte verkrijgen we meer inzicht in het immunotherapeutische potentieel van plasmabehandeling, met duidelijke paden voorwaarts voor toekomstig onderzoek.

Acknowledgements

This PhD has been a … turbulent time in my life. Starting it during a lockdown amidst a global pandemic did not provide the smoothest start, and many unexpected turns and troubles followed in the years after, though I suppose this can be said about most PhD's (well, maybe not the pandemic part). I have learned many things during my time as a PhD student. Things about myself, about science, and about (you guessed it) modelling *in vitro* treatment with a plasma jet. Before getting into the latter, though, I want to take a moment to acknowledge those who have helped and supported me.

First, I owe many thanks to my promotor. Annemie, thank you for giving me the opportunity to do research in PLASMANT, ever since my bachelor's thesis, and for your continuing encouragement. How you prioritize your students amidst your overflowing schedule is truly exemplary, even though none of us know how you do it (a secret twin remains my favourite theory).

While I will thank many amazing people in these acknowledgements, let's start with those that directly shaped my research. Ivan, thank you for your critical mindset and your drive to do good science. Robin, though our research areas are about as far from each other as possible within PLASMANT, you offered a fresh perspective on difficult questions on many occasions. Rani, your feedback on pretty much all my work has been invaluable in shaping my vision and writing. Maksud, thank you for teaching me the ins and outs of modelling proteins, with which I had no prior experience. I also want to thank Yury, Abraham, Stein, Erik, Kristian and Evelien, with whom I have had interesting discussions that changed my perspective.

I also want to acknowledge the members of PLASMANT, past and present, that make the group such a bright spot, even if (still) confined to a crumbling building. Thanks to Colin, for your contagious energy; Sarah, who went from pipsqueak bachelor student in my first year to competent PhD researcher; Elli, who I hereby formally forgive for leaving our office; Callie, for providing a welcome occasional change of scenery at BlueApp; and Joran, for realizing that organizing a mentoring system is indeed a two-person job. Thanks to Eduardo, Greg, Omar, Kristof, Elise, Eline, Senne, Rani, Joachim, Bjorn, Hamid, Kevin, Josh, Bart, Helder, Cédric, Stijn, Rubén, Christine, Matthias, Lisa H, Sara, Priyanka, Cecilia, Mac, Shangkun, and many others. While mostly spared from the crumbling B-building, but equally bright, I also want to thank the plasma-onco team: Angela, Ruben, Hanne, Mauranne, Jana and Lisa VDH.

Arriving to the people outside of PLASMANT, I want to start with thanking my family. Moeke, vake, bedankt voor jullie voortdurende steun. Ik ben tijdens mijn doctoraat dan wel permanent uit huis gegaan (wat de beestenboel thuis misschien iets rustiger gemaakt heeft), mijn wekelijkse bezoek heeft me toch steeds van een anker aan vroeger voorzien. Jelien, bedankt om steeds te checken hoe het met me gaat. Jij weet als geen ander het belang om hierbij stil te staan. Pascal, jij en Frank drukken een grote stempel op mijn leven, en dit zal altijd zo blijven.

Thank you to my friends from chemistry: Marjo, Rani, Robin, Wouter, Dries, Roel. We may have often been caught up in the troubles of our own PhD, but our group has provided the perfect environment for us to vent, because we really understand. Thank you as well to my amazing friends outside of chemistry. Thanks to Maarten, for always asking how things were going in my PhD even though you already knew; Mattias and Christophe, for always paying your taxes (money well spent if you ask me); and Hans, for your spontaneous calls and enthusiasm. Thank you, Julie, Eline and Rani, for graciously listening to me and those four Paljaskis telling every story for probably the tenth time. Thanks to Sophie, for reminding me that there are other things to talk about beside science; Tom and Nick, for the many drinks and for having been there for me basically forever; and Nils and Evita, for still finding the time to regularly see each other despite busy schedules and considerable distance.

Rani, as evident from the previous, you have been there for me as a co-worker, classmate, friend, and basically as the most important person in my life. Thank you for your never-ending support, your love, your good advice, and your natural ability to make me strive to always be a better version of myself.

Finally, thank you to whoever is reading this. Chances are high I already mentioned you in these acknowledgements (how many people randomly read a PhD thesis, especially the acknowledgements?). If not, I thank you here, and hope that you find what you are looking for in this thesis.

What do you mean, accounting

for Hofstadter's Law twice doesn't solve it?

Table of Contents

Chapter 1

General introduction

1. A brief introduction to plasma

Plasma is a (partially) ionised gas that is electrically conductive and exhibits collective behaviour. It is a complex, highly reactive mixture of ions and electrons, as well as various atoms, radicals and molecules in both their ground and excited states. Deexcitation of the latter causes the emission of photons, including visible light. A plasma is by definition quasi-neutral, which means that the positive and negative charges are balanced [1].

Plasma can be created by heating a gas to such a degree that the kinetic energy is able to overcome the binding energy between electrons and their atoms. In this regard, plasma can be seen as a "fourth phase" of matter, after the solid, liquid and gaseous phase that we are used to. In fact, there are several examples of plasmas in nature, such as the sun, lightning, and the auroras. Apart from by heating a gas, plasmas can also be created through photoionization, or by applying a sufficiently strong electric field across the gas. In the latter case, which causes a so-called "gas breakdown" or "gas discharge", the electric field will accelerate free electrons towards the positive anode. As a result, the electrons collide with gas molecules causing excitation, dissociation and ionisation, giving rise to more free electrons. Because these free electrons have a mass that is far lower than the heavier ions (a hydrogen ion, the lightest possible ion, is still 1836 times heavier than an electron), they are accelerated by the electric field much more easily, causing them to quickly gain much more energy. The electrons will transfer part of this energy to the heavier particles via elastic collisions but, again because of their small mass, this is an inefficient process. As a result, gas discharge plasmas are often not in local thermodynamic equilibrium, i.e., the electron temperature remains far higher than the gas temperature. A specific case, which can be achieved at low gas density or with a small distance between the electrodes, is one where the electron temperature is on the order of 10 000 K, while the gas temperature remains around room temperature [1]. In this case, the plasma is often referred to as a non-thermal plasma (NTP). When NTP is generated at atmospheric pressure, it is often also termed a cold atmospheric plasma (CAP).

Plasma has long been employed in technological applications for its physical properties, such as its heat, in welding [2] or wound cauterization [3], or its luminosity, in lamps [4]. More recently, plasma is the subject of research in various fields of applications based on its rich chemical properties (although also here there are examples of long-established industrial applications, such as ozone production [5]). Prime examples are

the use of plasma to convert otherwise stable molecules into useful products, such as nitrogen fixation [6] or CO_2 conversion [7], and the production of reactive species for water purification [8] or applications in medicine, such as the healing of wounds [9] or the treatment of cancer [10]. It is this last example that forms the main background of the research done in this thesis, specifically the use of CAP for cancer treatment. Before we dive into the concepts of this field, however, it is useful to understand the range of diseases we know as cancer.

2. Cancer and the immune system

Cancer is a large group of diseases characterised by unregulated cell growth and the ability to invade the rest of the body via so-called metastasis [11]. Currently, over 200 different types of cancer have been encountered. With almost 10 million deaths in 2020, the year I started the research for this thesis, it remains one of the leading causes of death worldwide [12].

Abnormal gene expression or dysfunction in DNA repair mechanisms can cause the cells in our body to develop mutations. These mutations accumulate over time, and can eventually cause the cell to become malignant and develop into a tumour [11]. The typical capabilities acquired by cells, through mutations, during human tumour development are defined as the hallmarks of cancer, with the original six coined by Hannahan and Weineberg in the year 2000 [13]. Further research over the past two decades has significantly increased our understanding of cancer development [14, 15], leading to the (currently) 14 defined hallmarks shown in Figure 1-1. Different types of cancer can develop from different cell types and in different places in the body, leading to different characteristics. Consequently, a uniform treatment does not exist and instead treatment must be tuned for each specific case [11].

A broad range of therapies are currently used for the treatment of cancer, apart from surgery, and can generally be divided into either local or systemic treatments [16]. Local treatments include radiotherapy [17], which exposes the tumour to a high dose of ionizing radiation to cause fatal genetic damage, and photodynamic therapy [18], where light is used to activate a photosensitizing agent to produce singlet oxygen that kills nearby cells. Systemic treatments rely mostly on the administration of drugs like in chemotherapy [19], where chemicals inflict genetic damage to rapidly dividing cells such

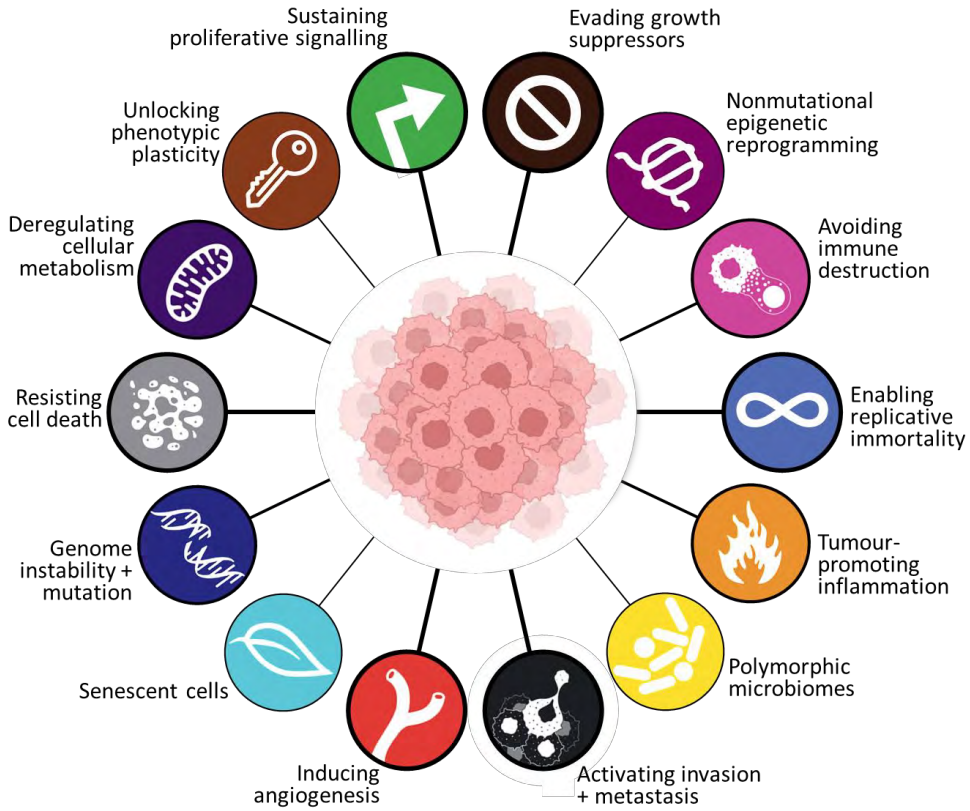

Figure 1-1. The hallmarks of cancer.

as cancer cells, and targeted therapies and hormone therapy [20], where drugs target specific biological pathways on which the cancer cells rely for survival. Systemic treatments have the advantage of acting in the entire body and can thus also target metastases. At the same time, this means that these treatments are usually accompanied by more severe side effects, e.g. infamously the fact that chemotherapy also targets healthy rapidly dividing cells such as hair follicles and hematopoietic cells in the same way as it does cancer cells. Despite the broad range of available treatments, mortality in cancer patients remains high. Combined with the desire to reduce side effects, research into new or improved cancer treatments is a massive field in (medical) science. The most recent breakthrough in the field has been the development of immunotherapy, a systemic therapy which aims to harness the body's own immune system to target and destroy cancer cells [21].

In reality, the mutations that can eventually lead to cancer happen in the body on a nearly constant basis. Because of this, we naturally produce an immune response against developing tumours [11, 22]. Indeed, similar to cells infected by a virus, our immune system can recognise and eliminate malignantly transformed cells. Almost all cells express major histocompatibility complex class 1 (MHC-I) molecules on their surface. These protein complexes present peptides from within the cell. Abnormal peptides that point to malignant transformation will be recognised by antigen-specific T cells, causing their activation against the cancer cell [22]. At the same time, natural killer (NK) cells screen for the presence of MHC-I itself. Unlike antigen-specific T cells, NK cells express invariant receptors on their surface and rely for their activation on a balance between activating and inhibiting signals received from binding of these receptors to ligands on the target cell membrane [23]. MHC-I is an important category of inhibiting ligands. Mutations that lead a cancer cell to downregulate MHC-I (a so-called "missing self"), which would prevent recognition by T-cells, are thus detected by NK cells, leading to their activation. Alternatively, NK cells can also be activated by an increase in activating signals provided by the expression of stress-induced proteins on the cancer cell surface (also called a "stress-induced self") [24, 25]. After activation, NK cells can kill cancer cells directly (hence their name), without prior proliferation or the need for an already initiated immune response [23].

Despite this immunosurveillance against arising tumours, some cancer cells can learn to evade the immune system [26]. Indeed, evasion of immune destruction is an important hallmark of cancer (see Figure 1-1). Thus, it is the goal of immunotherapy to reactivate or improve the body's immune response against cancer. As we will see, the potential of treatment with CAP to provide an immunotherapeutic effect has become an important topic in the field in recent years. In the next section, let us trace how the field of plasma medicine arrived to recognizing this potential.

3. Plasma medicine

In 1996, research by M. Laroussi at the Plasma Science Laboratory of the University of Tennessee showed that bacteria could be inactivated by exposing them to CAP [27]. This work spawned a research program mainly focused on disinfection and treatment of wounds of injured soldiers [28], and later research expanded to the effect of CAP on mammalian cells with envisioned applications such as microsurgery and tissue removal [29, 30]. Then, in 2006, Fridman *et al.* [31] found that treatment with CAP was able to kill cancer cells, specifically melanoma cells, *in vitro*. This was followed by reports on similar effects for different cancer cell types [32] and, importantly, the first report on the *in vivo* anti-cancer effect of CAP treatment, by Vandamme *et al*. [33].

From this research grew the field that is currently known as plasma medicine, which investigates the interaction between CAP and cells or tissue, with as its main applications sterilisation [34], wound healing [9, 35] and, most relevant for the context of this thesis, cancer treatment.

3.1 RONS as the treatment effectors

Much of the research regarding plasma for cancer treatment, also referred to as plasma oncology, has been centred around the cytotoxic effects of plasma. Indeed, many studies have shown that CAP is able to kill cancer cells and/or stop tumour growth [32]. The general consensus is currently that the main contributors to the biological effects of plasma treatment, at least *in vitro*, are the reactive oxygen and nitrogen species (RONS) produced by the plasma [36, 37]. This is the case not only for the cytotoxic effects that have mainly been studied for plasma-based cancer treatment (as well as sterilisation), but also for the stimulatory effects that form the subject of research in plasma for wound healing. Other, physical properties of CAP, such as the electric fields and UV radiation generated by the plasma, likely play a role as well but are generally considered of minor importance. The fact that plasma-produced RONS can cause both stimulatory (for wound healing) and cytotoxic (for cancer treatment and sterilisation) effects may seem counterintuitive at first. This is because exposure to RONS follows the principle of hormesis [38, 39]: exposure of a biological system to low doses of stress or changing environmental factors can cause stimulatory effects, while higher doses of those same factors cause inhibitory effects or even toxicity [40].

A wide range of RONS is produced by CAP devices [37], including hydrogen peroxide (H_2O_2), hydroxyl radicals (OH), ozone (O_3), singlet oxygen ($^1O_2$), atomic oxygen (O) and

superoxide anions (O_2^-), which can be classified as reactive oxygen species (ROS), and nitrite (NO_2^-), nitrate (NO_3^-), nitric oxide (NO) and nitrogen dioxide (NO_2), in turn classified as reactive nitrogen species (RNS). RONS can in general be subdivided into long-lived (stable species, such as H_2O_2) and short-lived (species that quickly react away, such as O_2^-). Many of these species are already present in the body. Various RONS are involved in diverse biological processes, including functioning as messenger molecules [41]. In addition, these reactive species play a pivotal role in inflammation and immune cell functioning [38, 42, 43].

3.2 Plasma oncology

In the first decade of plasma oncology research, there were many optimistic studies claiming that treatment with CAP is a selective treatment [44, 45], i.e. that while cancer cells are killed by the treatment, healthy cells are left unharmed. The main explanation for this has been that cancer cells already have a higher intracellular level of ROS compared to healthy cells due to (i.a.) their elevated metabolism [46], and are thus less resistant to the additional oxidative stress induced by the plasma treatment [47]. Other possible explanations were centred around the higher proliferation rate of cancer cells, making them more susceptible to extensive DNA damage [47], a higher expression of aquaporins (i.e. transport channels in the cell membrane) through which RONS can enter the cell [48], and the lower cholesterol content in cancer cell membranes, which facilitates pore formation [49, 50]. In addition, a correlation with redox-regulating enzymes was proposed [51].

However, the view of plasma treatment as a selective cancer treatment has since shifted [36]. Indeed, a retrospective analysis by Biscop *et* al. [52] revealed discrepancies in many of the studies that reported treatment selectivity. In addition, apart from the fact that several of the proposed explanations mentioned above are not general, exclusive properties of cancer cells, a study by Bekeschus *et al*. [53] screening 38 different cell lines for their susceptibility to CAP-induced cytotoxicity found no clear correlation with the expression of aquaporins or redox-regulating enzymes, although a correlation with cholesterol levels was found for a subset of cell lines. The authors even found a negative correlation between treatment sensitivity and metabolic activity for the investigated cell lines. One must keep in mind, though, that the treatment of cancer with CAP is a local treatment modality, similar to e.g. photodynamic therapy. This means that, in the end, the question of selectivity is not as important compared to in systemic treatment modalities [36].

In recent years, the attention in plasma oncology research lies increasingly on the immunotherapeutic effects of CAP treatment [16]. In 2015, Lin *et al.* [54] reported that *in vitro* treatment of nasophylangeal carcinoma with CAP was able to induce characteristics of immunogenic cell death (ICD), a cell death mechanism where the dying cells emit immune-stimulatory signals that makes them more detectable to the immune system [55]. This observation was soon reported for other cancer cell lines as well [56-58], followed by confirmation of the effect *in vivo* [59] and, especially more recently, proof of true immunotherapeutic effects of plasma treatment including abscopal effects [60, 61] and functional cancer vaccination [59, 62, 63]. This possibility of CAP as a local treatment modality to induce systemic anticancer immunity was soon identified as a very promising direction in the field [64, 65].

Currently, research into how CAP can affect different stages of the cancer-immunity cycle, a series of events initiated by ICD, is an important aspect of plasma oncology research, also going beyond the induction of ICD [66]. For example, CAP can induce changes in the expression of surface proteins that play an important role in the crosstalk between cancer cells and immune cells, such as immunosuppressive surface proteins or immune checkpoints. CAP can influence such proteins expressed on the cancer cell membrane in two ways. First, the treatment can cause direct chemical changes leading to post-translational modifications, which can alter the functionality of the proteins [67]. It was even demonstrated that CAP-treated proteins can lead to increased immunogenicity themselves [68]. Second, CAP treatment can lead to downstream effects that can change the expression of these proteins on the cell membrane on a longer timescale [69-71]. Observation of these effects has been reported both *in vitro* and *in vivo*.

From the above, we can say that plasma oncology shows much promise, especially given its immunotherapeutic potential. At the same time, much research is still needed, both to answer fundamental questions and for the field to establish itself as a clinical candidate.

3.3 CAP sources

So far, we have discussed the use of CAP in plasma medicine as if it is an unambiguous term. However, since the conception of the field, a plethora of different CAP devices have been developed, characterised and utilised in plasma medicine research [72, 73].

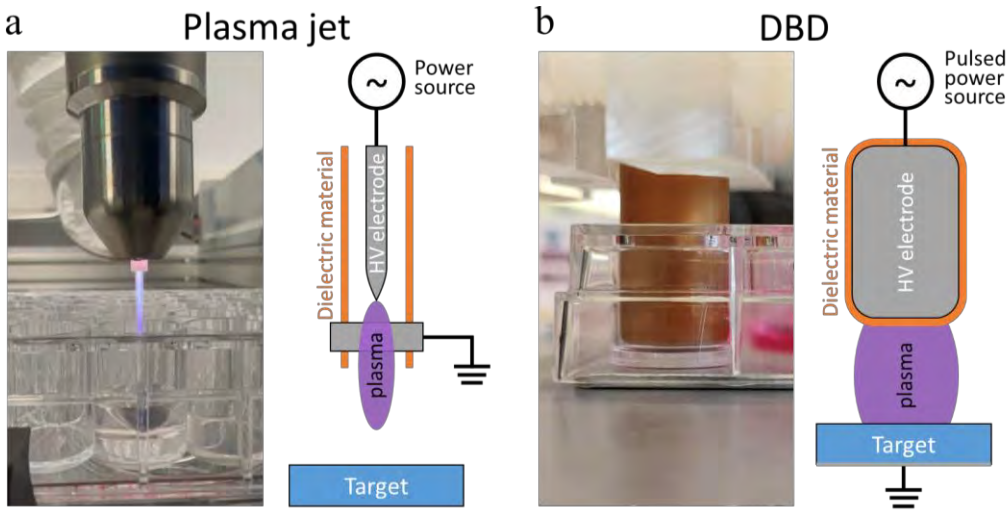

Figure 1-2. Example of (a) a plasma jet, and (b) a DBD, with their schematic geometry. Specifically, the plasma jet shown is the kINPen, which will be the subject of research in Chapters 2-4. The DBD shown is that used for the experimental research in Chapter 6.

One of the sources for generating CAP that is most used in plasma medicine research is the atmospheric pressure plasma jet (APPJ), or simply plasma jet. The general concept of a plasma jet is that a feed gas is guided through a hollow tube, in which the plasma is ignited. The plasma-produced reactive species are then transported toward the treatment target by the flowing gas. Many different types of plasma jets exist and are used in research, mainly differing in the number of electrodes and their configuration [74]. Plasma jets typically operate with a noble gas as the feed gas. In this case, the produced RONS can originate from two possible sources: either from impurities (or deliberate admixtures) in the feed gas [75, 76], or from mixing of the plasma effluent with the surrounding atmosphere [77]. Figure 1-2a shows a typical geometry for a plasma jet. The jet has two electrodes: a central pin electrode and a ring electrode separated from the working gas by the dielectric tube through which the feed gas flows. To generate the plasma, a voltage is applied to the pin electrode with either high frequency alternating current (AC, typically kHz to MHz), or pulsed direct current (DC), while the ring electrode is grounded.

The second type of CAP device most often used in plasma medicine research is the dielectric barrier discharge (DBD). It does not operate with a gas flow and instead directly generates the plasma in ambient air. A basic DBD consists of two parallel electrodes of which (at least) one is covered by a dielectric, separated by the discharge gap. For plasma medicine applications, the DBD typically consists of one powered electrode covered by the dielectric, and uses the treatment target as the second electrode, acting as either the anode or cathode [78]. Such a geometry is shown in Figure 1-2b.

A testament to the progress in the field of plasma medicine, is the fact that several CAP devices have received medical certification, be it only for wound healing applications. A notable example, for the context of this thesis, is the kINPen plasma jet, which received medical certification in 2013 and has so far been the subject of numerous studies [79-81]. A downside to the wide variety of CAP devices that have been used in the field, each also in different setups and conditions, is that comparison between experimental results can be difficult. As a result, there have recently been calls for more standardisation and uniformity in the field, to increase comparability and interpretability of reported results [36, 82].

3.4 How simulations fit in plasma medicine research

Most experimental biomedical research in plasma medicine is performed *in vitro* [82, 83], where treatment of (cancer) cells is typically performed in well plates of varying sizes. Beyond this, *in vivo* research is becoming more and more prevalent (and even some clinical trials have been reported [84, 85]), as this is crucial to progress the field and investigate the effects of plasma treatment in real tissue [36]. Still, *in vitro* research lies at the basis of understanding the possible effects of the treatment on cells. As RONS are the treatment's main effectors, it is in addition crucial to characterise the discharge and its production of these species in different CAP devices. This goes also beyond what is accessible to standard experimental methods that measure produced RONS in the far field, downstream from the discharge [86].

Moreover, cells *in vitro* are usually covered by a liquid layer such as cell medium [82]. This places the investigation of CAP treatment in the realm of plasma-liquid interaction research, which studies the interaction between CAP and liquids (usually water) [87, 88]. This field investigates various applications next to plasma medicine, such as water purification [8] and nitrogen fixation [89]. However, the interaction between a plasma jet and a liquid forms a very complicated system, with many phenomena influencing each other [90, 91], which makes experimental research challenging [87].

To support experimental research, both to understand RONS production and to investigate plasma-liquid interaction, computational modelling forms a valuable tool to gain insight into experimental results [10, 80]. The main strength in these simulations is the ability to separate various fundamental processes in a way that is impossible to achieve experimentally, and as such investigate their unique effects and contribution to the overall system. In this way, chemical kinetics modelling has made it possible to investigate the chemistry within the plasma, while fluid dynamic simulations allow us to understand the various transport phenomena in the system through which the produced RONS can reach the treated cells. In addition, molecular dynamics modelling has proven to be an invaluable tool to investigate the biological effects of the plasma treatment, such as its effect on biomolecules and their functions, at a scale that is very difficult to study in an experimental setting [92-94].

In the following, the current state-of-the-art of computational modelling through zero-dimensional, fluid dynamics and molecular dynamics simulations will be presented. This overview is not meant to be an exhaustive discussion of all computational efforts in the field, but should be sufficient to place the computational work done in this thesis within the broader context of the field.

4. Modelling in plasma medicine: state-of-the-art

4.1 Chemical kinetics modelling

Zero-dimensional (0D) chemical kinetics simulations, also referred to as global models, have been commonly employed to investigate the various chemical reaction pathways in CAP that lead to the formation of different RONS. In this approach, the densities of the simulated species resulting from chemical reactions are calculated as a function of time only, ignoring all spatial dimensions (hence the term “zero-dimensional”). Because this approach has a relatively low computational cost, it can take into account very large and detailed chemistry sets. To reach this low computational cost, a 0D model operates under the main assumption that the simulation volume is completely uniform, thus allowing for the reduction of this volume to a single point [95]. Because spatial dimensions are not considered, this also means that a 0D model ignores all transport phenomena in the system.

To simulate the chemistry in a plasma jet, the so-called “quasi-1D” approach has been used to account for the transport of species by the gas flow, which is crucial to capture the behaviour of a plasma jet. Here, knowledge on the velocity of the flowing gas in the jet is used to transform the time dependence of the 0D model into a spatial dependence in the axial direction of the jet. In essence, this means that the simulation volume of the model is a cylindrical volume element that flows with the gas through the jet [96]. As the feed gas mixes with the surrounding atmosphere in the effluent of a plasma jet, this additional source of ambient species must also be implemented into the quasi-1D approach.

A model using the above strategy has been developed for the kINPen by Van Gaens *et al.* [97], using a large chemistry set of 85 different species reacting in 1928 reactions developed for an argon plasma jet operating in humid ambient air [96, 98, 99]. While this model was able to investigate the full chemistry from the pin electrode to the far field, it did not account for the full waveform behaviour of the applied electric field, instead averaging the electric field through a general power deposition. By contrast, in the model developed by Schmidt-Bleker *et al.* [100, 101] for the kINPen, the exact applied electric field was taken into account, but only for a far smaller chemistry set. In addition, this model required much more fitting of the input parameters to match experimental results.

Some 0D modelling investigations have attempted to use a 0D model to describe the evolution of chemical species in a liquid treated by plasma, both for a DBD [102] and a plasma jet [103]. However, this provides only very approximate data, as 0D models are generally unsuited for this purpose. The transfer of species between the plasma and the liquid phase relies on various transport phenomena. Therefore, it can inherently not be accurately described in a 0D approach. For this purpose, a multidimensional model that can simulate these transport phenomena is needed.

4.2 Multidimensional fluid modelling

A multidimensional fluid model, which can be 1D, 2D or 3D, treats the modelled material as a continuum [104]. Because transport phenomena can be investigated within the simulated system, and spatial gradients can be resolved, a multidimensional model gives a far more realistic description of the physical phenomena in the simulated system compared to a 0D model. The drawback is that this comes at a much higher computational cost. For the investigation of plasma jets, 2D models have been most common, especially axisymmetric models.

Early 2D models, such as the model developed by Reuter *et al*. [105], were used mostly to investigate the mixing of the kINPen effluent with the surrounding atmosphere in a stationary state, without chemical reactions (i.e., as if the plasma is not ignited in the jet). These studies investigated the diffusion of oxygen and nitrogen into the jet effluent [105-107], as well as the effect of varying the composition of the surrounding air [77, 108].

To study the plasma discharge behaviour, the nonPDPsim modelling framework developed by Rauf and Kushner [109], has been employed in several case studies for a pulsed laminar jet operating in helium (as well as in multiple works to simulate a DBD discharge above tissue [110, 111] or liquid water [112-115]). While these studies have provided deeper insight into how the discharge in such a plasma jet is affected by, e.g., the electrical parameters [116], ambient gas composition [117] or feed gas admixtures [76], they have usually investigated only a single voltage pulse followed by up to a few ms of afterglow, because of the large computational cost of describing the full discharge behaviour. In addition, bar some exceptions [118, 119], most studies focus on operation of the free jet, without taking into account the effects caused by the presence of a treated substrate. The latter is true as well for several other 2D modelling studies of plasma jets [120, 121] and, in fact, also for most diagnostic investigations of the kINPen plasma and its effluent [80].

Treatment of a well plate with a plasma jet, in contrast to operation of the free jet (or the treatment of a flat surface), inherently causes a backflow toward the jet outlet, of which the flow pattern depends on the well geometry. This backflow may influence the dynamics of the jet effluent. Moreover, evaporation of the treated liquid in this case forms an additional source of water vapour that can affect the chemical pathways in the effluent [90, 122]. Finally, the transport and accumulation of RONS in the treated liquid takes place over timescales of several seconds or minutes [123]. Thus, a fluid model that aims to investigate this aspect of the system must be able to simulate these timescales, in contrast to the models discussed so far which either simulate to a stationary state (to investigate mixing in the effluent) or on the timescale of individual voltage pulses (to investigate discharge dynamics). Some computational efforts to investigate the interaction of a plasma jet with a liquid substrate in a well or beaker on longer timescales have been reported. Lindsay *et al.* [124] presented a 2D-axisymmetric model of a jet-like system above a petri dish, showing the importance of the induced convection in the liquid. Based on this, Verlackt *et al.* [125] developed a model with a more extensive chemistry set to investigate transport phenomena in a liquid-filled beaker treated by a

plasma jet. We later expanded this model to simulate the treatment of a well with a much smaller liquid volume, and combined this model with a 0D simulation to describe both the plasma chemistry and the transport of neutral species into the liquid during as well as after treatment [126]. In the same year, Semenov *et al*. [127] presented a modelling study on the description of convection and diffusion in the system and at the gas-liquid interface. Recently, Kamidollayev and Trelles [128] presented a 3D model focusing on the simulation of the dynamic gas-liquid interface that develops when liquid water is treated with a plasma jet, while Liu *et al.* [129] used a 2D-axisymmetric model to investigate the influence of the working gas (argon versus helium) on the transfer processes in this system.

While chemical kinetics simulations and CFD models are useful for investigating the chemical and physical phenomena that occur in the plasma and near the treated substrate, they do not provide any information on what actually happens to the treated cells. Indeed, the RONS will interact with the biomolecules that make up the treated cells and affect both their structure and function. To investigate these effects, a simulation method that is able to describe the behaviour of biomolecules at the atomic scale is needed.

4.3 Molecular dynamics modelling

A molecular dynamics (MD) simulation describes a system on the atomic level by solving Newton's equation of motion for each atom. While this provides detailed information on a scale that is inaccessible both experimentally and with the simulation methods described above, MD simulations inherently are computationally very expensive, limiting the system size and timescales that can be simulated. In classical MD, the forces to which the simulated atoms are subjected are calculated from an interatomic potential referred to as the "force field" (in contrast to, e.g., ab-initio MD where the forces are calculated directly from quantum mechanical calculations, though this further increases the computational cost significantly). These force fields can be either reactive, allowing for the breaking and formation of chemical bonds (once again increasing computational cost), or non-reactive, where the atoms retain their bonds throughout the simulation and the focus lies instead on physical interactions and conformational changes. For the latter, simulations can in practice be performed on systems containing up to the order of 10^6 atoms, on time scales of up to microseconds [92]. Although, of course, treating atoms as classical particles is an approximation, MD simulations have proven very useful for the study of biomolecules and drug development [130].

In the field of plasma medicine, MD simulations have been applied to study the effect of CAP on several biomolecules [94]. Several works have investigated the permeation of RONS through, and their interaction with, cell membranes [49, 50, 131-134] and protein channels [135, 136] to investigate the transport of plasma-generated species to the cell interior. The effect of electric fields, as present in direct treatment, has also been the subject of research [137].

Recently, focus has shifted more toward the effect of chemical changes induced by RONS, as would result from CAP treatment, on the properties of proteins. It was reported that these oxidative changes can lead to conformational changes in proteins and affect their ability to bind to receptors [138]. Recently, Yusupov *et al.* [139] showed that oxidation of cell adhesion protein CD44 and its ligand, hyaluronan, significantly decreased their binding affinity, and found indications that the breaking of important disulfide bonds near the binding groove plays an important role. Lin *et al.* [67] reported that the disruption of salt bridges of immune checkpoint CD47 connecting it to its ligand, caused by oxidation of Lys residues, was associated with conformational changes, and decreased the binding affinity of the CD47 – SIRPα complex.

5. Aim of this thesis

The aim of this thesis is to develop a computational model to investigate the physical phenomena at play during *in vitro* treatment of a liquid with a plasma jet and to use this model to improve our understanding of various parameters that can influence the experimental treatment of (cancer) cells. Recently, standardisation is becoming a prevalent topic in plasma medicine, as the wide variety of different treatment setups and conditions used in experiments since the conception of the field often makes results difficult to compare [36, 82]. Thus, understanding the impact of the chosen setup geometry on the treatment is useful to improve comparability as well as our understanding of the treatment effects as a whole. As a computational fluid dynamics model is able to separate the influence of different system parameters in a way that is difficult to achieve experimentally, this will be our method of choice. Moreover, to investigate the biological effects of CAP treatment on a microscopic scale, we will use molecular dynamics modelling to analyse the effects of treatment-induced protein oxidation, with a focus on the immunotherapeutic potential of CAP.

This thesis contains five research chapters, schematically represented in Figure 1-3, accompanied by a general introduction (Chapter 1, which you have now reached the end of) and a general conclusion (Chapter 7).

In **Chapter 2**, the computational 2D-axisymmetric fluid model developed for this thesis will be explained in detail and benchmarked against experimental data in literature. The model describes the transport phenomena at play during the treatment of a well plate with a plasma jet (based on the kINPen) and is able to simulate this on a timescale up to several minutes. The starting point for the development of this model was previous work done within PLASMANT (to which I previously also contributed) [125, 126]. The main goals are, however, to reach an improved description of the various physical phenomena in the model, resulting in a better comparison to experimental data, as well as to make the model as self-consistent as possible, i.e. reducing the need for external input data or fitting. This model will then be used for the research in the next three chapters.

In **Chapter 3**, the model is applied to investigate how *in vitro* treatment with a plasma jet is affected by the choice of the used substrate (i.e. well size), as well as the interplay of this effect with a gas shield during treatment. In addition, we will examine the mixing of the plasma jet effluent with the surrounding atmosphere, for different ambient conditions.

Chapter 4 builds on the results in Chapter 3 and systematically investigates how the geometry of the shielding gas device can affect its performance, and how it changes the conditions in the plasma effluent. Indeed, since the initial introduction of a gas shield in plasma medicine, various geometries have been used in research, while the effectiveness of the shield and its effect on the plasma has rarely been reassessed.

In **Chapter 5**, we will show that a lack of uniformity can arise not only in experimental setups, but also in computational models. Over the past decade, many different boundary conditions to describe transfer of chemical species over the gas-liquid interface have been reported and used in models developed to study plasma-liquid interaction. We will here use our model to test the validity of these formulas, and investigate how they compare to one another.

Finally, in **Chapter 6**, we employ a different type of modelling, specifically molecular dynamics, to investigate how CAP treatment affects MHC-I molecules and their ability to bind to their NK cell receptors. With this investigation, we focus on the immunotherapeutic potential of CAP treatment and look at biological effects that are out of reach for a fluid dynamics model. Furthermore, these computational results are combined with experiments (contribution of Hanne Verswyvel, shared first author to the publication on which this chapter is based), where the effects of CAP on the expression of a range of NK cell ligands are studied. Both the effects on short (as a measure of direct chemical changes) and longer (representing the downstream effects of the treatment on cellular signalling pathways) timescales are investigated.

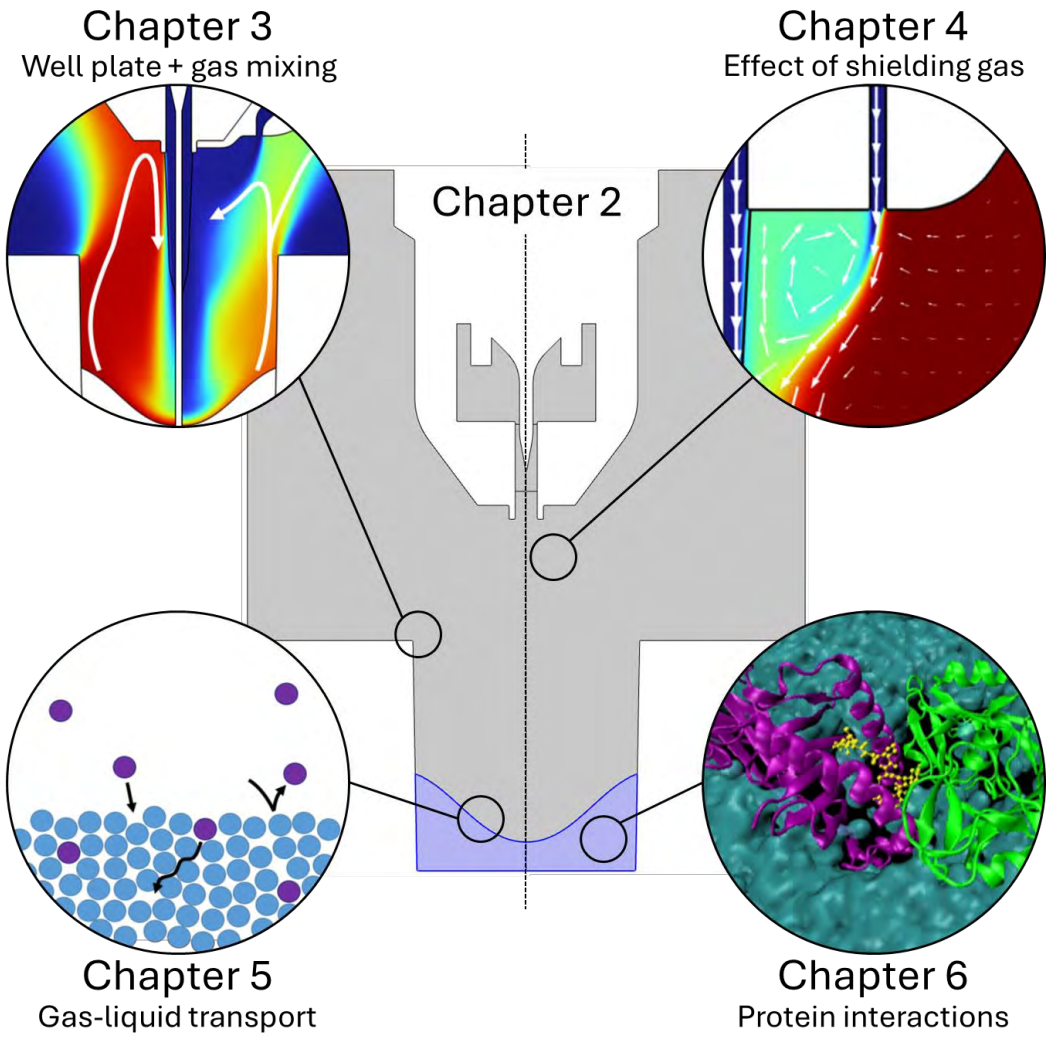

Figure 1-3. Schematic overview of the thesis.

Chapter 2

Modelling *in vitro* treatment with a plasma jet

The content of this chapter is in part based on:

Liquid treatment with a plasma jet surrounded by a gas shield: effect of the treated substrate and gas shield geometry on the plasma effluent conditions
Pepijn Heirman, Ruben Verloy, Jana Baroen, Angela Privat-Maldonado, Evelien Smits and Annemie Bogaerts
J. Phys. D: Appl. Phys., 57, 115204 (2023)
https://doi.org/10.1088/1361-6463/ad146b

and

Critical comparison of interfacial boundary conditions in modelling plasma–liquid interaction
Pepijn Heirman and Annemie Bogaerts
J. Phys. D: Appl. Phys., 58, 085206 (2024)
https://doi.org/10.1088/1361-6463/ad9c8f

1. The simulated system

To investigate the physical phenomena at play during *in vitro* treatment of a liquid with a plasma jet, we developed a 2D-axisymmetric fluid dynamics model that describes various transport phenomena in this setup. The aim of this model is to investigate the transport of chemical species in the simulated system, as well as their accumulation in the treated liquid on a timescale of minutes. Thus, in its current form, the model does not describe the plasma discharge itself, which would limit the simulation to much shorter timescales (cf. Chapter 1).

The model is constructed with the CFD software COMSOL Multiphysics (version 6.2) [140]. Figure 2-1 shows the simulated geometry for the general case of the model, as explained in this chapter. The plasma jet geometry is based on that of the kINPen [80]. The jet nozzle (i.e., the dielectric tube) has an internal diameter of 1.6 mm, and contains the pin electrode with a diameter of 1 mm, with its tip at a distance of 3.5 mm before the outlet of the jet. The dimensions of the treated well are those of a 24-well plate containing 1 mL of liquid. When treated with a plasma jet, a liquid surface is deformed because of the impinging gas from the jet, causing a dimple of which the shape and depth depend on the treatment setup [141]. The gas-liquid interface is treated in the model as a stationary surface, of which the shape is based on observations made in the lab for the same setup geometry. In the general model case, the gas flow rate at the jet inlet is 2 standard liters per minute (SLM), and the treatment gap, i.e. the distance between the jet nozzle and the liquid surface (in its original state), is 20 mm. We selected these conditions to make sure that, in the experimental work performed with this geometry, there would be no liquid splashing out of the well, and the jet would operate in a non-touching regime, i.e. no direct discharge onto the liquid occurs.

The main workflow of the model is as follows: first, we calculate the stationary state of the flow field in the system. Using this stationary flow field as the input, we simulate the temperature and transport of species in the system in a time-dependent manner. In this way, mixing of the feed gas with the surrounding atmosphere (O_2, N_2 and H_2O), which will heavily impact the formation of RONS in this system, can be investigated, as well as the transport of chemical species throughout both the gas and liquid phase in the system. In the following, the main equations that are solved by the model will be explained.

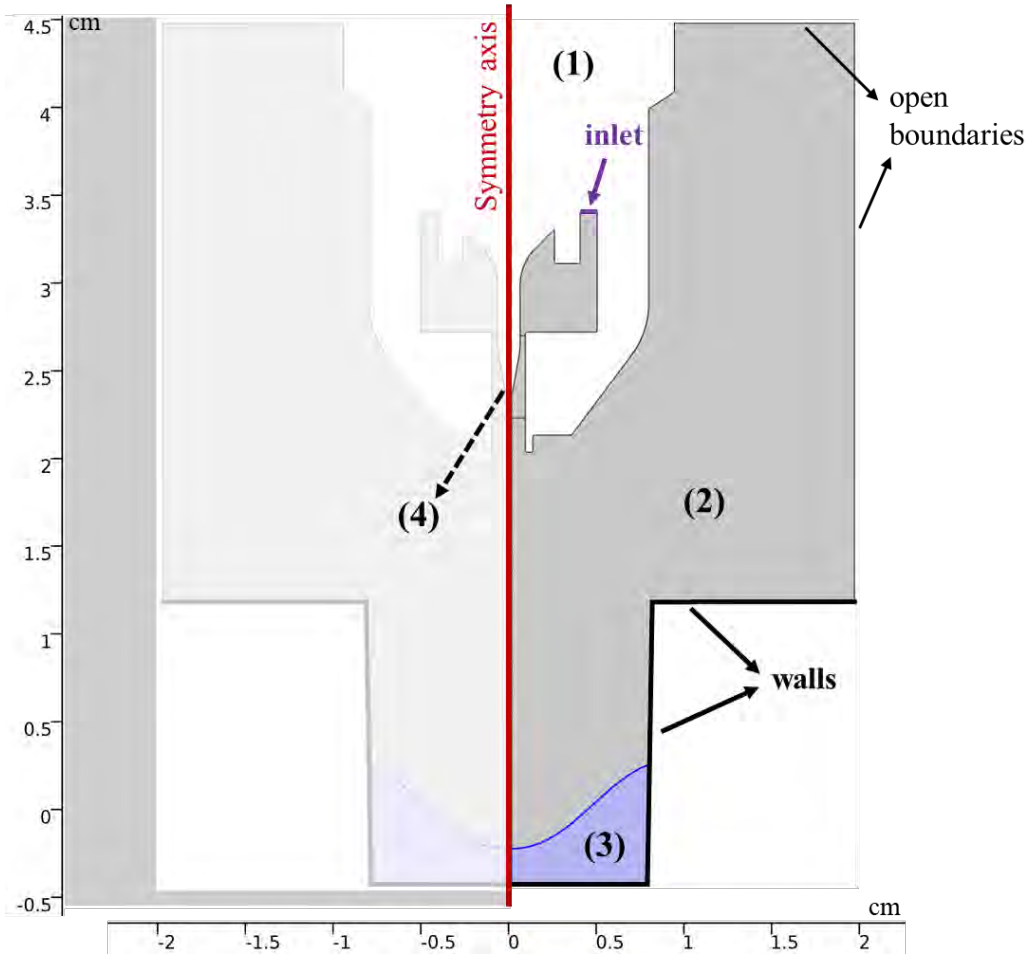

Figure 2-1. General model geometry. The geometry components are (1) the plasma jet, (2) gas phase and (3) liquid phase. The pin-electrode (4) is indicated for clarity. The boundary conditions applied at the edges of the model are indicated. As the geometry is 2D axisymmetric, only the right part is simulated by the model, with the symmetry axis indicated in red.

2. Description of the model

2.1 Stationary calculation of the fluid flow

The flow field in the system is calculated by solving the time-independent, incompressible Navier-Stokes equations [104, 142]:

$$\rho\nabla \cdot \vec{u} = 0 \tag{E.2-1}$$

$$\rho(\vec{u} \cdot \nabla)\vec{u} = \nabla \cdot [-p\boldsymbol{I} + \boldsymbol{K}] \tag{E.2-2}$$

With ρ the density (kg/m³), $\vec{u}$ the velocity vector (m/s) and p the pressure (Pa). **I** is the identity matrix, while **K** is the viscous stress tensor (Pa). It is known from experiments with the kINPen that when applying a gas flow rate of 3 SLM Ar through the jet (corresponding to a Reynolds number Re ≈ 2700), the jet is in a fully turbulent regime [143]. For round jets, flow is typically turbulent starting from Re ≈ 2000 [144], though for the kINPen flow instabilities have been observed starting from a flow rate above 1 SLM Ar (Re ≈ 1000) [80]. Turbulent instabilities are especially important in the shear mixing layer between the jet effluent and the ambient. Therefore, we employed Menter's shear stress transport (SST) turbulence model [145] as implemented in the COMSOL CFD module [142]. The SST model is a so-called Reynolds-averaged Navier-Stokes (RANS) model. Briefly, a RANS model splits the flow variables into a time-averaged and a fluctuating part. The fluctuating terms are then grouped together in the Reynolds stress tensor, which is modelled by writing the viscous stress tensor in equation (E.2-2) as:

$$\boldsymbol{K} = (\mu + \mu_T) \cdot (\nabla\vec{u} + (\nabla\vec{u})^T) \tag{E.2-3}$$

With μ the dynamic viscosity (Pa·s) of the fluid and μ_T the so-called turbulent dynamic viscosity. Superscript T represents the transposition operation. The new unknown parameter μ_T must then be solved for by adding additional equations. The SST model adds two transport equations, for the turbulent kinetic energy k and for the specific dissipation rate ω:

$$\rho\vec{u} \cdot \nabla k = \nabla \cdot \big((\mu + \sigma_k\mu_t)\nabla k\big) + P - \rho\beta_0^* k\omega \tag{E 2-4}$$

$$\rho\vec{u} \cdot \nabla\omega = \nabla \cdot \big((\mu + \sigma_\omega\mu_t)\nabla\omega\big) + \frac{\rho\gamma}{\mu_t}P - \rho\beta\omega^2 + 2(1 - f_{v1})\frac{\rho\sigma_{\omega 2}}{\omega}\nabla\omega \cdot \nabla k \tag{E 2-5}$$

Which then allows calculation of the turbulent dynamic viscosity:

$$\mu_t = \frac{\rho a_1 k}{\max(a_1 \omega, S f_{v2})} \tag{E.2-6}$$

In the above equations, P represents the turbulent kinetic energy source term. β_0^* and a_1 are turbulence modelling constants, while β, γ, σ_k and σ_ω are turbulence modelling parameters, and f_{v1} and f_{v2} are blending functions. Finally, S is the characteristic magnitude of the mean velocity gradients. More information on these parameters is given in Appendix A.

Walls are treated with the no-slip boundary condition, which means that the boundary condition $\vec{u} = 0$ is applied. Flow is fully resolved down to the walls (low Reynolds number approach) and accordingly it was made sure that the mesh adheres to the $y^+ < 1$ condition, for y^+ the dimensionless wall distance, on all walls [142]. At the open boundaries, a pressure of 1 atm is prescribed as a normal stress, while at the inlet of the jet the inflow is prescribed with a normal velocity that corresponds to the total flow rate of 2 SLM.

At the stationary gas–liquid interface, the gas flow sets the liquid in motion through continuity of flow velocity and shear stress. To achieve this in the model, the following boundary conditions are applied to the gas-liquid interface:

$$\vec{F} = (\boldsymbol{K} \cdot \overrightarrow{n_t})\overrightarrow{n_t} \tag{E.2-7}$$

$$\overrightarrow{u_l} - \overrightarrow{u_g} = 0 \tag{E.2-8}$$

$$\overrightarrow{u_g} \cdot \vec{n} = 0 \tag{E.2-9}$$

Where F is the shear stress exerted on the liquid surface with tangential vector $\overrightarrow{n_t}$, while $\overrightarrow{u_l}$ and $\overrightarrow{u_g}$ are the velocity vectors of the liquid and gas, respectively. Equation (E.2-7) thus applies a tangential projection of the stress at the wall. Equation (E.2-8) applies, in essence, a no-slip condition, while equation (E.2-9) prescribes a no-penetration condition for the gas flow. The latter is achieved in the model by treating the interface, from the perspective of the gas, as a slip wall, while the boundary layer still develops because of equation (E.2-8).

2.2 Time-dependent calculation of the heat transfer and species transport

The model calculates the temperature in the gas and liquid phase by solving the conservation of energy through the heat balance equation [146, 147]:

$$\rho C_p \frac{\partial T}{\partial t} + \nabla \cdot \vec{q} + \rho C_p \vec{u} \cdot \nabla T = Q \tag{E.2-10}$$

Where C_p is the heat capacity at constant pressure (J/kg·K), T is the absolute temperature (K) and $\vec{q} = -\kappa \nabla T$ is the conductive heat flux, with κ the thermal conductivity (W/m·K) (not to be confused with the turbulent kinetic energy k described above). Q represents additional heat sources like, in this model, viscous dissipation and heat loss due to water evaporation. In the gas phase, the effect of turbulence is accounted for through Reynolds averaging of the heat balance equation, in a similar way as described above. Here, an additional fluctuating term (the turbulent transport of heat) is modelled by writing the conductive heat flux as:

$$\vec{q} = -(\kappa + \kappa_T) \nabla T \tag{E.2-11}$$

Where κ_T is the so-called turbulent thermal conductivity, itself calculated as:

$$\kappa_T = -\frac{\mu_T C_p}{Pr_T} \tag{E.2-12}$$

More information on the calculation of the turbulent Prandtl number Pr_T is given in Appendix A.

The transport of chemical species by convection and diffusion is calculated by solving the conservation of mass through the continuity equation [147, 148]. In the gas phase, we solve for the mass fraction of all species, so the continuity equation has the following form:

$$\rho \frac{\partial \omega_i}{\partial t} + \nabla \cdot \vec{J}_i + \rho(\vec{u} \cdot \nabla)\omega_i = R_i \tag{E.2-13}$$

Here, ω_i is the mass fraction of species i, while $\vec{J}_i$ is its diffusive flux. The density is calculated using the ideal gas law. R_i represents the net production or consumption of chemical species (equal to zero in case no chemical reactions are included). The continuity equation is solved for each species, except argon, of which the density is determined in the gas phase through the fact that the sum of all mass fractions must be equal to 1:

$$\omega_{Ar} = 1 - \sum_{j \neq Ar} \omega_j \tag{E.2-14}$$

The diffusive flux is defined in the gas phase as:

$$\vec{J_i} = -\rho D_{m,i} \nabla \omega_i - \frac{\rho \omega_i}{M} D_{m,i} \nabla M + \overrightarrow{J_c} - \rho D_{T,i} \nabla \omega_i \tag{E.2-15}$$

$$\text{with } D_{m,i} = \frac{1 - \omega_i}{\sum_{j \neq i} \frac{x_j}{D_{ij}}} \tag{E.2-16}$$

$$\text{and } D_{T,i} = \frac{\mu_T}{\rho \cdot Sc_T} \tag{E.2-17}$$

Where M is the mean molar mass (kg/mol) and x_j is the molar fraction of species j. The formulation of the diffusive flux is based on a mixture-averaged diffusion model, which solves for the diffusion of each species i in the mixture of species j≠i, assuming a Fickian relation between the diffusive flux and the molar fraction gradient. $D_{m,i}$ is the mixture-averaged diffusion coefficient (m²/s), as derived from the simplified Maxwell-Stefan equations for multi-component diffusion [149], which is calculated using the binary diffusion coefficients D_{ij} of each species pair i,j (see Appendix A), while $\overrightarrow{J_c}$ is a correction term, which ensures that the net diffusive flux equals zero [148]. $D_{T,i}$ is the eddy diffusivity; this additional diffusive flux accounts for the turbulent mixing by eddies that are not resolved by the turbulence model. More information on the calculation of the turbulent Schmidt number Sc_T is provided in Appendix A. Other species-specific parameters C_p and κ are also self-consistently calculated within the model, as described in Appendix A.

In the liquid phase, we assume that the whole phase has the properties (e.g. density, heat capacity, etc.) of the solvent, i.e., water. We do not solve the continuity equation for water itself, instead we solve for the concentrations of different chemical species dissolved in the water. Thus, the continuity equation here has the following form:

$$\frac{\partial c_i}{\partial t} + \nabla \cdot \vec{J_i} + \vec{u} \cdot \nabla c_i = R_i \tag{E.2-18}$$

Where c_i is the molar concentration of species i. The diffusive flux is defined using simply Fick's law:

$$\vec{J_i} = -D_i \nabla c_i \tag{E.2-19}$$

The diffusion constants D_i are in this case taken from literature (see Appendix A). The above approach for transport of chemical species is sufficiently accurate for dilute solutes, as is the case in the liquid phase.

At the jet inlet, argon enters the domain, containing impurities (1 ppm O_2, 4 ppm N_2, 3 ppm H_2O [103, 126]). The temperature of the gas flowing into the system via this inlet is set to 327 K, which is the temperature experimentally measured at the outlet of the kINPen [107]. At the open boundaries we specify a constant concentration of N_2, O_2, and H_2O equal to the initial conditions in the gas phase, i.e. humid air with a H_2O concentration that depends on the specified relative humidity and temperature, taken to be 50 % and 293 K in the general case. Walls are treated as thermally insulating, with a no-penetration boundary condition for the chemical species. At the gas-liquid interface, the temperature is continuous ($T_l = T_g$). Water evaporation is accounted for with a flux that keeps the water density at the interface in line with the vapour pressure of water, which is in turn calculated via Antoine's law [150]:

$$log\left(p_{H_2O}\right) = 8.07131 - \frac{1730.63}{233.426 + T} \tag{E.2-20}$$

Evaporative cooling, i.e. the heat loss at the liquid interface due to the evaporation of water, is implemented by prescribing a loss of heat at the interface as follows:

$$Q_{water\ evap} = J_{H_2O} \cdot H_{vap} \tag{E.2-21}$$

With J_{H_2O} the molar flux of water due to evaporation, as calculated by the model, and H_{vap} the latent heat of evaporation (for water = 2260 kJ/kg).

Transport of chemical species other than H_2O over the gas-liquid interface is implemented with a flux designed to adhere to Henry's law if the system reaches equilibrium. The formulation of this flux will be extensively discussed in Chapter 5.

2.3 Mesh

The complete mesh contains ~200 000 elements. Figure 2-2 shows the mesh of the model, including several detailed areas where the mesh is particularly fine. The final mesh is the result of several mesh refinement studies in crucial areas, i.e. the area around the pin electrode, the effluent region of the jet and the gas-liquid interface. In these studies, the maximum mesh element size was reduced until this refinement did not significantly affect the computational results anymore and it was made sure that gradients are adequately resolved.

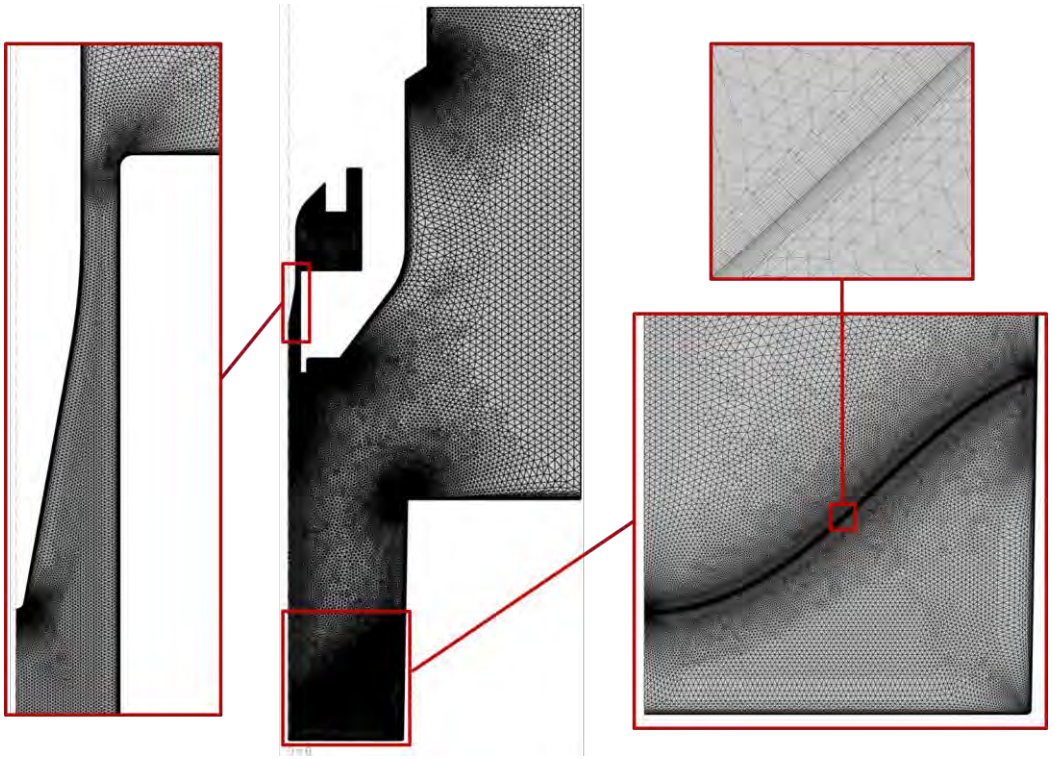

Figure 2-2. Mesh used in the model geometry. Regions where the mesh is particularly fine are shown in more detail.

3. Benchmarking

British statistician George E. P. Box is famously quoted with the phrase “All models are wrong, but some are useful”. The question thus presents itself how useful the modelling approach presented so far in this chapter actually is. To gain confidence in the results of the model and to understand its limitations, the remainder of this chapter will attempt to replicate published experimental measurements with the model, and address some of the assumptions made.

3.1 Conditions in the jet effluent

One of the main questions regarding the validity of the model is how well it can describe the mixing of the jet effluent with the surrounding atmosphere. Experiments to investigate mixing in the effluent of the kINPen were performed by Schmidt-Bleker *et al.* [107] using Schlieren imaging for the free jet (i.e. without a substrate), operating with a feed gas of 3 SLM pure Ar. To evaluate the performance of the model, its geometry was changed to represent the free jet, and the conditions adapted to those described in [107]. The resulting model geometry is similar to that shown in Figure 2-1, but instead of the well an outlet is defined at 3 cm below the jet nozzle. Figure 2-3 shows that we get quite good agreement, especially when considering that the spatial resolution of the experiments likely means that the experimental data is slightly smoothed out, as mentioned in [107]. When comparing the simulation results to the experimental data directly, we find that the distance from the nozzle where the effluent starts mixing with the surrounding atmosphere is slightly overestimated in the model, by about 3 mm. To show this, Figure 2-3 also contains the simulation results 3 mm further downstream for each line, giving an almost exact match to the experimental data.

Many computational fluid models described in literature that model the kINPen employ the k-ε turbulence model in the gas phase. Indeed, Schmidt-Bleker *et al.* [107] themselves also report on a fluid model for the kINPen using the k-ε model, showing good agreement with their experiments. However, this turbulence model is not a low-Reynolds number RANS model, meaning that it does not accurately resolve flow down to the wall. While this seemingly does not cause much issue for simulating mixing in the jet effluent (even though the flow profiles inside the jet are very different, as shown in Appendix B), we here employ the SST model instead of the k-ε model. Indeed, as it is our goal to specifically simulate the plasma jet above a liquid substrate, the behaviour at the

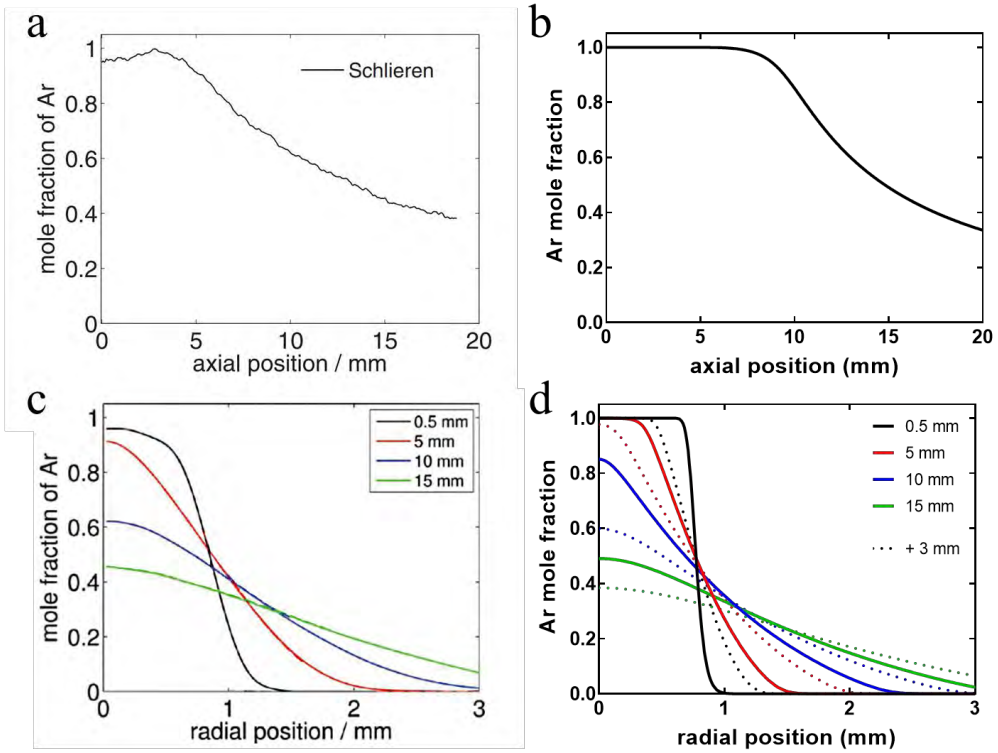

Figure 2-3. Experimentally measured (a) axial (with respect to the jet nozzle) and (c) radial (with respect to the symmetry axis, for different axial positions) variation of the argon mole fraction in the effluent of the kINPen operating at 3 SLM, as reported by [107]. (b, d) Ar mole fraction as calculated by our model for the same geometry and conditions. In (d), the data is also shown 3 mm downstream for each axial position, illustrating the slight overestimation of where the effluent starts mixing with the ambient when comparing directly to the experimental data. Figures (a) and (c) adapted from [107].

gas-liquid interface is of crucial importance in our case. While more sophisticated turbulence models, such as Large Eddy Simulations (LES) are available and could well give results that are closer to reality, such a modelling approach is incompatible with a 2D-axisymmetric geometry (requiring instead a 3D model) and would thus lead to impractically long calculation times [142]. Moreover, from the data presented in this section we can state that, for the purpose for which we built our model, the chosen modelling approach is sufficiently accurate.

In Figure 2-4, the model results are compared to experimental data for a higher feed gas flow rate of 5 SLM. The experiments in question are those performed by Reuter *et al.* [105] using VUV spectroscopy. While the axial distance where the feed gas starts mixing with the ambient agrees well (again a slight overestimation can be seen in the model results), the model predicts a rise in oxygen and nitrogen concentrations that differs from the experimental observations by about a factor two (note the values on the y-axis). Comparison of Figure 2-4 and Figure 2-3 reveals that the model in its current form may be less suited for higher flow rates through the jet, although qualitative agreement with experiments is still reached. In the remainder of this thesis, we simulate the kINPen only at flow rates of 3 SLM or below.

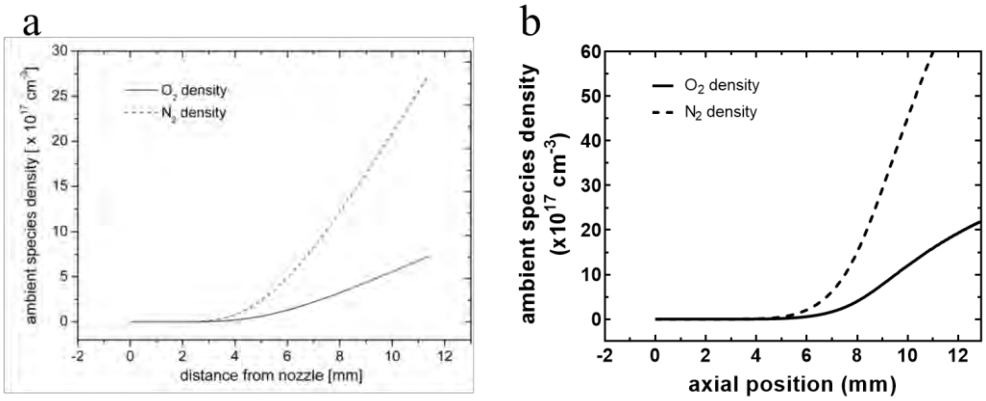

Figure 2-4. (a) Experimentally measured N_2 and O_2 density in the effluent of the kINPen operating at 5 SLM, as a function of distance from the jet nozzle, as reported by [105]. (b) N_2 and O_2 density as calculated by our model for the same geometry and conditions. Note that the y-axis is not the same for both panels. Figure (a) adopted from [105].

Apart from data on the mixing between feed gas and ambient air, Schmidt-Bleker *et al.* [107] also report on the temperature in the plasma effluent for a flow rate of 3 SLM. Figure 2-5 shows that also here our model provides adequate agreement to the experimental data: while the temperature only starts decreasing further downstream compared to the experimental measurements, at an axial distance of 15 mm the simulated temperature profile agrees well with that in [107].

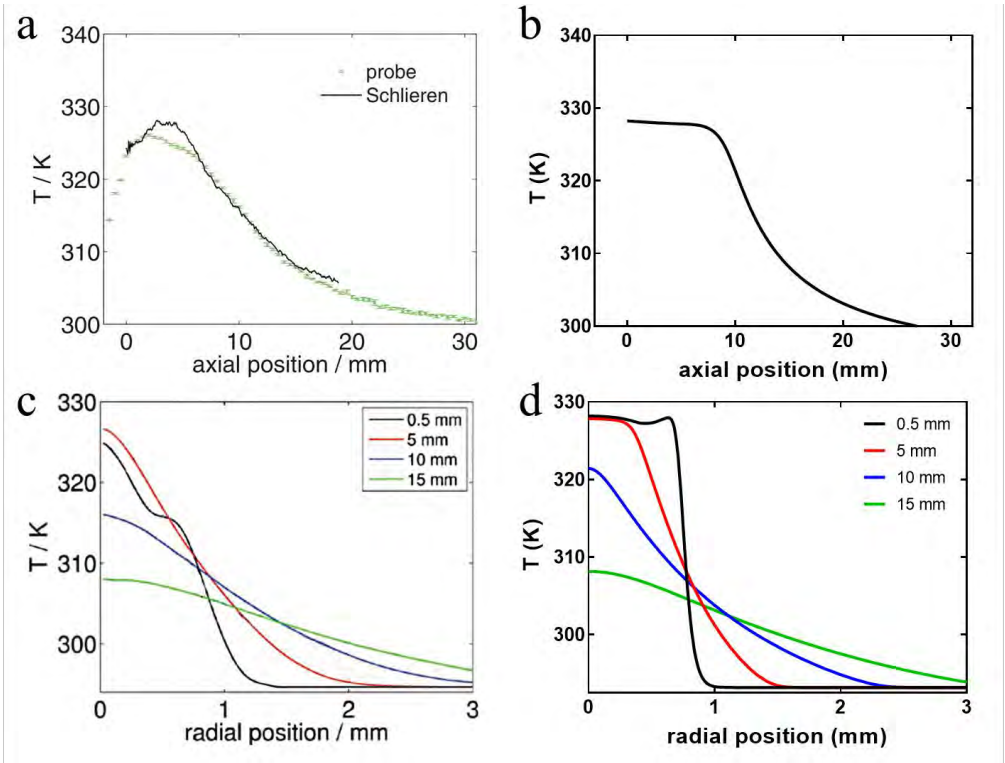

Figure 2-5. Experimentally measured (a) axial (with respect to the jet nozzle) and (c) radial (with respect to the symmetry axis, for different axial positions) temperature variation in the effluent of the kINPen operating at 3 SLM, as reported by [107]. (b, d) The temperature as calculated by our model for the same geometry and conditions. Figures (a) and (c) adapted from [107].

Finally, let us take a closer look at a central approximation in our modelling approach. As explained in Section 1 of this chapter, we implement a so-called one-way coupling between the stationary simulation of the flow field, and the time-dependent simulation of heat transfer and species transport. This is, however, an approximation, as in this way we do not take into account any effect that the different temperatures or gas compositions will have on the flow field variables. In turn, such changes in the gas velocity or density may lead to changes in the calculated temperature or species transport. To test the effect of this approximation, we performed a fully coupled, time-dependent simulation of the gas flow, heat transfer and species transport, assuming weakly compressible flow. The results are included in Appendix B, and show that this only has a marginal effect on the modelling results. There is only a minor change in the calculated mixing of the jet effluent with the surrounding atmosphere. The calculated gas temperature only differs slightly right after the feed gas exits the jet, while further

downstream there is no difference between the two simulation approaches anymore. This is not unexpected, since e.g. the temperature differences throughout the model are quite small. An additional reason why we continue using the one-way coupled approach is that the fully coupled model has a much higher computational burden. Indeed, the calculations for the latter took almost 50 times longer compared to the former.

Similarly, any effects of the discharge on the gas flow profile are not accounted for in the model, as we do not simulate the actual discharge itself in the plasma jet. While it is known that such effects can be substantial for e.g. He discharges (depending as well on the jet geometry) [151], the effects are limited for Ar jets [80], making this a fair approximation. Indeed, it has been reported for the kINPen operating in Ar that while the plasma ignition affects the onset of turbulence (i.e., causing turbulence to arise at lower flow rates compared to simple gas flow), the flow profile in already turbulent regimes was unaffected by the discharge [143].

3.2 Liquid phase flow profile

In a computational model that aims to simulate plasma-liquid interaction and the transfer of chemical species from the gas to the liquid phase, the velocity field in the simulated system is crucial. Indeed, the velocity field greatly affects transport of gaseous species over the gas-liquid interface, as it can transport species away from the interface towards the liquid bulk more efficiently than would occur solely through diffusion [124]. To confirm that our description of the liquid velocity field, in particular the way it is set in motion by the shear stress exerted on it by the flowing gas, is correct, we performed simulations based on published experimental work where the induced liquid flow profile was investigated.

A first comparison can be made with the flow profile visualised by Van Rens *et al.* [141] using laser scattering on microbubbles, while treating a large volume of water with the kINPen at a flow rate of 1.9 SLM. This work has been used before for the validation of computational models of a plasma jet above liquid water [127, 128]. Figure 2-6 shows a qualitative agreement with the liquid flow profile predicted by our model. It correctly shows the small vortex that arises where the liquid surface meets the wall of its container, although it is predicted to be somewhat smaller than visible in the experimental setup. A direct comparison is not applicable, however, as in the experiment the liquid container was cubic and thus not axisymmetric like the model. This will most likely affect the flow profile. Nevertheless, this comparison does give a first indication that the flow profile predicted by the model is at least qualitatively correct.

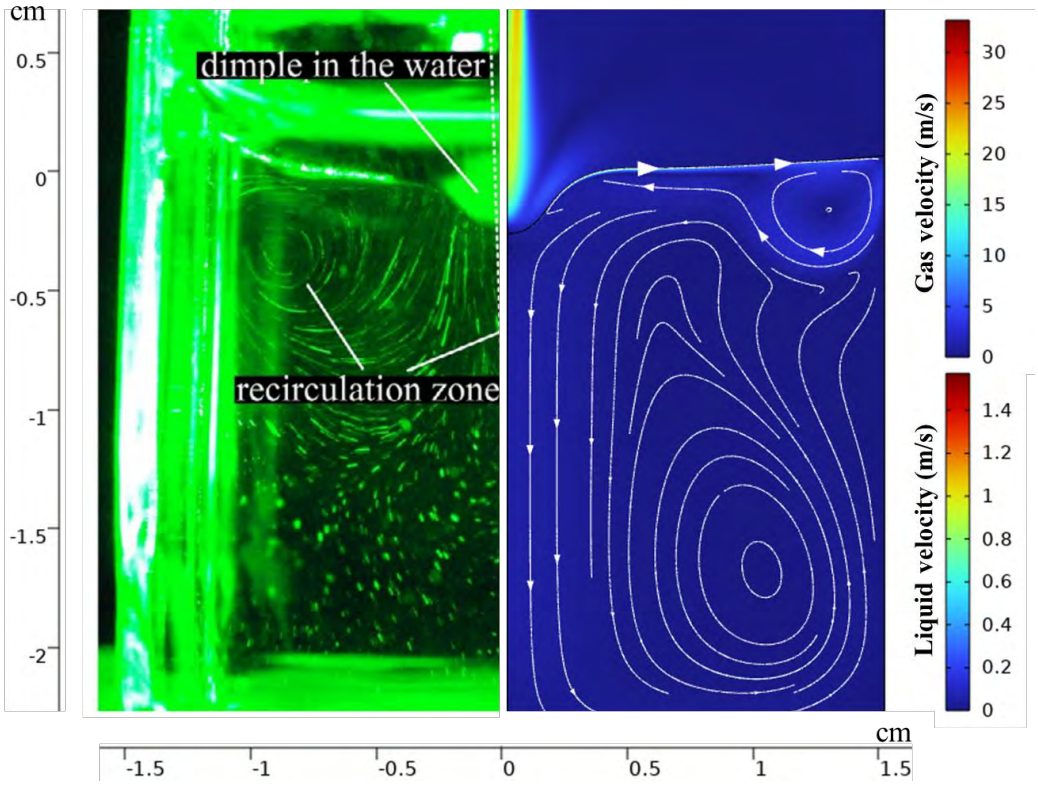

Figure 2-6. Experimentally determined liquid flow field as reported in [141] (left panel), compared to the calculated flow fields predicted by our model for similar geometry and conditions (right panel). Adapted from [141].

To investigate how well the model simulates the liquid flow in smaller liquid volumes, we adapted the geometry and conditions of the model to those of the experimental work by Stancampiano *et al.* [152] Here, the authors treated a 0.5 % starch solution with a He plasma at a flow rate of 1 SLM, allowing for visualisation of the velocity field by addition of KI to the liquid. To mimic the conditions in these experiments, we adapted our model to the conditions used in [152]. The results of these simulations are shown in Figure 2-7.

We can see that the velocity fields calculated in our model qualitatively agree well with those observed in [152]. Moreover, the maximum velocity of the liquid at the interface, under influence of the shear stress exerted by the flowing gas, is 0.3 m/s. This also falls in the range predicted by [152]. Based on these simulations, we believe that the description of the velocity field in our modelling approach is sufficiently accurate, and thus so is its influence on the transport of chemical species throughout the simulated system.

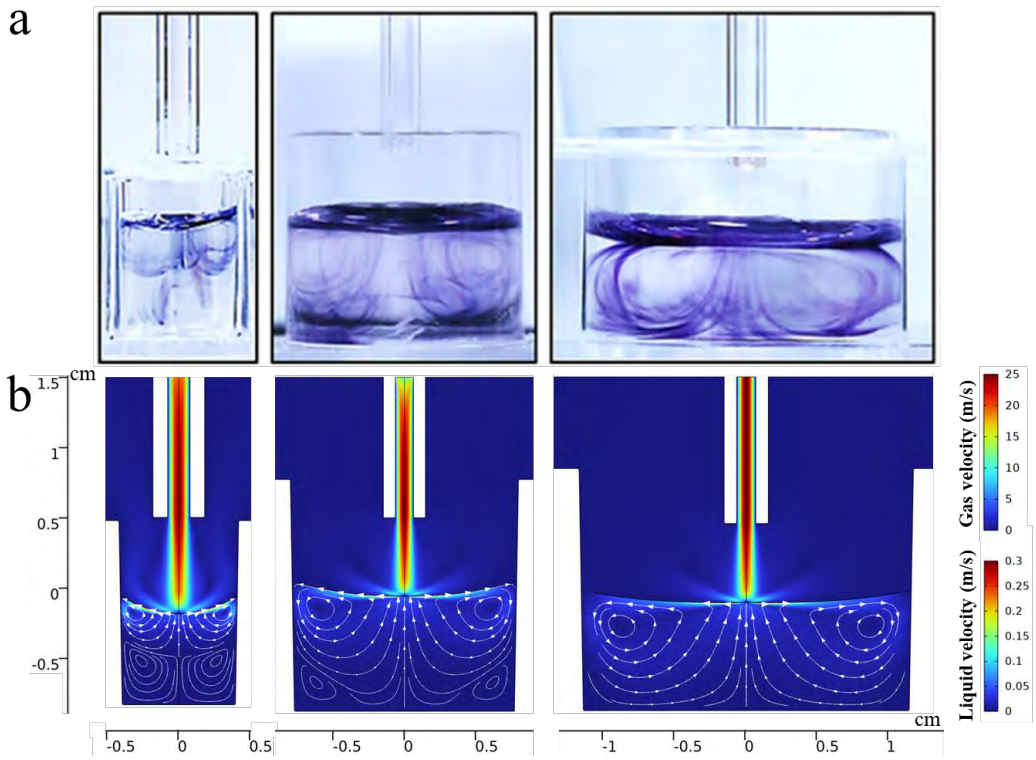

Figure 2-7. (a) Experimentally determined liquid flow fields as reported in [152], compared to (b) the calculated flow fields predicted by our model for the same geometries and conditions. Figure (a) adopted from [152].

As mentioned earlier, the gas-liquid interface in the model is treated as a static surface, of which the shape is based on experimental observations. One can consider the implemented shape as an average of the actual interface shape. In reality, the interface oscillates around this average, with the size of the oscillations depending on the well size and gas flow rate. While some computational fluid dynamics models in literature, that simulate the treatment of a liquid with a plasma jet, simulate this movement of the dynamic interface, even in these works the interface is simulated until a (quasi) stationary state is reached, after which the stationary interface shape is used for simulating the transport of chemical species throughout the system [127, 128]. While a dynamically oscillating interface will likely have an effect on this transport, such as locally enhanced mixing, species are already efficiently transported throughout both phases by convection. Thus, although it may be interesting to investigate the effects of a dynamic interface in the future, we believe that the approximation of using an “average” stationary surface has only a minor effect

3.3 Evaporative cooling of the liquid

At the liquid surface, water vapour will be continuously blown away by the dry feed gas from the plasma jet. To sustain the vapour pressure of water, the liquid will continuously evaporate during the treatment, taking away energy from the liquid and thus affecting its temperature. In the work of Stancampiano *et al.* [152], which was already discussed above, the resulting cooling of the liquid was observed experimentally using an infrared camera. Figure 2-8 shows the comparison between these experimental findings and the results of our model. The results agree quite well. The model overestimates the cooling by only 2 - 3 K after 80 s. This could be expected, however; unlike the experiments used for comparison in Figure 2-7, the temperature measurements were performed in [152] for a square well with the same characteristic length as a 24 well plate, thus holding a larger liquid volume than in the axisymmetric case, that will thus cool down more slowly.

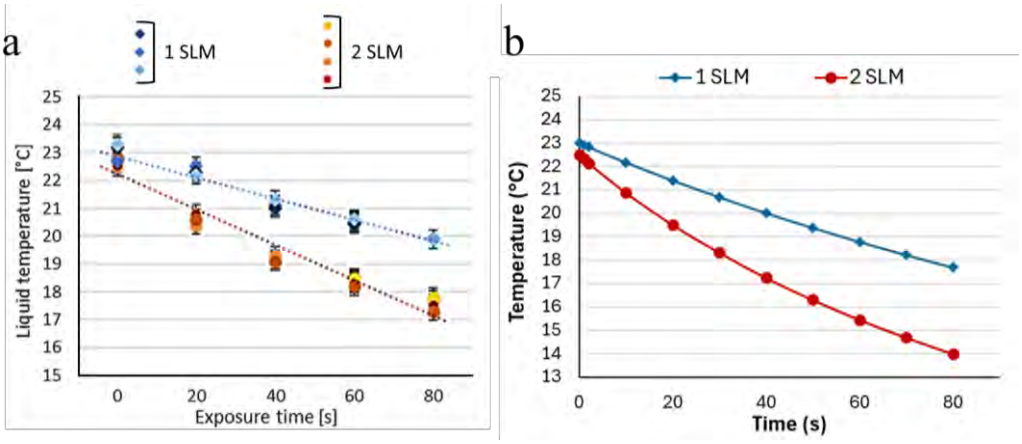

Figure 2-8. (a) Experimentally determined liquid cooling, caused by treatment with a He plasma jet operating at either 1 or 2 SLM, as reported in [152], compared to (b) the calculated temperature predicted by our model for similar geometry and conditions. Figure (a) adopted from [152].

In previous work [126], we also confirmed the occurrence of this evaporative cooling experimentally for the treatment of 2 mL water in a 12-well plate treated with the kINPen, by measuring the temperature of the treated liquid with a thermocouple during treatment. Figure 2-9 shows the model is able to simulate this cooling correctly, even giving quantitative agreement with the experimental results in this case.

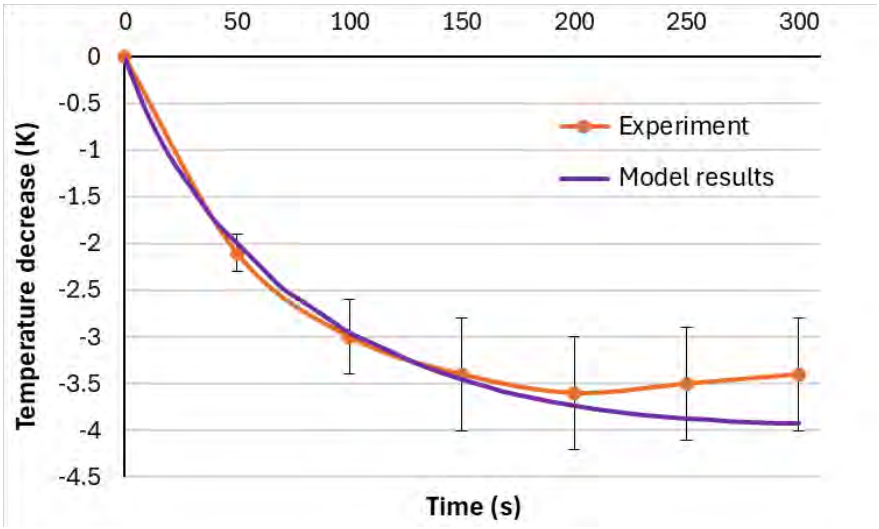

Figure 2-9. Experimentally determined liquid cooling, caused by treatment with the kINPen operating at 3 SLM, compared to the calculated temperature predicted by our model for the same geometry and conditions. The experiments were carried out in our previous work [126]. In that work, our previous model was not yet able to reach this agreement without applying a correction factor.

Note that in [126], such agreement between the model and the experimental data was not yet achieved, and implementation of a correction factor was necessary to prevent large overestimation of the evaporative cooling at the gas-liquid interface in the model. Briefly, the earlier overestimation stemmed from assuming $J_{H_2O} = J_{z,H_2O}$, i.e. the total axial flux of H_2O at the interface, as described in [124], which is an overestimation for a non-flat surface due to the large contribution of fluid flow in the axial direction.

Although the temperature differences in the liquid are only a few degrees for the cases investigated above, the inclusion of evaporative cooling in the model is important. Indeed, heat loss by evaporative cooling will balance the heat supplied by the gas that was heated by the plasma discharge (e.g. for the kINPen, as discussed above, the gas temperature at the nozzle is ±327 K). When neglecting evaporative cooling, the model instead predicts a large temperature increase in the liquid that does not correspond to experimental measurements at all (see Appendix B). At the same time, one may wonder why we should go through the trouble (and extra computational cost) of accounting for the calculation of temperature in the model at all, as the temperature changes in the liquid are small and, as discussed above, the gaseous temperature variations do not affect the flow profile. Indeed, several other published models that simulate a plasma

jet above liquid water do not simulate heat transfer in the system. However, accounting for changes in temperature is especially important for a model that wishes to simulate the transfer of chemical species across the gas-liquid interface. Indeed, the solubility of a species is determined by its Henry's constant, which is very temperature dependent. Specifically, a temperature difference of 10 degrees (i.e. the approximate difference between a few degrees of cooling versus a few degrees of heating of the treated liquid) can correspond to a Henry's constant that is twice as large for some species [153].

3.4 Mass transport across the gas-liquid interface

Finally, an aspect of the model that requires substantial validation is the description of mass transport across the gas-liquid interface. This validation will not be shown here, however, and instead forms the subject of Chapter 5, as it reveals an issue with standardisation and benchmarking in plasma-liquid modelling that goes beyond only the current model.

4. Conclusion

In this chapter, we have presented the computational 2D-axisymmetric fluid model developed for much of the research in this thesis. The model calculates the flow field in the system, specifically the treatment of a liquid in a well with a plasma jet, based on the kINPen. Using this calculated flow field, the model describes the transport of both heat and mass throughout the system. This allows us to investigate, e.g., mixing of the feed gas with the surrounding atmosphere, a crucial aspect of treatment with a plasma jet that determines in large part the production of RONS in the plasma and, by extension, the treatment, as well as the accumulation of RONS in the treated liquid.

In the next three chapters, we will employ this computational model to gain more insight into how the chosen treatment setup can influence the conditions in the effluent of the jet (Chapters 3 and 4), as well as how the choice of boundary condition at the gas-liquid interface can influence the accuracy of a computational model that aims to investigate plasma-liquid interaction (Chapter 5).

Chapter 3

Liquid treatment with a plasma jet surrounded by a gas shield: Effect of the treated substrate on the plasma effluent conditions

The content of this chapter is based on:

Liquid treatment with a plasma jet surrounded by a gas shield: effect of the treated substrate and gas shield geometry on the plasma effluent conditions
Pepijn Heirman, Ruben Verloy, Jana Baroen, Angela Privat-Maldonado, Evelien Smits and Annemie Bogaerts
J. Phys. D: Appl. Phys., 57, 115204 (2023)
https://doi.org/10.1088/1361-6463/ad146b

During treatment of a well plate with an atmospheric pressure plasma jet, reactive species are largely produced through the mixing of the jet effluent with the surrounding atmosphere. To control the atmosphere, a shielding gas can be applied. However, the interplay between the gas shield and the well geometry has not yet been investigated. In this chapter, we use our 2D-axisymmetric computational model of the kINPen plasma jet to study the mixing of the jet effluent with the surrounding atmosphere, with and without gas shield. Our computational and experimental results show that the choice of well type can have a significant influence on the effluent conditions, as well as on the effectiveness of the gas shield. These results provide a deeper understanding of how the choice of setup geometry can influence the plasma treatment, even when all other operating parameters are unchanged.

1. Introduction

As was explained in Chapter 1, in a plasma jet that uses a noble gas as the feed gas (like the kINPen) the produced RONS can originate from two possible sources: either from impurities (or deliberate admixtures) in the feed gas [75, 76], or from mixing of the plasma effluent with the surrounding atmosphere [77]. The latter makes plasma treatment with an APPJ susceptible to the ambient conditions during treatment, such as the relative humidity [154], which determines how much water can diffuse into the active plasma zone. This, in turn, plays a role in the RONS production and treatment reproducibility. To prevent this, a shielding gas device can be employed. First introduced in the context of plasma medicine by Reuter *et al.* [108], a gas shield induces a second, concentric gas flow that surrounds the jet and separates the plasma effluent from the surrounding air. The composition of the shielding gas can be controlled, thus allowing control over the gasses that are in contact with the plasma effluent. Since its introduction, the use of a gas shield with different gas compositions has been the subject of several studies. Although its effect on the RONS deposited in a treated liquid and its effect on treated cells has been examined [155, 156], its effect on RONS production in the gas phase is usually analysed with operation of the free jet, i.e., without a substrate being treated. In fact, most diagnostic investigations of the kINPen plasma and its effluent have been performed on the free jet, without accounting for the effects caused by the presence of a substrate [80].

For the kINPen, and plasma jets in general, multidimensional models have been developed to study e.g. mixing of the jet effluent with ambient species [105, 117] and how RONS production is affected by e.g. flow rate [116] or molecular admixtures [76]. The influence of using a gas shield has also been investigated computationally [108, 120, 121, 157]. Like gas phase diagnostics, however, these computational investigations are often performed for the free jet, without a substrate, though some computational efforts to investigate the interaction of a plasma jet with a liquid substrate have been reported. [124-127]. We previously discussed that most biomedical research is still performed *in vitro* [83, 158], where cell treatment is typically performed in well plates of varying sizes. Treatment of a well plate with a plasma jet, as opposed to e.g. a flat surface, inherently causes a backflow towards the jet outlet, of which the flow pattern logically depends on the well geometry. This backflow may in turn influence the dynamics of both the jet effluent and, when used, the shielding gas. Moreover, the gas flow over the liquid (as cells *in vitro* are usually covered by a liquid layer such as cell

medium) causes evaporation, which forms an additional source of water vapour that can affect the chemical pathways in the effluent, and thus the plasma treatment [90, 122].

In this chapter, we investigate how *in vitro* treatment with a plasma jet is affected by the choice of the used substrate (i.e. well size), as well as the interplay of this effect with a gas shield during treatment. For this purpose, we use our computational 2D-axisymmetric model of the kINPen plasma jet above a liquid water surface, outlined in Chapter 2, with and without a shielding gas device. Simulations are performed for various ambient conditions, such as temperature and relative humidity. This allows us to assess whether the gas shield is effective in eliminating variation caused by the ambient conditions for different setup geometries.

2. Methods

2.1 Computational methods

The modelling approach used in this chapter is the same as that described in Chapter 2, with some small changes. The most substantial change is the inclusion of a shielding gas device into the geometry of the model, which in practice means that a second gas inlet is introduced into the model at a larger radial position compared to the plasma jet inlet. Note that the simulations performed in this investigation were performed with a previous version of the model, which was built in COMSOL version 6.0 [140]. More information on the difference between both model versions is provided in Appendix C.

Figure 3-1 shows the simulated geometry. The geometry of the shielding gas device is based on a commercially available gas shield made by Neoplas GmbH specifically for the kINPen. The dimensions of the treated well in Figure 3-1 are those of a 24-well plate containing 1 mL of liquid, though different well sizes are used throughout this chapter. For each of the well geometries, the shape of the gas-liquid interface in our model is based on observations made in our lab for the same setup geometry. As mentioned in Chapter 2, a liquid surface is deformed because of the impinging gas from the plasma jet, causing a dimple of which the shape and depth depend on the well size [141]. As we focus mainly on the effect of the substrate geometry on the gas phase dynamics, the assumption of treating the liquid surface in the model as stationary will not significantly influence our results. The distance between the jet nozzle and the liquid surface (in its original state) is 20 mm. We use a gas flow rate of 2 SLM for the jet, and 4 SLM for the

gas shield (when applied). We selected these conditions to make sure that, in the experiments performed with this geometry, there would be no liquid splashing out of the well, and the jet would operate in a non-touching regime, i.e. no direct discharge onto the liquid occurs. Both phenomena would significantly complicate the modelling description. The gas shield inlet supplies dry air (79% N_2, 21% O_2) into the system, at the same temperature as the surrounding atmosphere.

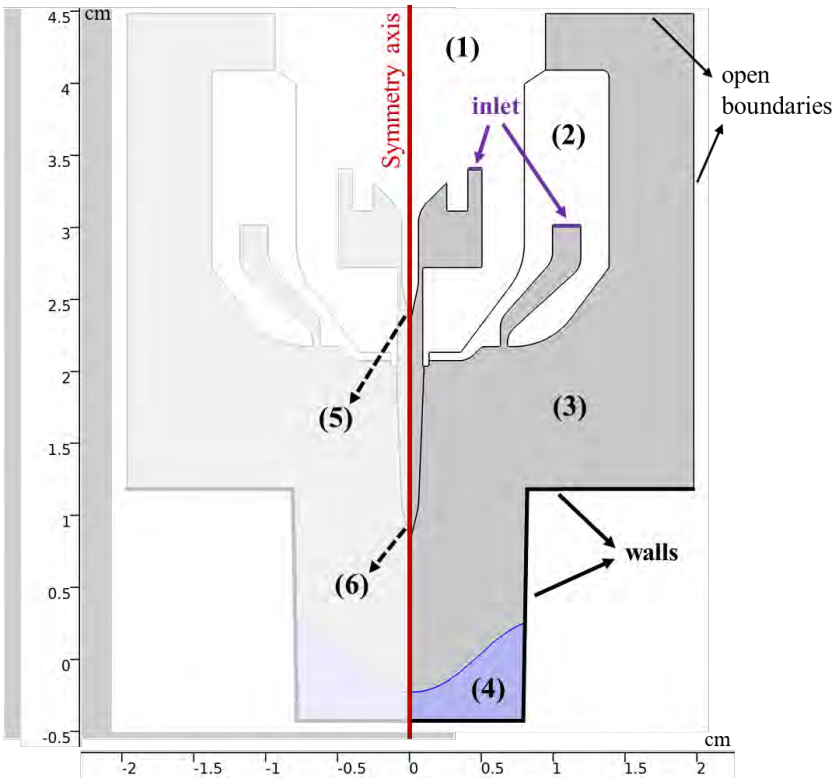

Figure 3-1. General model geometry of the 2D-axisymmetric fluid dynamics model as used in this chapter. Note that this figure is similar to Figure 2-1, the difference being the inclusion of the shielding gas device. The geometry components are (1) the plasma jet, (2) the shield gas device, (3) gas phase and (4) liquid phase. The pin-electrode (5) and approximate shape of the plasma plume (6) are also indicated for clarity. The boundary conditions applied at the edges of the model are indicated. As the geometry is 2D axisymmetric, only the right part is simulated by the model, with the symmetry axis indicated in red.

Using this model, we will study the species that typically lead to RONS formation in this system, i.e. the surrounding O_2, N_2 and H_2O, and their mixing with the feed gas from the jet. In this way, this chapter aims to provide a deeper understanding of how the choice of setup geometry, like the treated well and the use of a gas shield, can influence the

treatment even when all further operating parameters (which define the plasma discharge) are unchanged. The modelling approach is as follows: first, we calculate the stationary state of the flow field in the system. Using this stationary flow field as the input, we simulate the temperature and transport of species in the system in a time-dependent manner, for a treatment of 10 seconds. These simulations are performed for different geometries, i.e. for different wells with or without gas shield, to elucidate their effect on the plasma jet effluent conditions.

2.2 Experimental methods

Experiments were performed with the kINPen® MED to validate the computational results, using the same setup geometry as in the simulations, i.e. 2 SLM Ar flow rate with a 20 mm gap between the kINPen nozzle and the liquid surface. The treatment time was 60 s in all experiments. Afterwards, deionised water was added to counter evaporation. Specifically, we compared the liquid volume in the different well types before and after treatment, showing that the treatment caused the evaporation of up to 2% of the liquid during the applied treatment time.

Concentrations of long-lived RONS (H_2O_2, HNO_2 and HNO_3) were determined after treatment of a 12-, 24-, 48-, and 96-well plate (respectively 665180, Greiner; 10062-896, Avantor; 677180, Greiner and 655180, Greiner), containing 2 mL, 1 mL, 0.5 mL and 0.1 mL phosphate-buffered saline (PBS) per well, respectively. These volumes are typically used in experiments, as e.g. outlined in the standardised protocol by Tornin *et al.* [82], and correspond to solution depths of ca. 0.5 cm for the 12-, 24- and 48-well plates, and ca. 0.3 cm for the 96-well plate. Experiments were performed on three separate days, with three technical replicates each. Quantification of H_2O_2 in plasma-treated PBS (pPBS) was performed with the Fluorometric Hydrogen Peroxide Assay Kit from Sigma-Aldrich (MAK165-1KT), according to the supplier's instructions. The samples were diluted according to a 1:100 ratio in untreated PBS. The fluorescence intensity was measured at an excitation wavelength of 540 nm and an emission wavelength of 590 nm with the Tecan Spark Cyto 600. A standard curve was used to determine the concentration.

For HNO_2 and HNO_3, quantification in pPBS was done with the Nitrate/Nitrite Colorimetric Assay Kit from Cayman Chemical (780001), according to the supplier's instructions. The samples were not diluted, except for the samples treated in a 96 well, which were diluted according to a 1:10 ratio in untreated PBS. The absorbance was measured at 540-550 nm with the Tecan Spark Cyto 600. Calibration curves were used to determine the concentrations.

3. Results and discussion

3.1 General modelling case

As the general case in our investigation, we chose the treatment of a 24-well plate containing 1 mL of liquid. Figure 3-2a shows the calculated stationary flow field in the gas phase, both without and with the gas shield (left vs right panel). As expected, the gas flow out of the shielding gas device completely envelopes the plasma effluent. As shown previously [126], without a gas shield the Ar flow from the jet quickly displaces the gas that was initially in the well. This does not mean that the well becomes completely devoid of air; the vortex created in the well traps some of the surrounding air and mixes it with the effluent, keeping e.g. the N_2 density in the well around 1.8 x10^{17} cm^{-3}. Adding a gas shield provides a constant inflow of air into the well, keeping the concentrations of O_2 and N_2 much higher, as shown in Figure 3-2b.

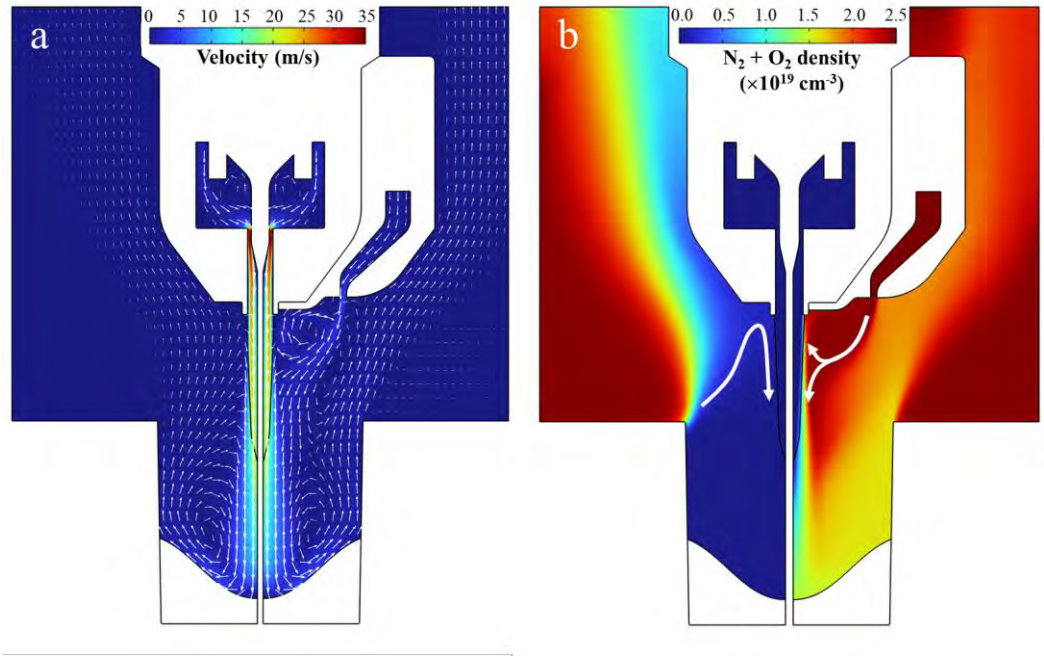

Figure 3-2. Calculated flow field (a) and air density (b) for the treatment of a 24-well plate, without (left panels) and with (right panels) gas shield. In (a), white arrows represent the flow field vectors, while in (b) they represent the main paths through which air mixes with the jet effluent. The liquid phase in the well is depicted in white.

3.1.1 N_2/O_2 in the plasma effluent

The kINPen produces a plasma plume of around 10 mm starting from the outlet of the jet nozzle. In this region, ambient species N_2, O_2 and H_2O are converted by electron impact reactions or reactions with excited Ar atoms into the primary reactive species that drive the RONS formation in the effluent [86]. For this reason, we are most interested in the conditions in the immediate effluent of the jet, resulting from mixing of the plasma effluent with the ambient. Because of the high velocity of the gas flow exiting the jet, axial convection is the dominant transport mechanism over radial diffusion, even when turbulent mixing is taken into account. We can thus expect strong radial concentration gradients in this region. To obtain a picture of the entire effluent as opposed to, e.g., only the very centre on the symmetry axis, we focus on the conditions at five different radial positions spanning the entire width of the jet nozzle. Figure 3-3a depicts the N_2 number density at these five radial positions, as a function of distance from the pin electrode. O_2 is not depicted here, but behaves in the same way as N_2, with absolute values four times lower, reflecting the N_2/O_2 ratio in air. Near the edge of the jet effluent, at r = 0.75 mm, the N_2 number density rises very steeply immediately when the gas exits the jet nozzle (see first vertical dotted line). The ambient N_2 however only reaches the centre of the effluent near the end of the plasma plume (second vertical dotted line). The number density does reach the same level over the entire width of the effluent before the gas flow reaches the liquid surface.

With a shielding gas (Figure 3-3b), we can see the same qualitative behaviour, but the gas shield significantly increases the absolute number densities of N_2 (and by extension, O_2) in the effluent. It is not surprising that the addition of a gas shield causes an increase of the number density of these species, especially near the edge of the jet effluent. However, even in the core plasma region the difference reaches up to two orders of magnitude, depending on the axial position. In diagnostic investigations of the kINPen, a gas shield is sometimes used not to exclude influence from the surrounding atmosphere, but to simulate the presence of a surrounding atmosphere of known composition [154], or to provide a surrounding atmosphere when directing the jet into a closed-off chamber for e.g. FTIR measurements [100, 159, 160]. Our simulations reveal that mixing of the jet effluent with the gas surrounding is significantly enhanced in the entire plasma effluent, when that surrounding gas originates from a gas shield as opposed to the ambient atmosphere. This means that caution must be taken when diagnostics in the presence of a gas shield are compared to experiments without a gas shield, as they do not entail the same (quantitative) conditions in the active plasma zone.

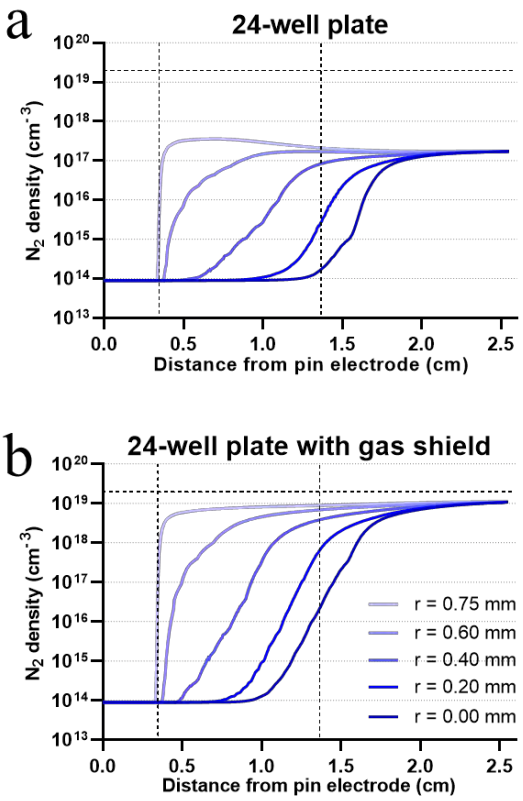

Figure 3-3. Calculated N_2 number density in the jet effluent without (a) and with (b) a shielding gas. The first (x = 0.35 cm) and second (x = 1.35 cm) vertical dotted lines indicate the jet nozzle and the end of the plasma plume, respectively, while the horizontal dotted line indicates the number density in the surrounding air (1 atm and 293 K).

3.1.2 H_2O in the plasma effluent

The main incentive to employ a gas shield is to limit the variation caused by different atmospheric conditions. The concentration of water in the atmosphere depends on the temperature and relative humidity. Hence, unlike O_2 or N_2, the amount of H_2O that mixes with the kINPen effluent can change from day to day, irrespective of the setup. The presence of H_2O substantially influences the CAP chemistry and can change the biological effects of CAP treatment [154, 161].

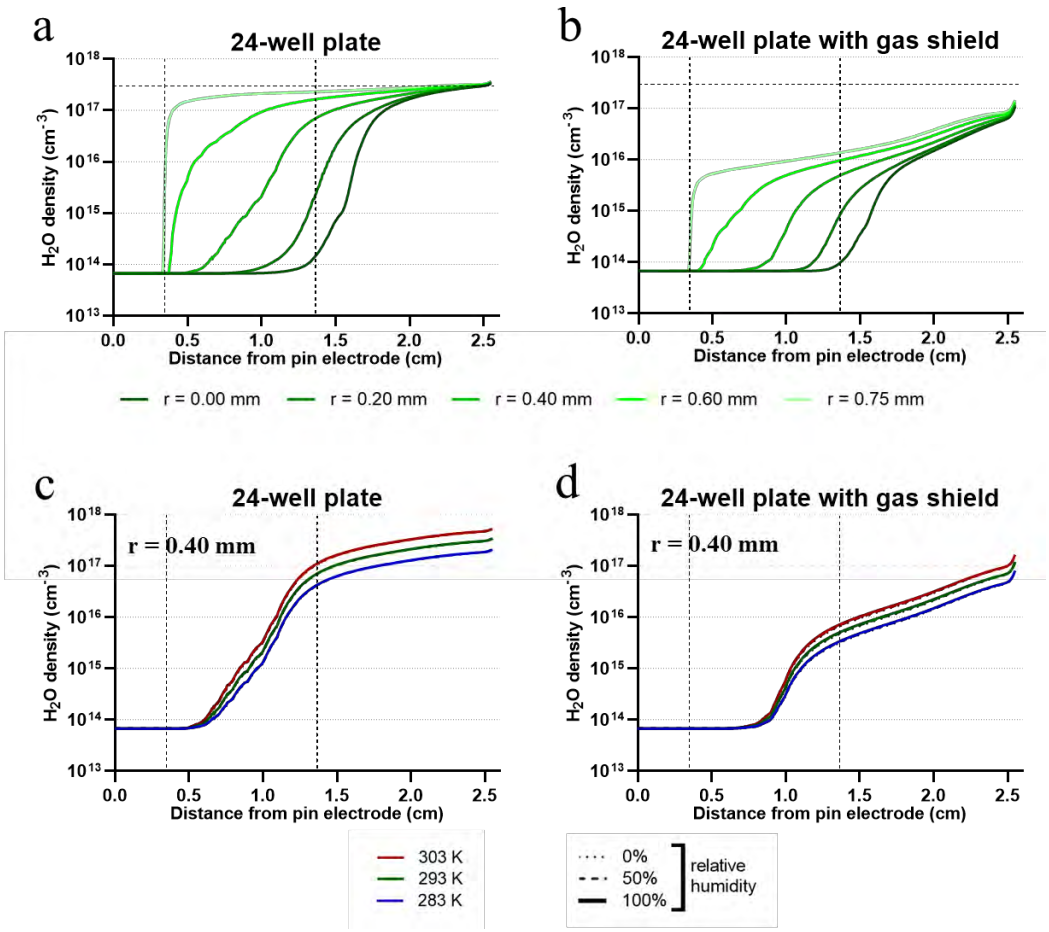

Figure 3-4. Calculated H_2O number density in the jet effluent, for different radial positions (a and b) and different ambient conditions (c and d). Results are shown for the case without (a and c) and with (b and d) gas shield. The first (x = 0.35 cm) and second (x = 1.35 cm) vertical dotted lines indicate the jet nozzle and the end of the plasma plume, respectively. The horizontal dotted line, indicating the number density in the surrounding air (at 1 atm and 293 K), is only shown for a and b, as it changes for different conditions. The different relative humidities in c and d overlap.

Figure 3-4a and b illustrate the mixing of ambient H_2O with the plasma jet effluent in the same way as plotted for N_2 in Figure 3-3, i.e., for different radial positions. In addition, to assess the efficacy of the gas shield in eliminating variation caused by the surrounding humidity, we performed these simulations for three different ambient temperatures (283 K, 293 K, and 303 K) and for three different ambient relative humidities (0%, 50% and 100%), yielding a total of nine conditions. The results are shown in Figure 3-4c and d. For clarity, only the density at a radial position of 0.4 mm is shown here, halfway

between the centre and the edge of the plasma jet effluent. The changes at this radial position can be used as a measure for the other radial positions in the effluent, as observed in Figure 3-4a and b.

Two main conclusions can be drawn from Figure 3-4. First, we can see that the gas shield reduces the H_2O concentration throughout the effluent. Indeed, since the gas shield is composed of dry air, it causes the H_2O concentration in the effluent to drop up to a factor 20 compared to the case without gas shield. Still, as observed from Figure 3-4d, it does not eliminate the variation in the H_2O concentration caused by different ambient conditions. In fact, the relative difference stays unchanged: both with and without the gas shield, there is a factor 3 difference between H_2O density in the effluent at an ambient temperature of 283 K and 303 K. A second observation is that the ambient temperature is by far the main cause of the different H_2O densities in the effluent, both with and without the gas shield. While the temperature determines which H_2O concentration in the air corresponds to a certain relative humidity, our model predicts almost the same rise in H_2O density for 0% and for 100% relative humidity at each temperature. Therefore, the atmospheric water vapour cannot be the cause of the variation we see across different ambient conditions tested in the model (cf. Figure 3-4c and d).

An additional source of H_2O in this treatment setup is the water that evaporates from the treated liquid surface. As gas from the jet flows over this surface, it takes with it the vapour that is present just above the surface and mixes it into the vortex present in the well. The vapour pressure of water is determined by the temperature, implemented into our model via Antoine's law. To confirm that it is the evaporated water that gives rise to the H_2O present in the jet effluent as opposed to the ambient water, we adapted our model so that it treats the H_2O originating from different sources (i.e. from impurities in the feed gas, from the ambient atmosphere and from evaporation at the liquid surface) as different species. The results are presented in Figure 3-5. Indeed, most of the water vapour in the jet effluent is evaporated H_2O from the treated liquid. Even without the gas shield, the ambient H_2O is kept relatively far away from the effluent, due to the backflow created by the well. In a way, this backflow induced by treatment of a well already acts as its own gas shield. Implementation of the actual shielding gas device then enhances the shielding effect, keeping ambient species even further away from the effluent (cf. Figure 3-5a). Additionally, the gas shield changes the flow field so that most evaporated water is guided outside of the well, decreasing the concentration of water vapour in the jet effluent (cf. Figure 3-5b).

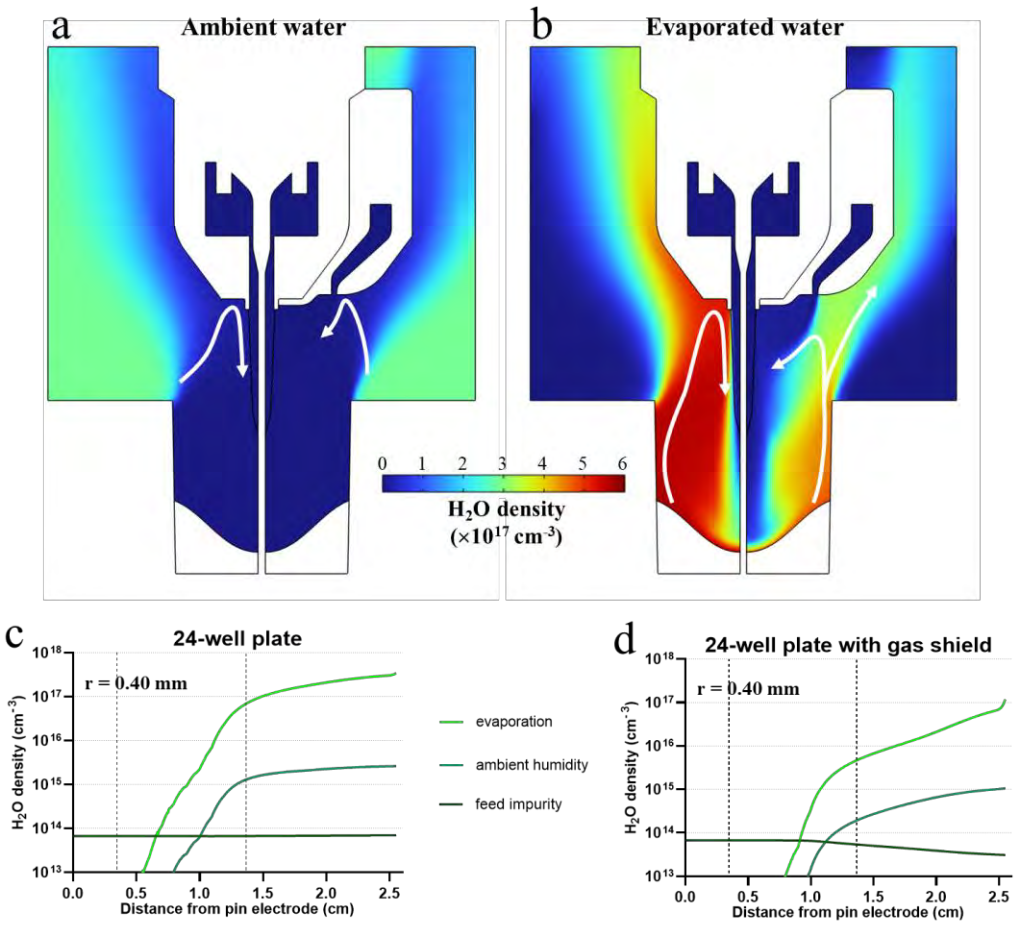

Figure 3-5. Calculated H_2O number density in the jet effluent originating from different sources. 2D profiles show the H_2O originating from the ambient humidity (a) or evaporation (b), both without and with gas shield. White arrows represent the main paths through which water mixes with the jet effluent. 1D profiles show the number densities originating from the different sources, i.e., ambient humidity, evaporation, and feed impurity, at a radial distance of 0.4 mm, without (c) and with (d) gas shield. The liquid phase in the well is depicted in white.

Apart from using a gas shield, another approach that can be used to reduce the effect of (different amounts of) water vapour in the ambient is by admixing H_2O into the feed gas of the plasma jet, in much larger amounts than the impurity levels typically already present. It was shown in literature that this admixed water vapour has a much larger influence than different humidities surrounding the effluent [159], effectively making a variation in ambient humidity less relevant. When humidifying the feed gas (or shielding

gas), the humidity should however still be actively controlled with e.g. a hygrometer [159], in order to obtain precise, reproducible treatments. Usually, H_2O admixtures are introduced into the feed gas of a plasma jet by leading (part of) the dry feed though a water bubbler. Since the vapour pressure of the water, and thus the amount of gaseous H_2O, depends on the temperature, different ambient temperatures can still influence the amounts of H_2O in the plasma, unless the bubbler is temperature controlled. In addition, depending on the liquid volume, continuous evaporation from the bubbler will cause the liquid water to cool down, changing the amount of H_2O in the gas over time. In practice, the kINPen is mostly used without admixed H_2O, and feed gas impurity forms only a small contribution. In these cases, most of the H_2O entering the active plasma zone originates from the ambient, and even more from evaporated water when treating a liquid-filled well (cf. Figure 3-5; note the logarithmic scale). Thus, it should be kept in mind that different ambient conditions, and especially the temperature, can cause variations in the treatment [154].

3.2 Effect of the treated well size

In the previous section we demonstrated that the backflow created by the treated well plays a role in determining the conditions in the plasma jet effluent, as it can induce a "self-shielding" effect. In literature, different well sizes are used for treatment of liquid and/or cells with a plasma jet. For the generation of plasma-treated liquids, even larger containers like beakers or petri dishes are often treated. To investigate the effect of the substrate geometry, we simulated the plasma jet over a 12-, 24-, 48-, and 96-well plate.

3.2.1 Well size effect without gas shield

In this section, we investigate how the geometry of the treated well influences the conditions experienced by the plasma jet, and thus the treatment itself. Figure 3-6a shows the N_2 density as calculated for the treatment of the four different well sizes, without a shielding gas. To indicate how the well geometry influences the flow field, we also show the main streamlines originating from the jet.

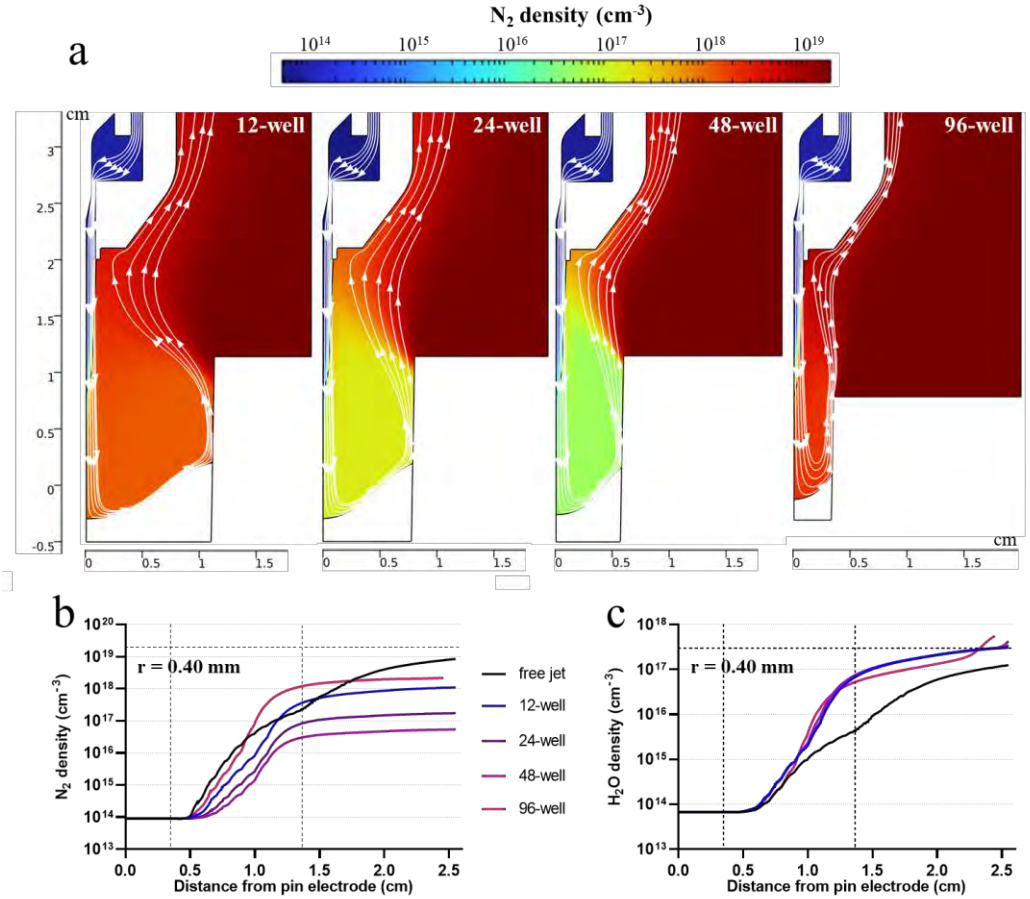

Figure 3-6. Influence of the well type on the flow field and N_2 density in 2D (a), and on the N_2 (b) and H_2O (c) density profiles in the jet effluent in 1D, without a shielding gas at 293 K. The flow lines in (a) originating from the jet are plotted in white. In (b) and (c), comparison is also made with the result for a free jet. The H_2O density curves for the 12-, 24- and 48-well plates overlap, since the plasma effluent mainly mixes with evaporated water from the well. The liquid phase in the wells is depicted in white.

Figure 3-6b and c depict the density of N_2 and H_2O in the jet effluent between the pin electrode and the liquid surface, for the different well types, as well as for a free jet. The difference in behaviour with the free jet (i.e. without well plate) will be discussed at the end of this chapter. Like in Figure 3-5, densities are shown for a radial position of 0.4 mm, but the behaviour can be extended to the entire width of the effluent (cf. Figure 3-3). Clearly, the chosen well type significantly affects the N_2 density in the gas phase. As the well diameter decreases, the vortex in the well becomes more confined. This causes

an increase in the velocity by which the backflow exits the well, and directs the backflow less towards the jet, effectively improving the "self-shielding" effect of the well-induced backflow. As a result, less ambient species, like N_2, enter the well and mix with the effluent. This trend is clearly visible up to the 48-well plate. For the 96-well plate, however, the N_2 density in the well and the effluent is the highest of all simulated wells. The reason for this is twofold. First, because the well is so small, the gas flow is more turbulent than for the other wells, causing more turbulent mixing in the region between the well interior and the surrounding gas. For example, the gas flow exiting the 48-well plate has a maximum turbulent dynamic viscosity of 1.8×10^{-4} Pa·s, while for the 96-well plate this is 7.1×10^{-4} Pa·s, causing a factor 9 and a factor 32 increase, respectively, in the diffusivity of N_2 over the normal molecular diffusion constant (cf. Chapter 2). Secondly, whereas the other well types have the same depth (16.5 mm), a 96-well plate is more shallow (10.9 mm). Mohades *et al.* [119] have previously shown that the so-called rim-height of a well influences the amount of ambient gas that enters it, when treated with a plasma jet. As this rim height is lower for the 96-well plate than for the other investigated well plates, more N_2 is able to reach the interior of the well. It should be noted that, since the rim height depends on the amount of liquid in the well, the results from Figure 3-6b will be quantitatively different for smaller or larger liquid volumes. Indeed, more liquid will result in a lower rim height, causing more ambient gas to enter the well. We here investigated only the volumes typically used in experiments, as e.g. outlined in the standardised protocol by Tornin *et al.* [82].

While the N_2 in the effluent originates from the surrounding atmosphere, the H_2O in the effluent is mainly evaporated water from the treated liquid, as explained in the previous section. As the simulations were performed for the same temperature and thus the same vapour pressure, the H_2O densities in the effluent are similar regardless of the well type. Hence, the curves overlap, with only a small difference for the 96-well plate.

3.2.2 Experimental validation

To assess whether the change in effluent conditions caused by the well geometry in fact leads to a different treatment result for the treated liquid, we measured the concentration of long-lived RONS, i.e., H_2O_2, HNO_2 and HNO_3, in PBS after 60 s of treatment with the kINPen. Figure 3-7a shows the measured number of moles of each measured species in the different wells. As can be seen, the smaller wells take up less RONS. Yan *et al.* [162] also showed that the choice of well type, when treating a liquid with the kINPen, can change its reactive species uptake, and we see the same trend as the one they reported [162]. However, while Yan *et al.* [162] attributed the lower species

uptake by the smaller wells to the decreasing surface area through which the liquid can exchange species with the gas, Figure 3-7b clearly demonstrates that this cannot be the only explanation. If the surface area was the only cause, the RONS uptake per unit of surface area should be the same for each well type. Instead, more RONS seem to be taken up by the liquid in the smallest well per unit of surface area than by the largest well, and the surface area of the liquid and its reactive species uptake do not vary in the same way for the different well plates. Indeed, whereas the 12-well plate contains twice as much H_2O_2 as the 48-well plate, its liquid surface area is four times as large. Since the uptake of a species by a liquid is determined by the concentration of that species above the liquid surface, this indicates that the concentrations of the species in the gas phase above the liquid are different, even though the sole difference is the type of well that is treated.

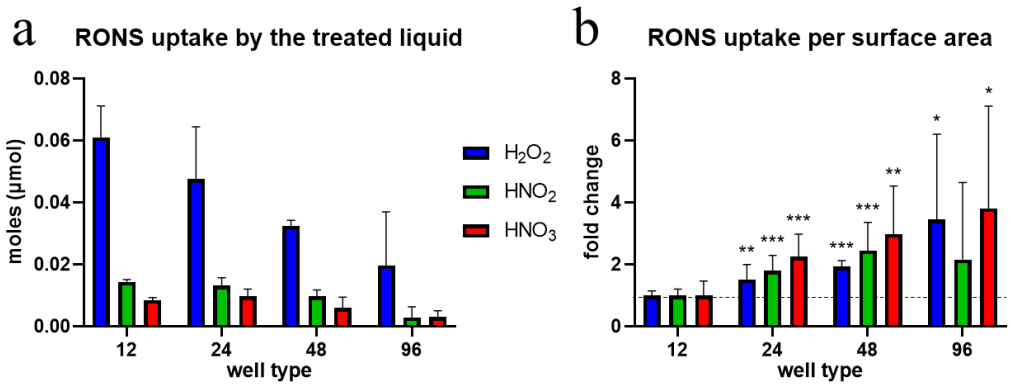

Figure 3-7. Experimentally measured RONS in the treated liquid for different well types, in absolute number of moles (a), and per unit of liquid surface area (b). Data is shown as the mean value and standard deviation of the replicates. For easy comparison between the different well types, the RONS uptake per surface area is plotted as fold change with respect to the 12-well plate, and the statistical significance of this difference is indicated (* = $p < 0.05$, ** = $p < 0.01$, *** = $p < 0.001$). Note that due to their different size, the wells contained different volumes of liquid (cf. Section 2.2), meaning that the number of moles and the concentration do not follow the same trend. For instance, while the number of moles H_2O_2 as measured in a 12- and 48-well plate is 0.06 µmol and 0.032 µmol, respectively, their H_2O_2 concentrations after treatment are 30 µM and 65 µM.

The main chemical reaction leading to the formation of H_2O_2 in the gas phase by the kINPen is [103, 160]:

$$OH + OH + M \rightarrow H_2O_2 + M \quad \text{(R.3-1)}$$

Where M stands for a neutral collision partner, such as Ar. OH radicals are formed in the active plasma by the dissociation of water. It has been reported in literature that OH radical densities produced by a plasma jet correlate linearly with the H_2O density within a range relevant for the current study [160, 163]. From the results shown in Figure 3-7b, we can deduce that a smaller size of the treated well leads to a higher gas phase concentration of H_2O_2 above the liquid. However, since the H_2O density in the jet effluent is the same regardless of the well type, according to our model (cf. Figure 3-6), the rise in H_2O_2 production cannot be due to reaction (R.3-1). Contrary to H_2O, the calculated N_2 and O_2 densities in the effluent change significantly depending on the chosen well type (cf. Figure 3-6). Increasing levels of air entering the plasma will lead to increased production of primary and secondary RONS such as N and NO [86]. Both species in turn react with OH via the following reactions [101, 103]:

$$N + OH \rightarrow NO + H \quad \text{(R.3-2)}$$

$$NO + OH + M \rightarrow HNO_2 + M \quad \text{(R.3-3)}$$

These reactions will compete with reaction (R.3-1) and thus reduce the amount of H_2O_2 formed via OH radical recombination. This can explain the increasing H_2O_2 trend seen for the 12-, 24- and 48-well plate seen in Figure 3-7b. Indeed, decreasing N_2(/O_2) densities in the smaller well sizes can lead to a higher rate of reaction (R.3-1), due to less competition with reactions (R.3-2) and (R.3-3). On the other hand, the 96-well does not follow this trend. This is unexpected, since our model predicts the N_2(/O_2) density in the effluent to be the highest when treating a 96-well plate (cf. Figure 3-6), while experimentally the highest average H_2O_2 concentration was found in the liquid. It is possible that our model does not yet accurately describe all mechanisms at play. Especially for the 96-well plate, which is a very small system, certain assumptions in the model may play a larger role, such as the stationary liquid surface that may affect the flow field in the gas. Still, the trends seen for the other well types do agree well between our model and experiments. Additionally, chemical reactions in the liquid may influence the results. Indeed, plasma-treatment of PBS can cause formation of ClO^- through reaction of Cl^- with atomic oxygen [164]. H_2O_2 (and HNO_2) can, in turn, react with ClO^-, via e.g. the following reactions:

$$H_2O_2 + ClO^- \rightarrow Cl^- + H_2O + O_2 \quad \text{(R.3-4)}$$

$$NO_2^- + ClO^- \rightarrow Cl^- + NO_3^- \quad \text{(R.3-5)}$$

However, the kINPen, using Ar as the feed gas, leads to much smaller amounts of ClO^- in PBS compared to other CAP devices, e.g., the COST-jet operating with He/O_2 as feed gas [165]. In addition, Van Boxem *et al.* [103] showed the stability of H_2O_2 in PBS for 2 hours after treatment with the kINPen. Still, the possibility of a small production of ClO^- cannot be excluded. The surface-to-volume ratio of the liquid in the investigated wells (i.e. the surface through which RONS can enter the liquid, compared to the volume in which they can react) is nearly the same for all wells, except for the 96-well plate. Thus, this may be an additional reason why its results in Figure 3-7 do not follow the qualitative trend explained above.

Finally, it must also be noted that the experimental results for the 96-well plate in Figure 3-7 simply have a very large uncertainty. For example, the difference in HNO_2 uptake per surface area of the 96-well plate, compared to that of the 12-well plate, is not statistically significant. This large uncertainty can be explained in two ways. First, we showed in Figure 3-6 that, due to the higher turbulence and lower rim-height, more ambient gas mixes with the plasma effluent for the 96-well plate compared to the other well plates. This means that treatment of a 96-well plate will be inherently more susceptible to different relative humidities compared to the other well types. Second, the diameter of a 96-well is only 4.3 times larger than that of the kINPen nozzle. Small deviations from a perfectly centred position above the well may thus significantly influence the flow field in the well. As our model describes an ideal geometry, this may additionally form an explanation for why our model and our experiments do not follow the same trend for the 96-well plate only.

The trends plotted in Figure 3-7 for HNO_2 and HNO_3 are less straightforward to explain. Like for H_2O_2, the liquid takes up a higher amount per unit of surface area for decreasing well size, indicating higher gas phase concentrations. However, because the formation of HNO_2 and HNO_3 requires the presence of both N_2 and O_2, and the concentrations of these species in the effluent decrease with smaller well sizes, as shown in Figure 3-6b, one would expect HNO_2 and HNO_3 to follow this trend. Instead, however, we see the opposite. HNO_2 is mainly formed via reaction (R.3-3), while HNO_3 is formed through [101]:

$$NO_2 + OH + M \rightarrow HNO_3 + M \quad \text{(R.3-6)}$$

where NO_2 in turn is formed from NO. It was noted by Van Gaens *et al.* [97] that NO_2 production by the kINPen rises with increasing amounts of N_2 or O_2 only up to a certain point: above 0.1% O_2 content and 0.15% N_2 content, the NO_2 production decreases again. In addition, Mohades *et al.* [119] calculated lower concentrations of NO and NO_2 near the liquid in geometries where more N_2/O_2 from the ambient diffused into the well. Though both these observations are in line with the behaviour we see here, they cannot be directly compared. In [97], N_2 and O_2 were supplied to the jet as admixtures in the feed gas, while in [119] a different type of plasma jet was simulated. A more in-depth analysis will thus be necessary in the future to fully explain the observed trends.

Nevertheless, both our experimental and computational results show that the choice of treated well type can have a significant influence on the effluent conditions and, by extension, the treatment itself. This is important to keep in mind for plasma medicine applications.

3.2.3 Well size effect with gas shield

The question arises how the chosen well geometry impacts the effluent conditions when a gas shield is employed. Simulation results for these cases are depicted in Figure 3-8 in a similar way as Figure 3-6, for the different well types, as well as for a free jet. The difference in behaviour with the free jet will again be discussed at the end of this chapter. When implementing a gas shield, it is clear that the flow field changes drastically for different treated wells. An extreme case is the treatment of a 48-well plate. Because the edge of the well in this case is positioned at a similar radial position as the nozzle of the shielding gas device, the shielding gas does not blow into the well being treated, but instead into the wells surrounding it. The neighbouring well for the 48-well plate is shown in Figure 3-8a to illustrate this. It should be noted that this second well is in fact treated in the model as a ring-shaped cavity surrounding the treated well, because the model is axisymmetric. However, this still illustrates the effect on the neighbouring wells. For the other well types, Figure 3-8a shows the results of simulations without the neighbouring well present. In these cases, we also performed simulations that included the neighbouring well, but its inclusion had no effect on the results, and the flow did not enter the neighbouring well like for the 48-well plate.

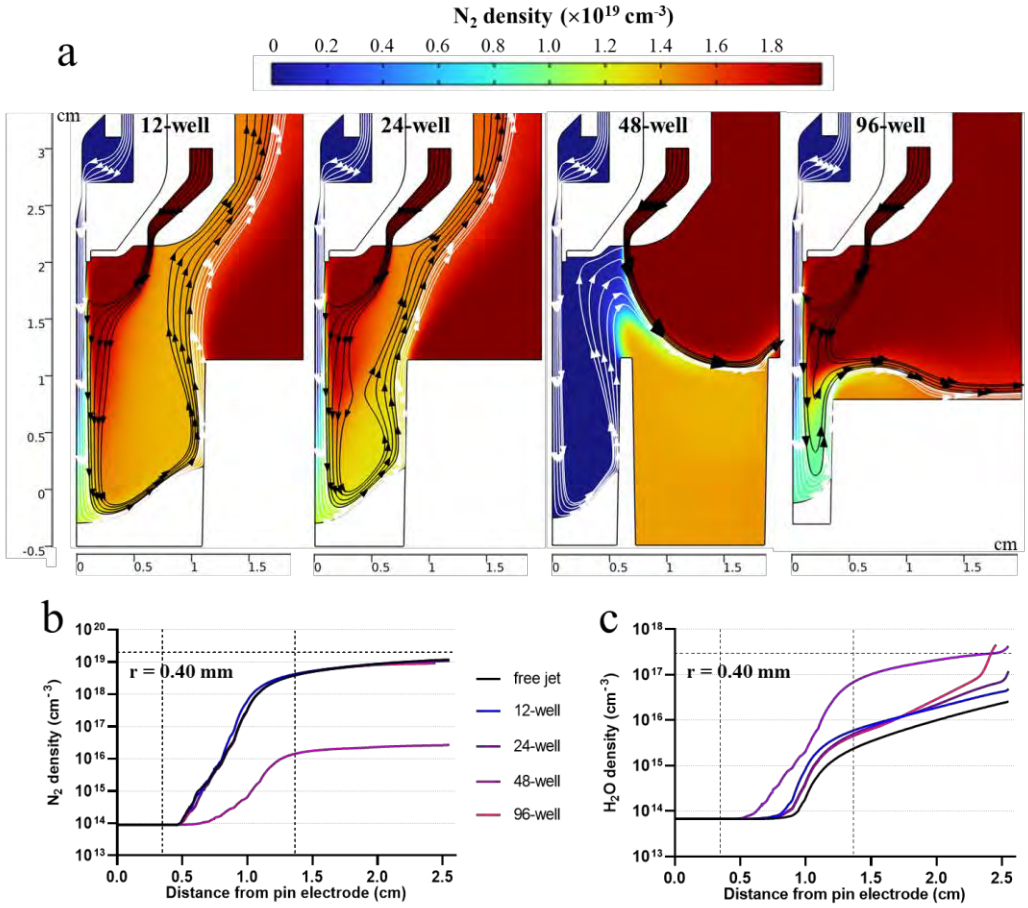

Figure 3-8. Influence of the well type on the flow field and N_2 density in 2D (a), and on the N_2 (b) and H_2O (c) density profiles in 1D, in the jet effluent, with a shielding gas at 293 K. The flow lines in (a) originating from the jet and the gas shield are plotted in white and black, respectively. In (b) and (c), comparison is also made with the result for a free jet with gas shield. For the 48-well plate, a neighbouring well is shown in (a), for clarity. For the other well types, the inclusion of a neighbouring well has no effect on the flow field. The N_2 density curves for the 12-, 24- and 96-well plates overlap, since the plasma effluent mainly mixes with air supplied by the shielding gas. The liquid phase in the well is depicted in white.

We can thus expect that for the 48-well plate the gas shield will not actually provide a shielding effect, as is clear from the flow field in Figure 3-8a. Indeed, when comparing Figure 3-8 with Figure 3-6 we can see that there is little difference between, respectively, the N_2 and the H_2O density for the 48-well with or without a gas shield. For the other wells, the shielding gas does envelop the plasma jet effluent. Because in these cases,

almost all N_2 that mixes with the effluent is supplied by the shielding gas, the N_2 density in the effluent is the same for the 12-, 24- and 96-well plate. The H_2O density is also very similar for these three well types. As discussed in Section 3.1, the H_2O that mixes with the effluent is mainly evaporated water from the treated surface. The H_2O density is lower with shielding, because the flow field caused by the shielding gas for the three wells is such that it guides the evaporated water away from the jet nozzle, instead of towards it like in the cases without shielding. Overall, our results indicate that the gas shield is indeed able to induce a controlled environment surrounding and mixing with the jet effluent, regardless of the treated well type, although in some cases, like for the 48-well plate in this setup, the substrate geometry can influence the flow field in such a way that the shielding gas does not at all behave as intended.

3.2.4 Unintended effects on neighbouring wells

The fact that the shielding gas blows into the wells surrounding the treated well, for the 48-well plate shown in Figure 3-8, does not only cause the gas shield to not operate as intended. Along with this shielding gas, much of the effluent from the plasma jet passes through the neighbouring well. This means that in this geometry, wells could be unintendedly affected by the treatment of other wells close by.

The RONS produced by a plasma jet can be divided into three groups [126]. These are (i) short-lived species, which quickly react away after the end of the active plasma zone (some even before reaching the liquid), (ii) long-lived species with a high Henry's constant (i.e., a high solubility), and (iii) long-lived species with a low Henry's constant. For a flow field such as that of the 48-well plate in Figure 3-8, short-lived species are unlikely to reach the neighbouring wells, because they react away quickly. Long-lived species with a high Henry's constant can survive long enough, but are also unlikely to reach the neighbouring wells because they will mostly be taken up by the liquid in the treated well, more so for higher Henry's constants. However, long-lived species with a low Henry's constant, that are thus only taken up by the treated liquid in small amounts, are able to reach the surrounding wells and dissolve in the liquid therein. To illustrate this, we performed simulations where a density of 10^{15} cm^{-3} O_3 was supplied at the inlet of the plasma jet, similar to produced amounts of O_3 reported in literature [86], while the neighbouring well (also shown in Figure 3-8a) was now filled with liquid. Figure 3-9a shows the O_3 density in the gas and liquid phase, for a 48-well plate. Indeed, the flow field in this case guides a substantial amount of O_3 to the liquid surface in the neighbouring well, where it subsequently dissolves.

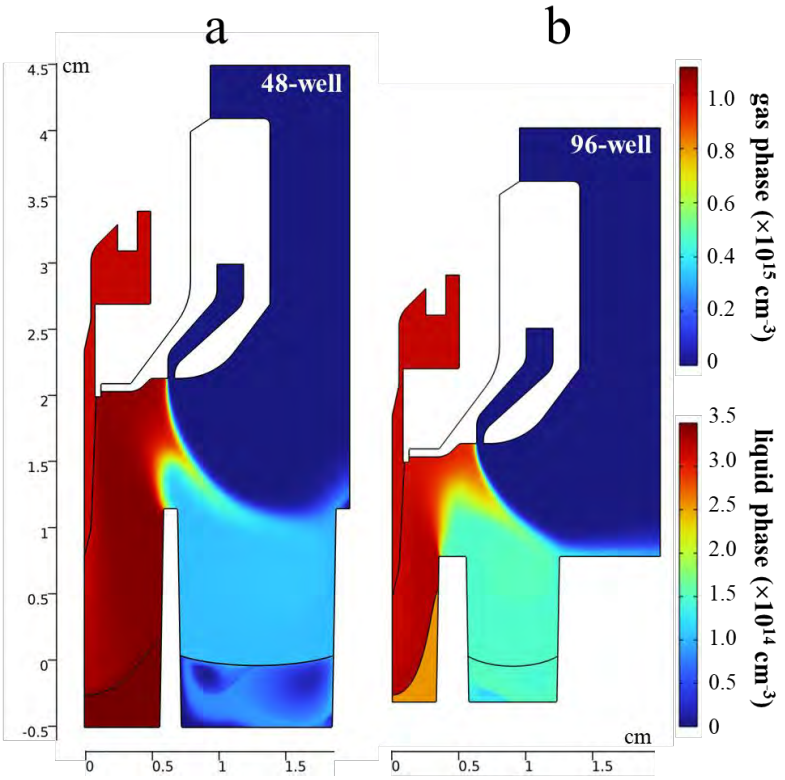

Figure 3-9. Ozone density in the gas and liquid phase of both the treated and neighbouring well when the setup geometry causes the shielding gas to blow into the wells surrounding the treated well. (a) 48-well plate with a treatment gap of 2 cm. (b) 96-well plate with a treatment gap of 1.5 cm. An ozone density of 10^{15} cm^{-3} is supplied by the jet, based on reported produced densities in literature [86].

The effect occurs when the radius of the treated well is comparable to (or smaller than) the radius of the gas shield nozzle, in combination with a strong enough backflow from the well to push away the shielding gas. For instance, for a 96-well plate with 20 mm gap between the liquid and the plasma jet nozzle, as discussed in Section 3.2.3, the flow does not affect the neighbouring well, while for a smaller gap of 15 mm, and thus a stronger backflow, the same effect as for the 48-well plate with 20 mm gap can be seen (cf. Figure 3-9b).

3.3 Comparison with the free jet

As is clear from the previous section, the choice of treated substrate will influence the treatment of the substrate itself. To emphasize this influence, Figure 3-6b and Figure 3-8b also showed the density profiles of N_2 and H_2O as calculated for the free jet, i.e., without treated substrate. To end this chapter, let us now take a closer look at these results. Due to the lack of a backflow from the treated well, the N_2 density without a shielding gas is significantly different for the free jet (cf. black curve in Figure 3-6b), which confirms again that caution should be taken when comparing results (like produced RONS densities) for the free jet with those gathered when treating a well. With a shielding gas, the N_2 density is independent of the well geometry (except for the 48-well), and the same as for the free jet, since in these cases most N_2 mixing with the effluent is supplied by the shielding gas, confirming again that the shield is able to create a controlled environment. However, it should be kept in mind that the effect is not the same as a controlled atmosphere around the jet.

The H_2O density without shielding is lower for the free jet than for the treatment of any well type, which is to be expected, since without a treated liquid surface no evaporated water is present, and all H_2O in the effluent stems from the ambient humidity. The density is however higher than the H_2O density coming from the ambient shown in Figure 3-5b, because the "self-shielding" effect caused by the induced backflow from the well is absent here. This also suggests that the free jet is far more susceptible to varying ambient humidity, which is confirmed in Figure 3-10a. Finally, with the gas shield, one would expect that the lack of an evaporating liquid surface beneath the jet, and the presence of a shielding flow separating the effluent from the ambient, would cause the H_2O density to barely rise above the impurity level in the feed gas. Surprisingly, as shown in Figure 3-10, the H_2O density is similar with and without a gas shield. The position from which concentrations start to rise is increased slightly, but by the end of the plasma plume (x = 1.35 cm) the densities are at the same level as without shielding gas. This would indicate that the gas shield does not actually provide efficient shielding of the jet effluent from the surrounding atmosphere at all. This is in contrast with existing literature, where the correct performance of a shielding gas has been confirmed experimentally [77]. In the following chapter, we will elucidate the reason for this discrepancy.

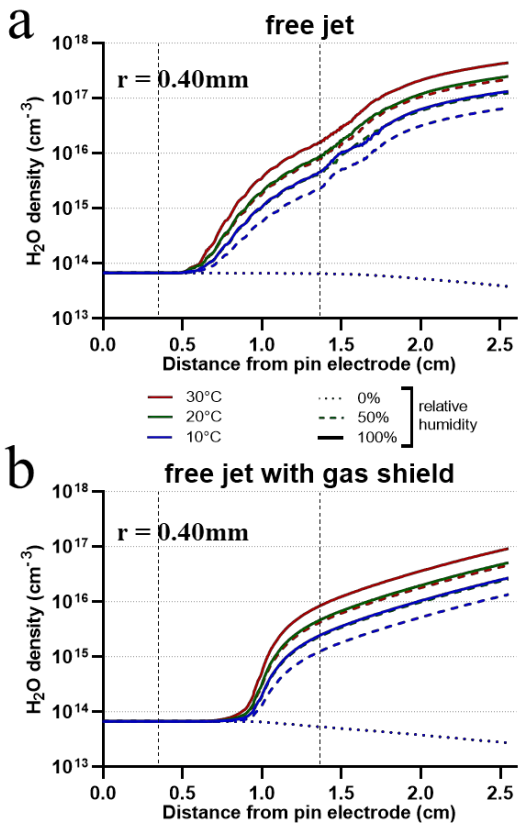

Figure 3-10. H_2O density in the jet effluent as calculated for the free jet, without (a) and with (b) gas shield, for three different ambient temperatures and three different relative humidities. As all water mixing with the jet originates from the ambient humidity, there is no rise in H_2O density for 0% relative humidity (see dotted line), and the curves for the three temperatures overlap.

4. Conclusion

In this chapter, we investigated how *in vitro* treatment with a plasma jet is affected by the geometry of the treatment setup, i.e. the chosen well type and the use of a shielding gas device. For this purpose, we applied our computational 2D-axisymmetric model of the kINPen jet above a liquid water surface, with and without gas shielding, to investigate the mixing of the plasma jet effluent with the ambient N_2, O_2 and H_2O. These molecules drive the formation of RONS by the plasma, and thus their mixing with the plasma determines the treatment effect. Simulations were performed for different ambient temperatures and relative humidities.

Both our computational and experimental results show that the choice of treated well type can significantly influence the effluent conditions and, by extension, the treatment itself. The backflow created by the treatment of a well plate plays a role in determining the conditions in the plasma jet effluent, as it can induce a "self-shielding" effect. Because this flow field depends on the size of the treated well, mixing of the plasma with the ambient will be different for different treated wells, causing changes in the RONS formation. Additionally, because the self-shielding keeps the surrounding atmosphere away from the plasma effluent, evaporation of water in the treated well forms the main contributor to the H_2O that enters the plasma plume.

The use of a shielding gas provides a consistent supply of gas and is able to induce a controlled environment surrounding and mixing with the jet effluent, regardless of the treated well type. However, in some cases, like for the 48-well plate in this setup, the substrate geometry can influence the flow field in such a way that the shielding gas does not at all behave as intended. When the radius of the treated well is comparable to (or smaller than) the radius of the gas shield nozzle, in combination with a strong enough backflow from the well, the shielding gas can be pushed away. In this case, the long-lived RONS with a low Henry's constant, such as O_3, may enter the wells surrounding the treated well, causing unintended effects of the treatment to these neighbouring wells. Furthermore, it should be taken into account that the flow of a gas shield can enhance the amount of N_2 and O_2 that mixes with the plasma effluent. This means that caution must be taken when comparing diagnostics in the presence of a gas shield to experiments without a gas shield, as they do not entail the same (quantitative) conditions in the active plasma zone.

Altogether, the results in this chapter provide a deeper understanding of how the choice of setup geometry, such as the treated well and the use of a gas shield, can influence the conditions in the plasma effluent and, by extension, the plasma treatment itself. We also found, however, when evaluating the simulation results for the jet without a substrate, that the shielding gas was predicted to not provide efficient shielding against the ambient atmosphere. This is an unexpected result, as the efficiency of using a shielding gas has previously been confirmed in literature. We will see in the next chapter that the geometry of the shielding gas device is the culprit, providing an additional way in which the setup geometry can influence treatment results.

Chapter 4

Effect of the gas shield geometry on the plasma effluent conditions

The content of this chapter is based on:

Liquid treatment with a plasma jet surrounded by a gas shield: effect of the treated substrate and gas shield geometry on the plasma effluent conditions
Pepijn Heirman, Ruben Verloy, Jana Baroen, Angela Privat-Maldonado, Evelien Smits and Annemie Bogaerts
J. Phys. D: Appl. Phys., 57, 115204 (2023)
https://doi.org/10.1088/1361-6463/ad146b

Since the first report of a gas shield, different designs have been employed in different works. However, the possible effects of this change in geometry on, e.g., mixing of the shielding gas with the plasma jet effluent have rarely been addressed. In this chapter, we use our 2D-axisymmetric CFD model of the kINPen plasma jet to study the performance of different shielding gas geometries. Our simulations reveal that the design of the shielding gas device can have a substantial effect on the conditions in the plasma effluent and the effectiveness of the shielding. These results reemphasize the importance of standardisation in plasma medicine research, as the use of different gas shields inhibits clear comparison of results across different works.

1. Introduction

At the end of the previous chapter, it became clear that the shielding gas device that we used in our investigation gave unexpected results. One would expect for the free jet with shielding gas, operating without a (liquid) substrate and the accompanying backflow caused by the well, that the H_2O level in the jet effluent would barely rise above the impurity level in the feed gas. Instead, we saw that there is still a large influence from the ambient, with different amounts of H_2O entering the plasma effluent depending on the ambient temperature and humidity. In fact, the conditions were not all that different compared to the free jet without the shielding gas.

When the use of a shielding gas in context of plasma medicine was first introduced in by Reuter *et al.* [108], experimental data confirmed that the gas shield performed as expected, and was able to shield the plasma effluent from the ambient atmosphere. Since then, several computational and experimental investigations of a shielding gas and its effect on the plasma treatment have been reported [108, 120, 121, 155-157]. However, many of these works do not use the same shielding gas device. Since its introduction, several different gas shield geometries have been depicted in literature [117, 156, 166], differing in both the position of the gas shield nozzle relative to the plasma jet nozzle, and the flow direction of the shielding gas compared to the plasma jet. However, the performance of these gas shields in excluding the surrounding atmosphere and their effect on the conditions in the plasma effluent have rarely been reassessed.

In this chapter, we elucidate the cause for the unexpected performance of the shielding gas device used in the previous chapter. In addition, we systematically investigate the effect of the gas shield geometry on its performance, and on how this changes the conditions in the plasma effluent.

2. Methods

2.1 Computational methods

To simulate only the effect of the gas shield geometry, we adapted the model from the previous chapter to simulate the free jet. Thus, the liquid phase and well geometry are removed, and the bottom edge of the model geometry is treated as an outlet for the gas flow, located at 3 cm from the kINPen nozzle. Other than that, the modelling approach is unchanged.

2.2 Experimental methods

Experiments were again performed with the kINPen® MED to support the computational results. Treatment was performed on a 24 well plate (Greiner; 10062-896) containing 1 mL of liquid, using 2 SLM argon flow rate with a 20 mm gap between the kINPen nozzle and the liquid surface. The treatment time was 60 s in all experiments. Afterwards, deionised water was added to counter evaporation.

2.2.1 Determination of RONS in the treated liquid

Concentrations of long-lived RONS (H_2O_2, HNO_2 and HNO_3) were determined in PBS after plasma treatment, in the same way as explained in Chapter 3. Experiments were again performed on three separate days, with three technical replicates each.

2.2.2 Cell experiments

The human cancer cell line A375 (melanoma, ATCC®) was used to determine the effect of the treatment on the cell viability. Cancer cells were cultured in Dulbecco's Modified Eagle Medium (DMEM, 10938025, Gibco) supplemented with 10 % fetal bovine serum (FBS, Gibco), 100 U/mL penicillin, 100 µg/mL streptomycin (15140122, Gibco) and 4 mM L-glutamine. The kINPen® MED was used to treat 2D monolayers of 96 000 A375 cells per well in a 24-flat well plate (10062-896, Avantor) with or without gas shield. The plasma setup was controlled by an automated stage using the program WinPC-NC. Hoechst (200nM, 62249, Life Technologies) and Cytotox Green (60 nM, 4633, Essen Bioscience) were added to measure both confluence and cell death with fluorescence imaging at 4h, 24h, and 72h. Experiments were once again performed on three separate days, with three technical replicates each.

3. Results and discussion

3.1 Comparison to literature

In literature, the effectiveness of using a gas shield was shown by Reuter *et al.* [108], both experimentally and with a simple CFD model. The most notable difference between their investigation and our study is the geometry of the shielding gas device. While in [108] the device was made in-house, we opted (with the interest of reproducibility and a clinical setting in mind) for a device specifically made for the kINPen by Neoplas [167].

Interestingly, when we adapt our model to the geometry shown in [108], as presented in Figure 4-1a, our computational results do show efficient shielding for the free jet: any influence from the ambient atmosphere is pushed back by the gas shield until after the plasma plume has ended as illustrated in Figure 4-1b. Moreover, the different shield geometry also significantly changes the conditions in the plasma effluent above a well plate, as shown in Figure 4-1c: the rise in H_2O only happens after the end of the plasma plume (i.e. providing better shielding), and the amount of N_2 that mixes with the effluent is reduced.

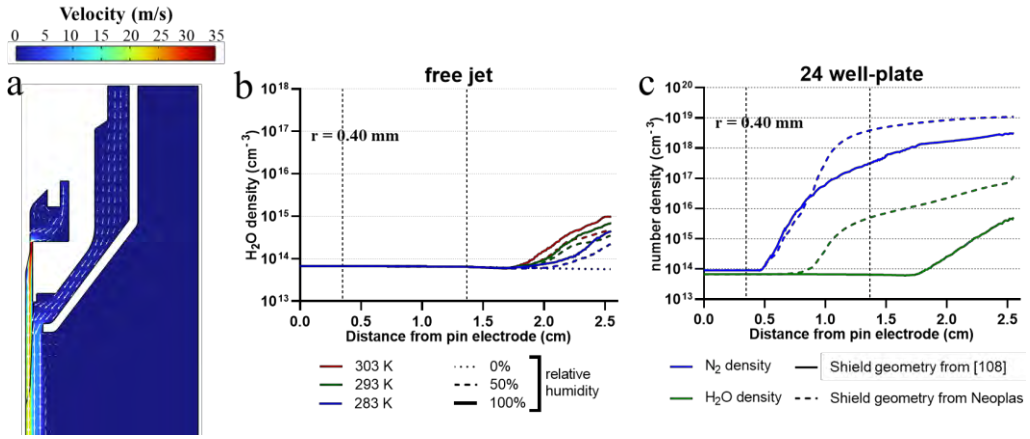

Figure 4-1. Calculated flow field (a) and H_2O number density in the jet effluent, for a free jet (b), for the shielding gas geometry used in [108]. Number density of N_2 and H_2O in the effluent above a 24-well plate is also shown for both the shield from [108] and the shield from Neoplas (used throughout Chapter 3), for 293 K and 50% relative humidity (c). It is important to note that the shape of the liquid water surface was kept unchanged for the different shield geometry. This will not be entirely correct: the different geometry changes the flow field, and e.g. slows stagnation of the effluent velocity, which will in turn induce a different liquid surface shape. However, we believe this effect is of minor importance for the message of this figure.

3.1.1 Experimentally testing shielding efficiency

To confirm that the Neoplas shielding gas device used in our model up until now does not provide efficient shielding, we experimentally tested different shielding gas compositions for treatment of a liquid sample, followed by measurement of long-lived RONS in the treated liquid. It has been shown in literature that when the plasma jet effluent is efficiently shielded from the environment, different shielding gas compositions can significantly change the RONS composition of a treated liquid. For example, by using a shielding gas devoid of N_2, the production of nitrogen-containing species can effectively be prevented [156, 168].

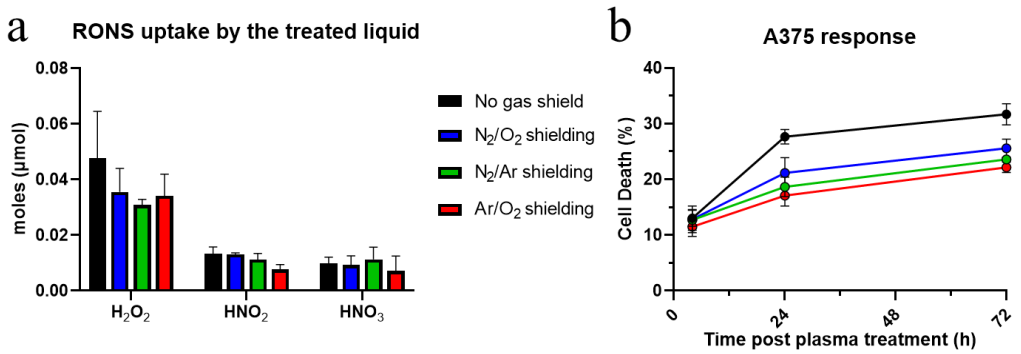

Figure 4-2. (a) Experimentally measured RONS uptake in treated liquid after 60 seconds of treatment time, for different shielding gas compositions. (b) Response of A375 cancer cells to the treatment, using the same treatment conditions as in (a). Data is shown as the mean value and standard deviation of the replicates. Cell death was measured 4, 24 and 72 h after the treatment.

The results in Figure 4-2a show that HNO_2 and HNO_3 are still produced in large amounts when an Ar/O_2 shielding gas is used. Moreover, the production of the measured RONS is similar regardless of the shielding gas composition. This shows that despite the shielding, species from the ambient, like N_2, still make it into the jet effluent in significant amounts with this gas shield. This is also reflected by the measured response of melanoma cell line A375 to the plasma treatment, shown in Figure 4-2b: there is little difference between the results for the different shielding gas compositions. The difference compared to the treatment without shielding gas mirrors the measured H_2O_2 uptake, shown in Figure 4-2a. Note that the RONS measurements and the cell experiments were performed in different liquids. For the species measurements, PBS was used to prevent consumption of the long-lived RONS before measurement. For the cell experiments, the cells were treated in cell medium, which contains organic biomolecules that can act as

scavengers for plasma-produced RONS. The response seen in Figure 4-2b is thus not only the result of the primary species produced by the plasma, but also of secondary species such as oxidised biomolecules, which also affect the cancer cells [169].

3.1.2 Underlying reason for the different shielding efficiencies

The question remains what the underlying reason is for the large difference in shielding efficacy in Figure 4-1. One of the most notable differences between the two shield geometries is that the radial distance between the shielding nozzle and the jet nozzle is larger for the shield geometry used in Chapter 3. At first glance, one would expect that increasing the radial position of the shielding nozzle could be beneficial, as it keeps the ambient further away from the plasma jet. However, as was shown previously in Figure 3-2, a vortex forms in the region between both nozzles. It was found in the model that this vortex effectively "pulls in" species towards the jet effluent. In fact, the vortex acts in a similar way to the recirculation zone generated by bluff-body stabilisation, used in combustion. In this field, the formation of a recirculation zone between the two nozzles is used to enhance fuel-air mixing and stabilize the flame [170, 171]. A closer look at the behaviour in this vortex is provided in Appendix C.

For the free jet, the species that are pulled in are those from the ambient atmosphere, explaining why for the free jet, shown previously in Figure 3-10, there is only a small difference between the case with and without gas shield. When the jet is positioned above a well plate, the species that are pulled in by the vortex are mainly those in the backflow coming from the well (explaining why the evaporated water so significantly affects the H_2O density in the jet effluent, while for the shield geometry in Figure 4-1 this is far less the case). However, species from the ambient also still make it into the effluent, as becomes clear from Figure 4-2 and was previously also visible in Figure 3-5. Finally, for a 96-well plate, we could see previously in Figure 3-8 that backflow coming from the well is directed outwards, unlike for the other well types where the induced backflow is directed upwards. This means that the gas next to the vortex between the jet nozzle and the shield nozzle is mainly the ambient atmosphere, and thus, based on the current train of thought, one would expect the treatment (with a gas shield) of a 96-well to be more susceptible to variation in the ambient conditions compared to that of 12-, 24- and 48-wells. Indeed, as shown in Figure 4-3, the ambient humidity plays a far larger role in this case than for the other well types, more akin to the situation without a treated well.

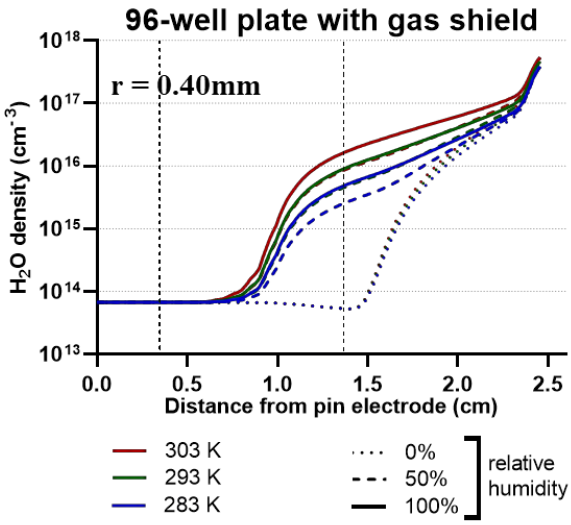

Figure 4-3. H_2O number density in the jet effluent as calculated for the 96-well plate with shielding gas.

3.2 Systematic study of the effect of the gas shield geometry

To investigate the effect of different gas shield geometries in more detail, we present here a systematic study of the effect of the gas shield geometry. Indeed, since its introduction by Reuter *et al.* [108], different gas shield geometries have been used in both modelling and experimental works [117, 156, 166]. To the best of our knowledge, however, the influence of a change in shielding gas geometry on its efficacy has rarely been reported. In the following, we will use our computational model to investigate the effect of the gas shield geometry on the conditions in the plasma effluent, and on its ability to shield the plasma effluent from the ambient. To investigate this in a general way, we simplified the model geometry, as shown in Figure 4-4a. Like in the previous sections, we will discuss the H_2O density and the N_2 density in the effluent (while O_2 acts in the same way as N_2).

3.2.1 Effect of the shield nozzle position and width

Four main parameters can be adjusted in the shielding gas device geometry, i.e. (i) the axial and (ii) radial position of the shielding nozzle compared to the plasma jet nozzle, (iii) the width of the shielding nozzle, and (iv) the flow direction of the shielding gas relative to the plasma effluent. This section will present the effect of the first three parameters, while the flow direction will be discussed in Section 3.2.2 below.

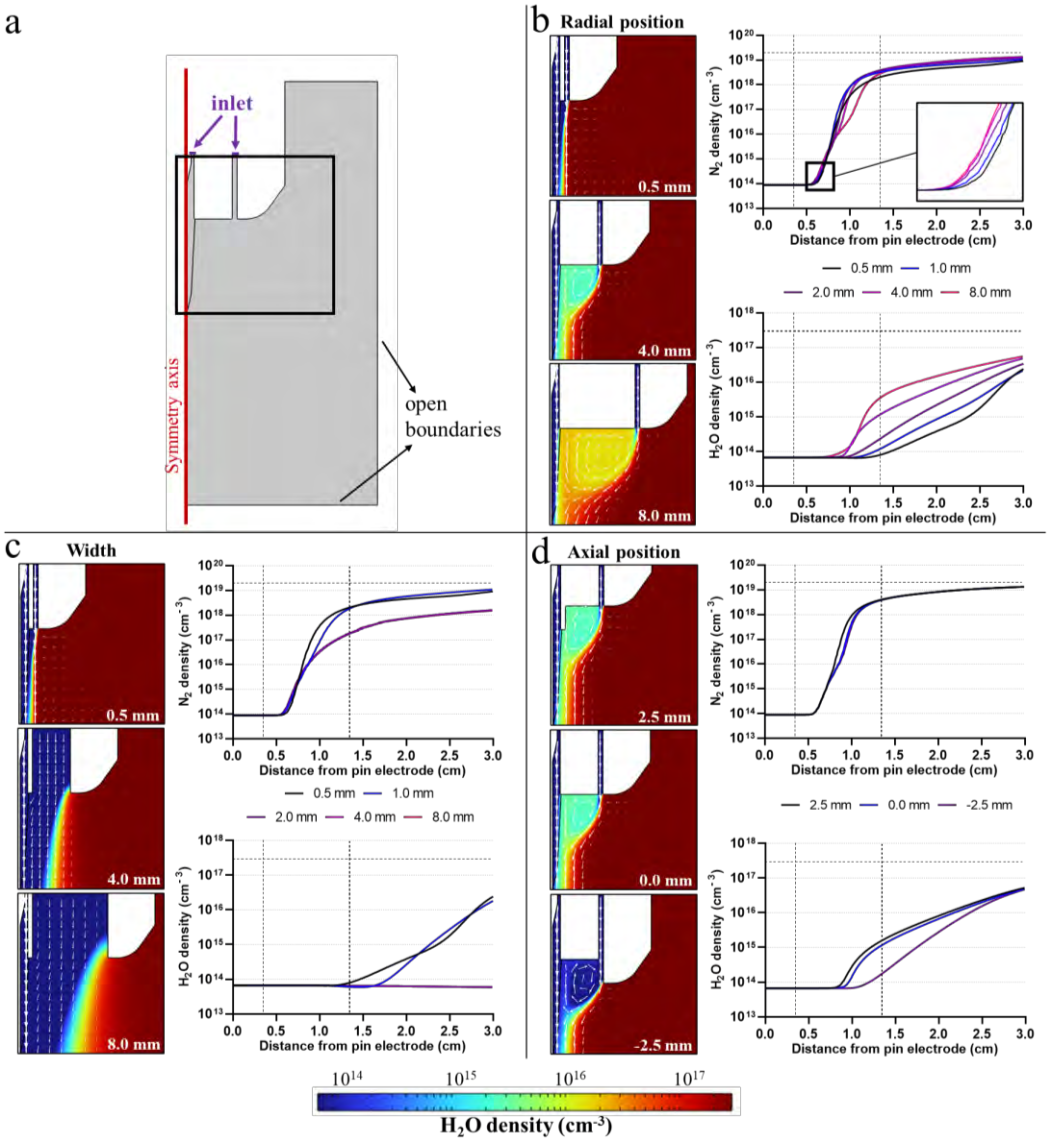

Figure 4-4. Effect of the gas shield geometry on the N_2 density and H_2O density in the plasma effluent. (a) shows the basic geometry of the jet nozzle and gas shield nozzle. The investigated parameters are (b) the radial position, (c) width and (d) axial position of the gas shield nozzle relative to the plasma jet nozzle. The 2D plots show the ambient H_2O density, with white arrows representing the flow field. In (a) the black box indicates which part of the geometry is shown in these 2D plots. The 1D plots depict the N_2 and H_2O number density in the plasma effluent, at a radial position of 0.40 mm, as a function of distance from the pin electrode for the different simulated gas shield geometries. In (c), the curves for 2.0, 4.0 and 8.0 mm overlap. Note that the colour scale is logarithmic to clearly visualize the differences.

Figure 4-4b illustrates the effect of the radial position of the shielding gas nozzle compared to the outer diameter of the plasma jet nozzle. A large radial distance between both nozzles causes formation of a vortex, like discussed previously in Section 3.1.2, that accumulates species from the ambient atmosphere. As the radial distance decreases, this vortex becomes smaller, and the density of ambient species in it decreases. At very small radial distance between the nozzles, the vortex disappears completely. This trend is clearly visible for the H_2O density, on which the radial distance (and by extension, the size of the formed vortex) has a very large influence. For larger radial distances, the H_2O density in the plasma effluent rises much faster. Additionally, larger radial distances also decrease the axial position at which the rise in density starts. For the largest simulated radial distance (8 mm), the H_2O density in the plasma effluent (at a radial position of 0.4 mm) starts rising at 7 mm from the pin electrode. When the radial distance is small enough to prevent formation of the vortex, this rise in H_2O density only occurs near the very end of the plasma plume. This means that smaller radial distances between the jet and shielding nozzle, or in other words, a more confined shielding curtain around the plasma effluent, provides a better shielding effect. The same general trend is present for the N_2 density. A larger radial distance between the jet and shielding nozzle decreases the distance from the pin electrode at which the N_2 density in the plasma effluent starts to rise, and it increases the amount of N_2 in the effluent. Only at the end of the visible afterglow, around 10 mm from the pin electrode, the behaviour is different, and no clear trend is visible.

Figure 4-4c shows the influence of the width of the shielding gas nozzle. Increasing the gas curtain width causes a strong drop in the amount of H_2O that is able to mix with the plasma effluent, as the ambient is kept further away. This trend is opposite to that for an increasing radial distance between the plasma jet nozzle and the shielding gas nozzle. Indeed, increasing the radial position of the shield gas nozzle also keeps the ambient further away from the plasma jet, but this actually increases the amount of ambient H_2O that mixes with the jet effluent, due to the vortex creation. This further emphasizes the importance of the vortex that can form between the jet effluent and the shield effluent (note that in Figure 4-4b and Figure 4-4c the outer diameter of the gas shield is the same for each simulated condition, respectively). For the N_2 density, two behaviours can be seen. For small shield nozzle widths (0.5 -1 mm) the N_2 mixes with the plasma effluent in higher amounts compared to large nozzle widths (2 – 8 mm). This can be attributed to the fact that, for a large nozzle width, the flow is far less turbulent, causing much less turbulent mixing between the N_2 from the shielding gas and the plasma effluent. These

two behaviours are in fact also visible for the H_2O density, indicating that turbulent mixing also plays a role in the mixing of the plasma effluent with the ambient atmosphere.

Finally, Figure 4-4d depicts the influence of the axial position of the shielding gas nozzle. The N_2 density in the plasma effluent is mostly unaffected by this change in geometry. For the H_2O density, increasing the axial position (i.e., if the shield nozzle position is higher than the jet nozzle position in the geometry of Figure 4-4a) has only a small effect. Lowering the axial position of the shield nozzle however significantly reduces how quickly the ambient gas, as seen by the H_2O density, mixes with the plasma effluent. This is to be expected, because it simply takes longer before the ambient can start diffusing towards the jet effluent. Though the results in Figure 4-4d are only shown for the case where a vortex between the jet nozzle and shield nozzle forms, the trends are the same for the case where no vortex can form.

It should be kept in mind that these simulations were performed for the free jet. When treating a well plate, the backflow from the well can in some cases push back the shielding gas, which may cause unintended effects, as discussed in Chapter 3. To emphasize this, Figure 4-5a shows the effect of the radial position of the shielding gas nozzle, like also depicted in Figure 4-4b, but for the treatment of a 24-well plate (with a 2 cm treatment gap). For a radial distance of 0.5 and 4.0 mm, the shielding gas flow is unaffected, although in these cases most of the H_2O that mixes with the plasma effluent (and accumulates in the vortex, when formed) is evaporated water as opposed to H_2O from the ambient air, as shown in Figure 4-5b. For a radial distance of 8.0 mm, however, the radial position of the shielding gas nozzle becomes similar to that of the well edge, and no vortex forms. Instead, the shielding gas blows into the wells surrounding the treated well. Additionally, although Figure 4-4c indicates that increasing the shielding nozzle width gives a better shieling effect, a wider shielding curtain makes it easier for the backflow from the well to push back the shielding gas.

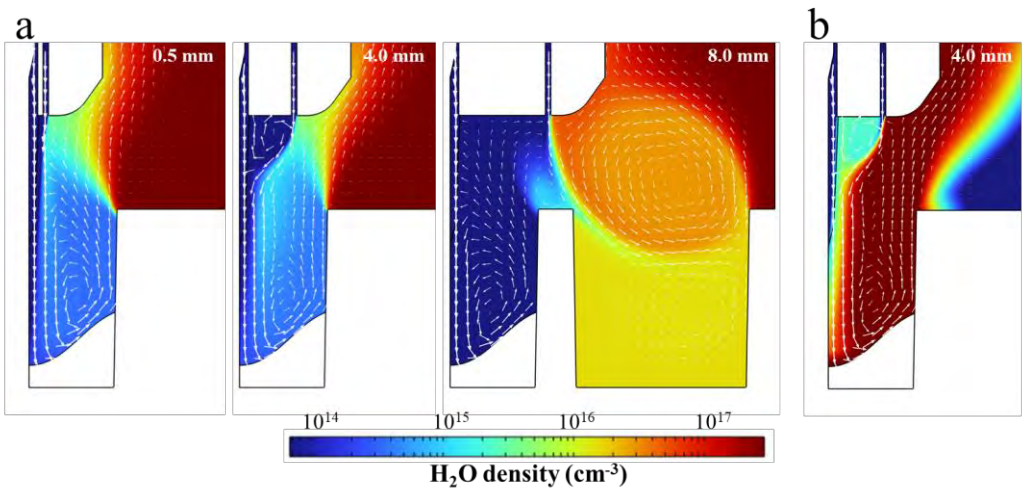

Figure 4-5. Effect of the well-induced backflow on a gas shield, for different radial distances of the shielding gas nozzle. (a) Ambient H_2O density in the system. For the case with a radial distance of 8.0 mm, the neighbouring well is shown, for clarity. (b) Evaporated H_2O density in the system, for the gas shield with a radial distance of 4.0 mm. Arrows represent the flow field. The liquid phase in the wells is depicted in white.

3.2.2 Effect of the flow direction

Apart from the position of the shielding gas nozzle relative to the plasma jet nozzle, and its width, the flow direction relative to the plasma effluent can be adapted. In literature, different gas shields are depicted that direct the shielding curtain parallel to the plasma effluent [117], or direct it towards the plasma effluent diagonally [166, 172] or perpendicularly [108]. Figure 4-6 shows the influence of the flow direction of the shielding gas, for a small radial distance between the jet nozzle and the shielding gas nozzle.

Both the diagonal and perpendicular flow direction induce less mixing of the jet effluent with H_2O from the ambient, compared to the parallel flow. The reason is that for these two cases there is much less turbulent mixing, similar to the effect of the shielding nozzle width discussed in the previous section, which causes the ambient air to penetrate into the jet effluent far slower. This behaviour was also noted by Gazzah *et al*. [173], who reported reduced mixing in a jet with co-flow by directing the co-flow towards the jet effluent. This also explains the N_2 profiles plotted in Figure 4-6: less N_2 mixes with the jet effluent for the diagonal and perpendicular compared to the parallel flow direction. Note that here, the same two behaviours can be seen as in Figure 4-4c.

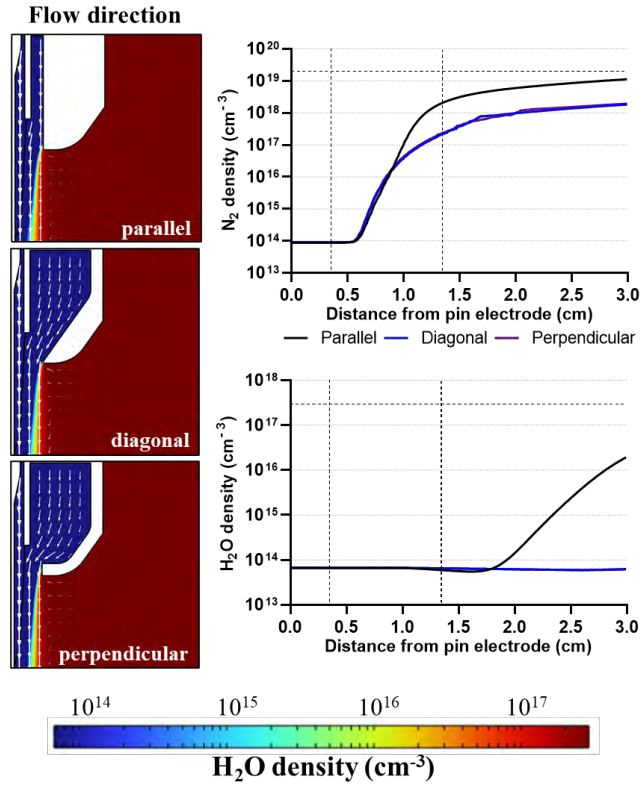

Figure 4-6. Effect of the flow direction of the gas shield, relative to the flow from the plasma jet, on the N_2 density and H_2O density in the plasma effluent. The 2D plots show the ambient H_2O density, with white arrows representing the flow field. The 1D plots show the N_2 and H_2O number density in the plasma effluent as a function of distance from the pin electrode for the different simulated flow direction of the gas shield.

4. Conclusion

In this chapter, we were able to find an explanation for the unexpected low efficacy of the gas shield, as used in the investigation of Chapter 3, in shielding the jet effluent from the ambient atmosphere. When instead implementing the gas shield geometry as initially reported by Reuter *et al*. [108] into our model, we showed that changing the design of the shielding gas device can have significant consequences on both the conditions in the jet effluent and on the ability of the gas shield to effectively shield the jet from the surrounding atmosphere.

Consequently, we systematically investigated the effect of different gas shield geometries, i.e., the radial and axial position of the shielding gas nozzle, its width, and the flow direction relative to the plasma jet flow. Overall, the largest effect was seen for the radial position of the shielding gas nozzle. When this increases, a recirculation zone can arise between the shielding curtain and the plasma effluent, which pulls in species from the ambient, severely changing the conditions in the plasma effluent. In this way, we further showed that the gas shield design can have a substantial effect on the shielding efficiency.

Taken together, in the past two chapters we have applied our computational CFD model, as presented in Chapter 2, to gain insight into the effect of various aspects of the setup geometry. We showed that when treating a well plate with a plasma jet, the conditions in the jet effluent can be significantly altered by the chosen setup geometry. These choices largely determine the RONS produced by the plasma, through the densities of N_2, O_2 and H_2O that mix with the noble gas effluent from the jet. As a result, these effects will thus also determine the treatment outcome. These insights are important to keep in mind in experimental work. Indeed, various setups and conditions are used throughout literature, and this lack of uniformity can make experimental results difficult to compare. Such a lack of uniformity is, however, not exclusive to experiments, and can also arise in computational work. This will be the subject of the following chapter.

Chapter 5

Critical comparison of interfacial boundary conditions in modelling plasma-liquid interaction

The content of this chapter is based on:

Critical comparison of interfacial boundary conditions in modelling plasma–liquid interaction
Pepijn Heirman and Annemie Bogaerts
J. Phys. D: Appl. Phys., 58, 085206 (2024)
https://doi.org/10.1088/1361-6463/ad9c8f

Several computational models have been developed over the past decade with the goal of investigating the various processes that occur during plasma-liquid interaction. However, many different boundary conditions to describe transfer of chemical species over the gas-liquid interface have been reported and used in these investigations. In this chapter, we employ our computational model to test these different boundary conditions, and compare the results to experimental data for H_2O_2, O_3, ·NO and HNO_2, to assess how well they can describe the dissolution of different species. We will see that the validity of the different formulas depends on the solubility of the investigated chemical species; they appear valid for species with high solubility (H_2O_2), but not for species with low (O_3 and ·NO) or intermediate (HNO_2) solubility. Finally, we propose an approach to reach better agreement, based on film theory in combination with the mass accommodation coefficient.

1. Introduction

Computational simulations can form a valuable tool to elucidate the various processes that occur during plasma-liquid interaction. Over the past decade, several computational models have been developed, with varying degrees of complexity, to investigate the plasma treatment of a liquid and, specifically, the reactive chemical species that end up in the liquid upon treatment. Modelling studies have been reported for plasma jets above liquid water, such as discussed at length in Chapter 1, and for DBDs in contact with liquid water. Integral to a computational model that simulates plasma-liquid interaction is the description of the dissolution of reactive species from the gas phase into the liquid phase. Notably, however, various computational works in literature employ different methods of describing this species transfer across the plasma-liquid interface.

Physically, the solubility of gas in a liquid is described by Henry's law [174]:

$$\frac{c_l}{p} = H^{cp} \tag{E.5-1}$$

Where H^{cp} is the Henry's law solubility constant of the chemical species, c_l is the concentration of the species in the liquid phase, and p is its partial pressure in the gas above the liquid. Henry's law is, however, an equilibrium law, i.e. it describes the concentration of species in the gas and liquid phase in steady state and does not give any information on the rate of the dissolution process, i.e. how fast this equilibrium is reached. Moreover, before steady state is reached, different phenomena can complicate matters further, such as the depletion of a soluble gaseous species near the liquid interface. Different published models simulating plasma-liquid interaction have used a variety of boundary conditions at the plasma-liquid interface, to describe species transfer between both phases in a way that adheres, if steady state is reached, to Henry's law. Often, however, comparison of the liquid concentrations to experimental data, which would support the use of these boundary conditions, is lacking. In the few cases where simulation results on the predicted dissolution of reactive species have been benchmarked against experiments, this was done only for H_2O_2, a highly soluble species. Of course, experiments that can test the validity of the boundary condition describing solvation, independently of other factors such as chemical reactions, are not straightforward. For a few cases, though, experimental data has been published [160, 175].

In this chapter, we employ our computational fluid model as explained in Chapter 2 to investigate and compare the various expressions for the description of species transfer between gas and liquid, as used in published computational works in the field of plasma-liquid interaction. The results are compared to published experimental data, in order to assess how well these expressions are able to replicate experimental results, a crucial prerequisite for the use of a computational model to both explain and predict experimental outcomes. To the best of our knowledge, no critical comparison of these expressions, benchmarked with experimental data, is available in literature. Our data indicates that the validity of the different formulas depends on the solubility of the investigated chemical species, and that none of the tested expressions is able to replicate experimental data for all species. Finally, we expand our view to fields outside plasma-liquid interaction, and propose an approach to reach better agreement.

2. Methods

2.1 Computational model

Several different model geometries will be used throughout this chapter, based on experimental setups from literature. The modelling approach for each is as presented in Chapter 2, while the model is adapted in each case to the conditions reported for each setup as described in Section 2.2 of this chapter.

Each of the various expressions tested throughout this work to describe dissolution of RONS into the treated liquid at the gas-liquid interface, which are discussed in detail in Section 3.2, depends on Henry's constant of the simulated species. We employ the temperature-dependent Henry's constant, calculated as follows [174]:

$$H^{cp} = H^{cp,0} \cdot exp\left(\frac{-\Delta_{sol}H}{R}\left(\frac{1}{T} - \frac{1}{T^0}\right)\right) \quad \text{(E.5-2)}$$

Where $\mathrm{H}^{\mathrm{cp,0}}$ is the Henry's constant at the standard temperature $\mathrm{T}^0 = 298.15\ \mathrm{K}$, $\Delta_{\mathrm{sol}}\mathrm{H}$ is the enthalpy of dissolution (J/mol), and R is the ideal gas constant (J/mol·K). The parameters in equation (E.5-2) are taken from [174], and are shown in Table 5-1.

Table 5-1. Parameters used to calculate the temperature-dependent Henry's constants of RONS used in this work.

Species	$H^{cp,0}$ (mol/m³·Pa)	$\frac{-\Delta_{sol}H}{R}$ (K)
H_2O_2	8.6×10^{2}	7300
O_3	1.0×10^{-4}	2800
·NO	1.9×10^{-5}	1600
HNO_2	4.7×10^{-1}	4900

Note that the temperature-dependence of the Henry's constant does not strictly follow the van 't Hoff equation with constant $\Delta_{sol}H$ as depicted above. However, for the simulated conditions, the above expression is sufficient [153].

2.2 Model geometries

Figure 5-1 shows the different model geometries used throughout our investigation, each based on an experimental setup reported in literature. To mimic the experimental data as close as possible, each simulation is performed for the same conditions as those described in the respective references, including the working gas composition and inlet flow rate.

The geometry shown in Figure 5-1a is based on the setup used by Winter *et al.* [160], where a petri dish containing 5 mL liquid was treated with the kINPen plasma jet (without igniting the plasma) with a gap between the jet nozzle and the liquid surface (before treatment) of 9 mm. Through the jet inlet, 3 SLM of humid argon containing 5 ppm H_2O_2 enters the gas phase domain. The shielding gas inlet has a flow rate of 5 SLM dry air. It is stated in [160] that the kINPen was continuously moved over the liquid during treatment, mixing the liquid. Hence, the liquid phase is assumed to be well mixed, as in [127].

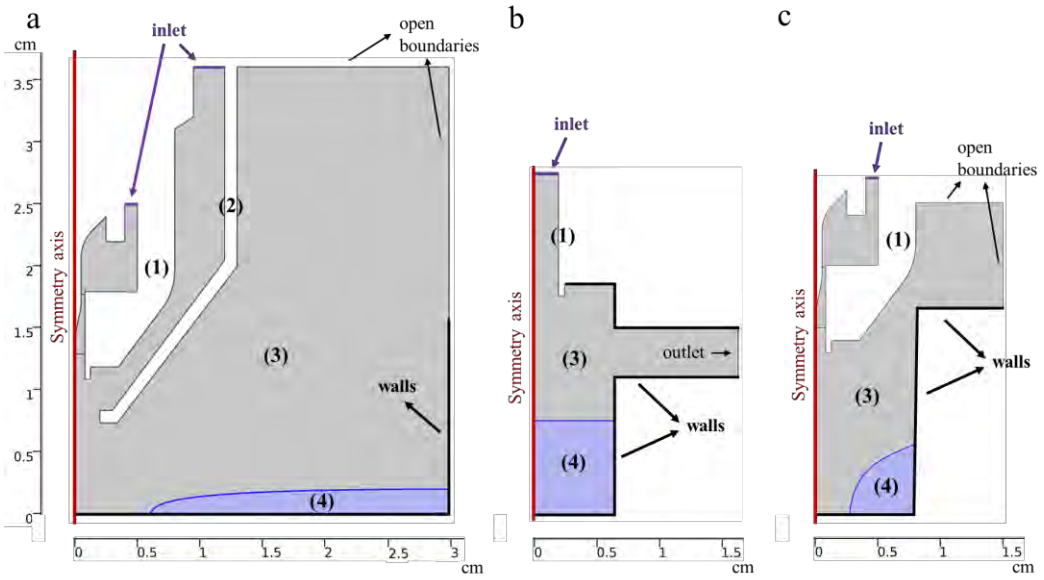

Figure 5-1. Model geometries used throughout this chapter, based on the experimental setups used in [160] (a), [175, 176] (b), and [177] (c). The geometry components are (1) the jet, (2) the shielding gas device (when present), (3) the gas phase and (4) the liquid phase. Boundary conditions at the model edges are indicated, including the symmetry axis around which the 2D-axisymmetric model is revolved. Note that in (a) and (c) the liquid is pushed away by the gas to such a degree that the gas reaches the bottom of the petri dish or well.

Figure 5-1b represents the geometry based on the setup of Hassan *et al.* [175, 176]. Either 1000 µL (as shown here) or 500 µL is treated with either 2 SLM of 50 % humid air containing 110 ppm H_2O_2, 1.6 SLM of dry air containing 450 ppm O_3, or 1 SLM of humid air containing 100 ppm HNO_2. The gas-liquid interface is flat, based on the observations described in [175], and has the same surface area for both liquid volumes (i.e., only the liquid depth is changed). Unlike for the other geometries, laminar flow is simulated in the gas phase because of the much lower flow velocity (Re ≈ 700). Note that, for this geometry, the outlet tube in our model is an approximation, as this element of the experimental setup is not axisymmetric.

Finally, the geometry in Figure 5-1c represents the experimental setup used by Jablonowski *et al.* [177], where a 24-well plate containing 750 µL of liquid was treated with the kINPen. The treatment gap is 9 mm, and the feed gas is 3 SLM of dry argon containing 40 ppm ·NO.

3. Results and discussion

3.1 Directly using Henry's law

The most straightforward method of implementing species transfer between a gas and liquid phase in a computational model is by directly coupling the concentrations in both phases at the gas-liquid interface via Henry's law:

$$\frac{c_l}{c_g} = H^{cc} \qquad \text{with } H^{cc} = H^{cp} \cdot RT \tag{E.5-3}$$

Where $\mathrm{H^{cc}}$ is the dimensionless Henry's constant, R the ideal gas constant (J/mol·K), and T the temperature (K). This method has been used in several published models, including by our group [124-126, 129, 178, 179]. For mass conservation, it is necessary to additionally specify that the flux of species entering the liquid must also exit the gas phase at the interface, thus recalculating both c_l and c_g. To investigate how well this boundary condition can describe the dissolution of chemical species into a liquid, we need to compare computational results to experiments where liquid water was treated with a gas jet that contains a known amount of RONS, whose concentration is afterwards measured in the treated liquid.

Such an experiment was performed by Winter *et al.* [160], where they measured how much H_2O_2 was dissolved into an aqueous medium after treatment with argon containing a known amount of gaseous H_2O_2, using the kINPen plasma jet (without igniting the plasma), as also described above (see Figure 5-1a). We thus adapted our model to the setup used in [160]. Figure 5-2a shows the resulting H_2O_2 density profile in both gas and liquid phase calculated by the model, while Figure 5-2b illustrates how well using Henry's law directly as the boundary condition at the interface can replicate the measured dissolution of H_2O_2 into the treated liquid. Clearly, there is very good agreement between model and experiment. Notably, almost all H_2O_2 present in the feed gas dissolves into the liquid. To emphasize this, Figure 5-2b additionally shows the maximum amount of H_2O_2 that would physically be able to dissolve (i.e. if 100% of the gaseous H_2O_2 that entered the system was dissolved in the liquid). The reason for this is two-fold: (i) H_2O_2 has an extremely high solubility ($\mathrm{H^{cc}} = 1.84 \times 10^6$, at 300K), and (ii) in this setup, the treated liquid has a large surface area through which the species can dissolve.

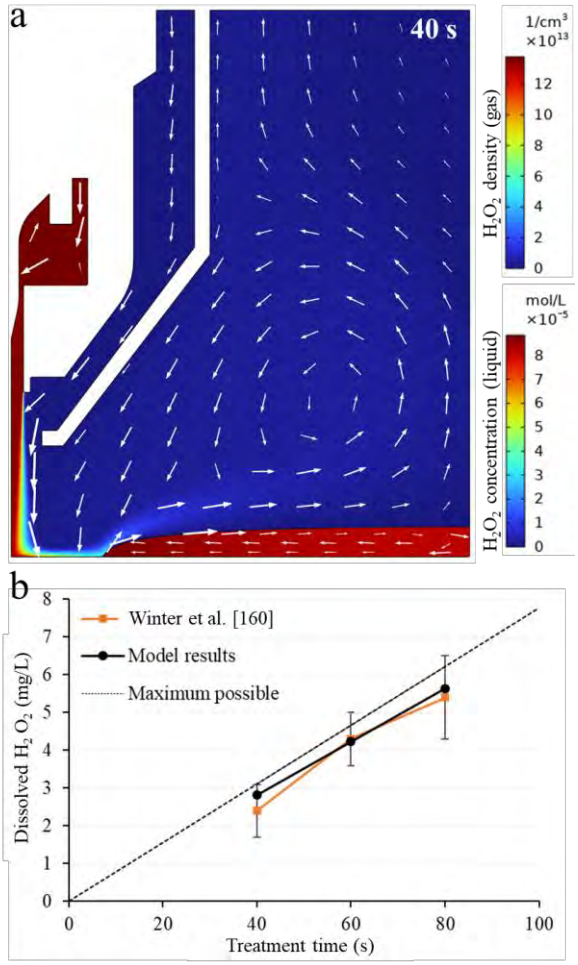

Figure 5-2. Model results for the setup geometry described in [160], where 5 mL of liquid is treated with 3 SLM of argon containing 5 ppm H_2O_2. (a) Calculated H_2O_2 density profile in gas and liquid phase, after 40 s of simulated treatment. Arrows represent the calculated flow field in the system. (b) Total dissolved H_2O_2 concentration over time, compared to the reported experimental data, and the maximum possible concentration (see text).

Similar experiments were performed by Hassan *et al.* [175], though with a much higher gaseous H_2O_2 concentration, and a smaller liquid volume. In this case, as can be calculated from their reported data, a smaller fraction of the gaseous H_2O_2 dissolved into the treated liquid. Figure 5-3 shows our simulation results when we adapt our model to their setup. Figure 5-3a depicts the calculated H_2O_2 density profile in gas and liquid phase. Just above the interface, the gaseous H_2O_2 is depleted (see inset in the figure) because of its high solubility, a phenomenon that has also been reported elsewhere

[115, 125]. Again, as seen in Figure 5-3b, our calculated amount of dissolved H_2O_2 agrees very well with the reported experimental values.

In the same work, Hassan *et al.* [175] also investigated the dissolution of O_3 into the treated liquid. In contrast to H_2O_2, O_3 has a low solubility ($H^{cc} = 0.24$, at 300K), inhibiting the depletion of the gas phase directly above the liquid, as visible in Figure 5-3c. Figure 5-3d shows that, unlike for H_2O_2, our model now vastly overestimates how much O_3 dissolves into the liquid. In addition, our model predicts a significant change in dissolved amount depending on the liquid volume, while the experiments show no difference as long as the surface area stays the same (note that the y-axis depicts the number of moles, not the concentration like in Figure 5-2b).

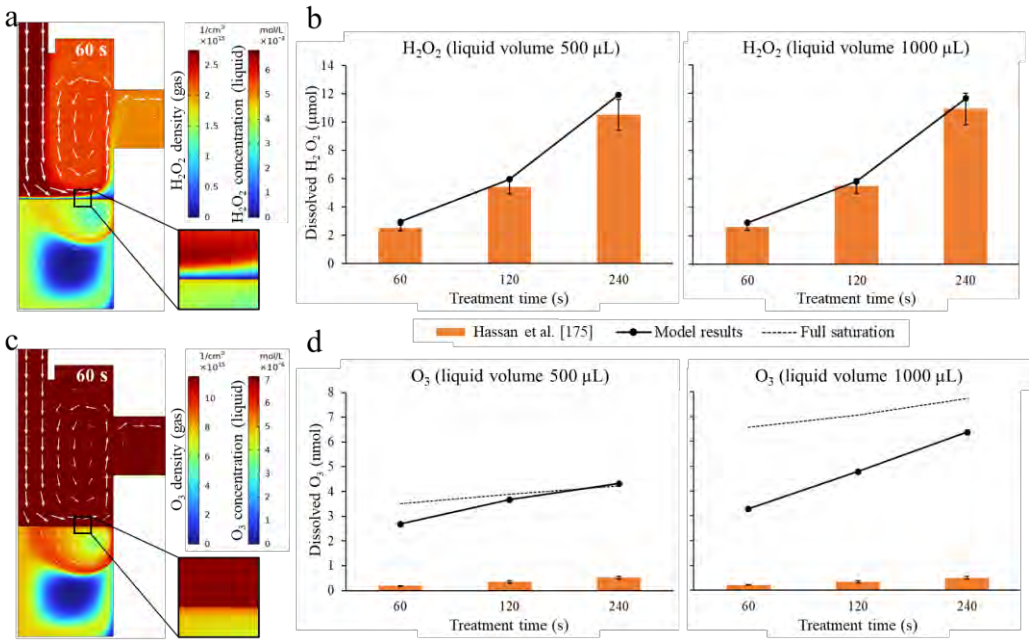

Figure 5-3: Model results for the setup geometry described in [175], where 500 µL and 1000 µL of liquid is treated with air containing either 110 ppm H_2O_2 (a, b) or 450 ppm O_3 (c, d). (a) Calculated H_2O_2 and (c) O_3 density profile in gas and liquid phase, after 60 s of simulated treatment. Arrows represent the calculated flow fields. (b, d) Total dissolved amount of H_2O_2 and O_3 over time, compared to the reported experimental data. For O_3, the total dissolved amount if the liquid were fully saturated when in contact with 450 ppm gaseous O_3 is also shown (dashed line). The saturated amount rises with time because the gas flow causes the liquid to cool: as we apply the temperature-dependent Henry's constants, the solubility thus increases with decreasing temperature.

From the above, it is clear that using Henry's law directly as the boundary condition governing species dissolution in the model is sufficient for highly soluble species, such as H_2O_2, but severely overestimates the dissolution of species with low solubility, such as O_3. The issue lies in the fact that by applying Henry's law directly, the model forces equilibrium at the interface in each time step, without taking into account how long it would take in reality to reach equilibrium. This causes the interface region to be saturated almost immediately, while the flow field continuously renews the liquid at the interface. For species with low solubility, this in turn causes the entire liquid phase to reach saturation soon, more so for smaller liquid volumes, as dissolved species are efficiently transported toward the bulk through convection. This is also visible in Figure 5-3d, when comparing the dissolved amount of O_3 over time calculated by our model with the dissolved amount if the liquid were saturated with O_3.

3.2 Other formulas used in literature

Clearly, a model that directly applies Henry's law does not produce correct results for the dissolution of gaseous (plasma-produced) species into liquid water. Although several published modelling studies have used Henry's law directly at the plasma-liquid interface, including our group [124-126, 129, 178, 179], many multi-dimensional models for plasma treatment of water have been reported over the past decade that take a different approach to describe the dissolution of neutral species. Numerous different formulas have been described in these works, but most can be grouped into either kinetic boundary conditions [180-182], diffusive boundary conditions [112-115, 118, 119, 183, 184], or film theory [127]. In the following, a recently reported use of each approach is briefly described.

The kinetic approach, as explained by Hassan *et al.* [175], treats the transfer of species between the gas and liquid phase with a flux Γ, based on the mean molecular velocity $\bar{v}$ of gas phase species above the interface:

$$\Gamma_{g\leftrightarrow l} = \frac{1}{4}\bar{v}\left(c_g - \frac{c_l}{H^{cc}}\right) \tag{E.5-4}$$

The above expression arises from the assumption that all gas molecules that strike the interface via random motion are transported to the liquid, while transport back to the gas phase happens continuously with a rate that depends on the species' surface concentration.

The diffusive approach essentially describes diffusion of chemical species through the liquid interface, but with a weighted diffusion coefficient (e.g. for the plasma/gas phase: $D = D_g \left(\frac{H^{cc} \cdot c_g - c_l}{H^{cc} \cdot c_g}\right)$) that depends on how close the system is to the equilibrium prescribed by Henry's law. In this way, Kruszelnicki *et al.* [115] applied two fluxes to the plasma-liquid interface in their model., i.e. a flux from gas to liquid, and a flux from liquid to gas:

$$\begin{cases} \Gamma_{g \to l} = \frac{D_g}{\Delta x}\left(\frac{H^{cc} \cdot c_g - c_l}{H^{cc} \cdot c_g}\right)(c_g - c_l) & \text{if } c_l < H^{cc} \cdot c_g \\ \Gamma_{l \to g} = \frac{D_l}{\Delta x}\left(\frac{c_l - H^{cc} \cdot c_g}{c_l}\right)(c_l - c_g) & \text{if } c_l > H^{cc} \cdot c_g \end{cases} \quad \text{(E.5-5)}$$

Here, Δx represents the mesh element size at the interface, taken in [115] to be 1 µm.

Finally, film theory describes a laminar "film" at the liquid interface through which the chemical species diffuse into and out of the liquid phase [185]. If a film is assumed only on the liquid phase side of the interface, the flux between the two phases can be described as:

$$\Gamma_{g \leftrightarrow l} = \frac{D_l}{\Delta x}\left(H^{cc} \cdot c_g - c_l\right) \quad \text{(E.5-6)}$$

The above equation was employed in the context of plasma-liquid interaction by Semenov *et al.* [127], who assumed the film thickness, Δx, to be approximately equal to 10 µm. Each of the above boundary conditions prescribes a flux between the two phases that goes to zero as the system approaches Henry's law equilibrium, but the magnitude of the fluxes differs for each formula. In case of equation (E.5-5), extra care must additionally be taken, as the flux also becomes zero for $c_g = c_l$, which is an unphysical equilibrium for all species that do not have a Henry's law constant equal to 1.

To investigate how equations (E.5-4), (E.5-5) and (E.5-6) perform at replicating experimental results compared to directly applying Henry's law, we implemented them into our model. Figure 5-4a shows the results for H_2O_2. Clearly, all curves overlap: regardless of the used boundary condition, the same amount of H_2O_2 is calculated to dissolve, which agrees very well with the experimental results. For O_3, the results are less ideal. As shown in Figure 5-4b, the results are similar for each equation used, though not identical, and comparable to when simply applying Henry's law directly. However, they are clearly far higher than the experimental results. Hence, all boundary conditions

severely overestimate the amount of O_3 that dissolves into the treated liquid. The fact that different boundary conditions describing species dissolution behave similarly was also reported by Liu *et al*. [186], who compared the diffusive approach, kinetic approach and applying Henry's law directly (referred to there as the "thermodynamic" approach) in their 1D model. However, the authors did not compare the results to experiments. Figure 5-4b clearly illustrates that although these approaches indeed produce similar results, they are in fact wrong when compared with experiments.

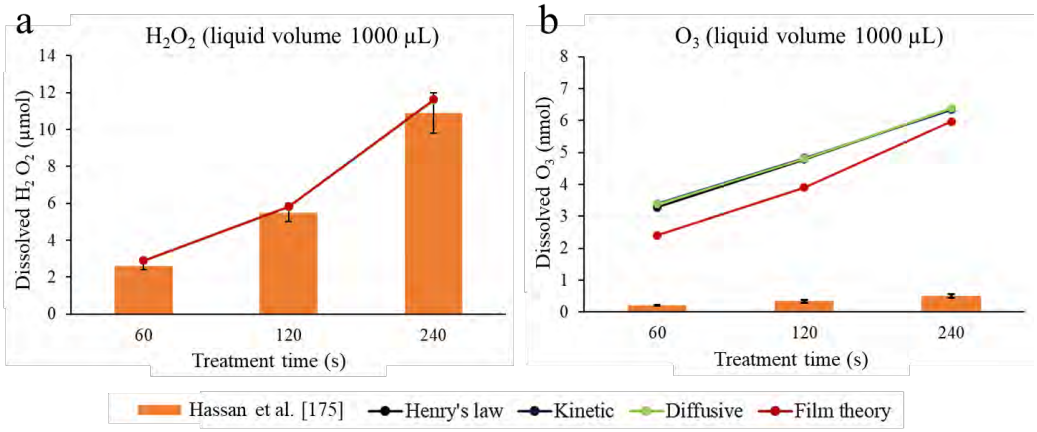

Figure 5-4. Total dissolved amount of H_2O_2 (a) and O_3 (b) over time, as calculated by our model using four different boundary conditions on the gas-liquid interface, compared to the experimental data reported in [175]. In (a), the four curves overlap, while in (b) the green, blue and black curve overlap.

In essence, the different boundary conditions used in plasma-liquid literature overestimate the flux of plasma-produced species into the liquid. For species with high solubility like H_2O_2, this does not cause a problem. Its high solubility causes the gaseous region above the liquid to become depleted, meaning that transport from the "bulk" of the gas to the liquid surface is rate-limiting, not the transport of species into the liquid. For species with low solubility, the transport into the liquid is rate-limiting, so an overestimation of the flux across the interface causes overestimation of the dissolved amount. When directly applying Henry's law, this overestimation is caused by the assumption that equilibrium at the interface is reached instantly. For the kinetic and diffusive approach, transport from gas to liquid is only determined through transport from the bulk gas to the interface (through $\bar{v}$ and D_g, respectively), in practice also causing equilibrium to be reached almost instantly. Only when applying film theory, the

transport is limited by the resistance a species would encounter caused by transport into the liquid phase. More specifically, the flux from gas to liquid is determined by the transport from the interface to the bulk liquid (via D_l), and the concentrations at the interface evolve towards equilibrium over time, not near-instantly. Indeed, Figure 5-4b shows that when using film theory, the results lie (slightly) closer to the experimental values. However, the dissolved amount of O_3 is still severely overestimated.

3.3 Can we reach better agreement?

Describing the dissolution of chemical species into liquid water is, of course, not only relevant for plasma-liquid interaction. Other research fields, such as water purification and atmospheric chemistry, also describe the interaction of gas and liquid. In context of the latter, Kolb et al. [187] reviewed the different transport processes occurring near the gas-liquid interface. One aspect of this, which is not present in the formulas tested so far, is the accommodation of species at the gas-liquid interface. In a non-reactive setting, a gaseous molecule that strikes a liquid surface can either be reflected or be accommodated and transferred through the interface. The ratio of these two outcomes is determined via the bulk mass accommodation coefficient, α_b, described as the probability for a molecule that strikes the liquid surface to actually enter the bulk liquid. As such, α_b determines the maximum possible flux of gaseous species into the liquid [188].

In other words, besides transport from the gas bulk to the interface and transport from the interface to the bulk liquid, transport through the interface itself forms an additional barrier. In principle, not taking α_b into account is the same as assuming it has a value of 1, i.e. 100% of the species that follow the flux prescribed by the boundary condition at the gas-liquid interface will indeed be transported through the interface.

Unfortunately, taking the mass accommodation coefficient into account is not straightforward. Most critical is the fact that values of α_b have been reported for only a handful of species, including only a few RONS, as previously also noted by Kruszelnicki *et al*. [115] when discussing their 0D model. Secondly, for the cases where data is available, reported values span several orders of magnitude for the same species. In theory, molecular dynamics simulations should be able to predict the mass accommodation coefficient of chemical species, but this approach has so far faced issues in reaching agreement with experiments [189, 190]. A compilation of available data can be found in the Chemical Kinetics and Photochemical Data compilation by Burkholder *et al.*, NASA [191]. Both H_2O_2 and O_3 are among the species for which values of the mass

accommodation coefficient are available, allowing us to test the effect of taking this coefficient into account on the model results.

Combining both film theory and the mass accommodation coefficient gives us the following boundary condition for the gas-liquid interface:

$$\Gamma_{g\leftrightarrow l} = \alpha_b \cdot \frac{D_l}{\Delta x}\left(H^{cc} \cdot c_g - \overline{c_l}\right) \tag{E.5-7}$$

Here, $\overline{c_l}$ is the average concentration in the liquid phase. In film theory, $\overline{c_l}$ should in principle be the concentration in the liquid bulk [185], but as our multidimensional model describes a finite liquid phase in which there is constant transport through convection, it is not possible to define a bulk concentration, which can instead be approximated by the average concentration. The maximum film thickness can be estimated as $\Delta x = \sqrt{2 \cdot D_l \cdot r/\bar{v}_{int}}$ where r is the radial dimension of the gas-liquid interface and $\bar{v}_{int}$ the average velocity at the interface, i.e. $r/\bar{v}_{int}$ is the total interaction time between a fluid element in the liquid and the gas phase. The film thickness will vary in the radial direction. We will assume this variation to be quasi-linear, allowing us to use the cylindrical average of Δx for simplicity.

For H_2O_2, using the reported room temperature value of α_b = 0.1 [191], our computational results using equation (E.5-7) still agree well with experimental data, as visible in Figure 5-5a. Because of its high solubility, the mass accommodation coefficient has nearly no effect on the modelling results for H_2O_2: even for a lower value, such as α_b = 0.01, the results stay the same. For O_3, [191] recommends a lower limit of α_b = 0.01. As an upper limit, we can use α_b = 0.1, i.e. the highest reported value of α_b for O_3. Figure 5-5b shows that using equation (E.5-7) as the boundary condition at the gas-liquid interface indeed dramatically improves the agreement between our model and the experimental data. Now, for α_b = 0.01 the dissolved amount of O_3 is slightly underestimated, which can be expected as this value is a lower limit, with the actual value most likely being higher. For α_b = 0.1, the dissolved amount of O_3 is again overestimated, though the agreement is still much better than that shown in Figure 5-4b.

Note that, instead of combining it with film theory, α_b could in principle also be combined with either the diffusive or kinetic approach. The latter was done by Oinuma *et al*. [181], i.e. the only other reported use of α_b in context of plasma liquid modelling, to the best of our knowledge. However, this combination with either the diffusive or kinetic approach does not change the results of these approaches, because they already

overestimate the rate of dissolution significantly more compared to film theory, as mentioned in Section 3.2. In contrast, we can conclude that using α_b in combination with film theory can reach better agreement with experiments for species with low solubility.

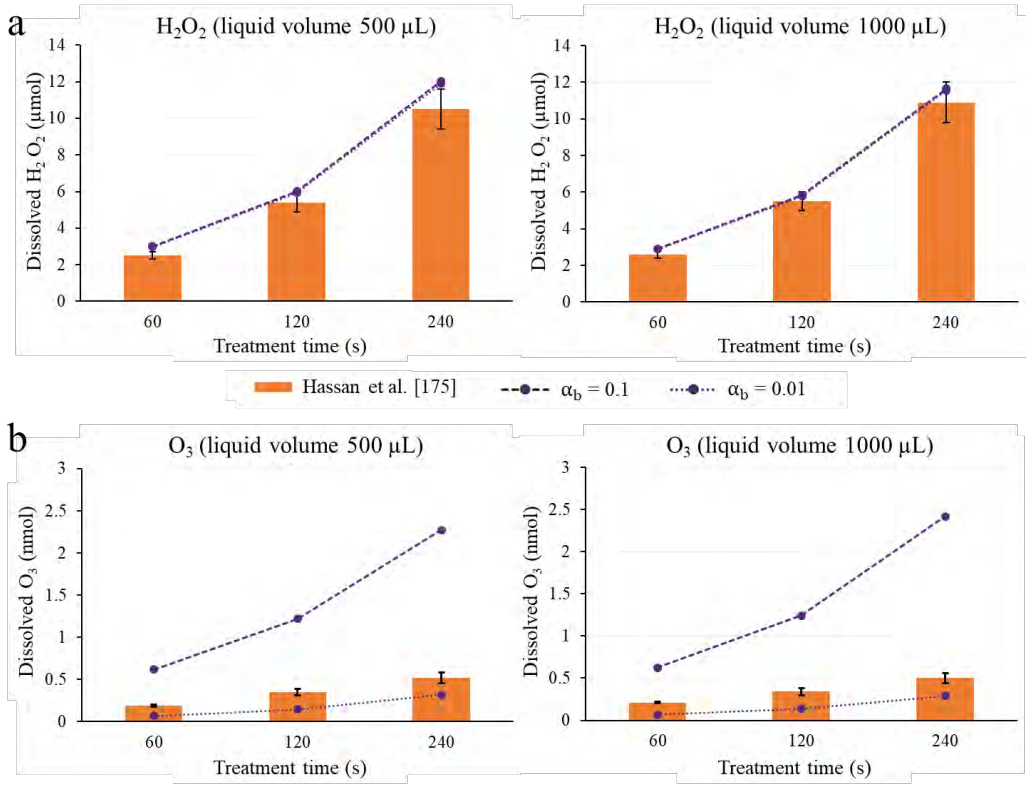

Figure 5-5. Total amount of dissolved H_2O_2 (a) and O_3 (b) over time, for a liquid volume of either 500 µL or 1000 µL, as calculated by our model using equation (E.5-7) as the boundary condition on the gas-liquid interface, for two values of α_b, compared to the experimental data reported in [175]. In (a), both curves overlap.

3.4 Results in the presence of liquid phase reactions

So far, we have used experimental data where liquid water was treated with a gas jet that contains a known amount of RONS, whose concentration was afterwards measured in the treated liquid, for both a RONS with high solubility (H_2O_2) and low solubility (O_3). These RONS virtually do not react in the liquid. It would be beneficial to evaluate equations (E.5-3) - (E.5-6), as well as whether equation (E.5-7) performs better, for other RONS that do react in the liquid phase. Indeed, liquid phase reactions significantly affect the transport processes at the gas-liquid interface [174].

Jablonowski *et al*. [177] reported such experiment for ·NO, again a RONS with low solubility ($\mathrm{H^{cc}} = 0.05$, at 300 K). Therefore, we adapted the geometry of our model again, to that used in [177]. As the ·NO concentration was determined using a spin trap (CPTIO), this indeed allows to investigate our model results in the presence of chemical reactions. The reaction system for ·NO implemented into our model consists of the following reactions [192, 193]:

$$\mathrm{CPTIO} + \cdot\mathrm{NO} \rightarrow \mathrm{CPTI} + \mathrm{NO_2} \quad \text{(R.5-1)}$$
$$k = 9.1\times10^{-18}\ \mathrm{cm^3 s^{-1}}$$

$$\mathrm{CPTIO} + \mathrm{NO_2} \leftrightarrow \mathrm{CPTIO^+} + \mathrm{NO_2^-} \quad \text{(R.5-2)}$$
$$k_f = 2.3\times10^{-14}\ \mathrm{cm^3 s^{-1}}$$
$$k_b = 1.5\times10^{-16}\ \mathrm{cm^3 s^{-1}}$$

$$\mathrm{CPTIO^+} + \cdot\mathrm{NO} + \mathrm{H_2O} \rightarrow \mathrm{CPTIO} + \mathrm{NO_2^-} + 2\mathrm{H^+} \quad \text{(R.5-3)}$$
$$k\times[H_2O] = 3.5\times10^{-16}\ \mathrm{cm^3 s^{-1}}$$

By evaluating the CPTI concentration in this model, we can evaluate how well the dissolution of ·NO is simulated. Other reactions of ·NO in water, e.g. with O_2 or NO_2, are multiple orders of magnitude slower than the reaction with the spin trap at the conditions under study and can thus be neglected here.

Secondly, Hassan *et al*. [176] recently published a follow-up to their earlier work, this time with experimental data for HNO_2. Compared to O_3 and H_2O_2, this species has a more intermediate solubility ($\mathrm{H^{cc}} = 1.1 \times 10^3$, at 300 K). As HNO_2 dissociates in water, this again allows us to investigate the model results in the presence of chemical reactions, i.e.:

$$\mathrm{HNO_2} \leftrightarrow \mathrm{NO_2^-} + \mathrm{H^+} \quad \text{(R.5-4)}$$
$$\mathrm{pKa} = 3.4$$

Unfortunately, no data is available regarding the mass accommodation coefficient of either ·NO or HNO_2. Meanwhile, fitting the model to find some optimal value of α_b would decrease its reliability and usability outside of the range of experimental parameters (in this case, the model geometry and precise chemical species) it was fitted to. Therefore, in first approximation, we test both the upper and lower limit used previously for O_3. Indeed, looking at the available values reported for different RONS,

none are higher than α_b = 0.1, and only few are lower than α_b = 0.01 [191]. Thus, when no data is available, this range seems a reasonable first approximation. Figure 5-6 presents the results using this approach. Using Henry's law directly (equation (E.5-2)), once again significantly overestimates the dissolution for both ·NO and HNO_2, though less severely than for O_3, which could be expected, as chemical reactions in the liquid in principle increase the effective solubility of the species [153]. For HNO_2, which already has a higher solubility on its own, the overestimation is a factor ~2. Using equation (E.5-7), the upper limit of α_b = 0.1 now approximates the measured values most closely, for both species.

Notably, the experimental data in Figure 5-6b indicates that after 120 s treatment, more than double the amount of HNO_2 has dissolved compared to after 60 s, which is not predicted by the modelling results using equation (E.5-7). In fact, in the simulation results, a saturation effect can even be observed already, which does correspond well with the experimental results at 240 s. This is expected, as the dissolved amount of HNO_2 gets closer to its saturation concentration (i.e. 3560 nmol HNO_2 for the liquid volume of 500 µL). A possible explanation could be that the mass accommodation coefficient changes with the amount of HNO_2 already dissolved. Indeed, from reported data for HNO_3 it seems that α_b is higher for solutions that already contain HNO_3 compared to for pure water [191]. However, as we have no data for the mass accommodation coefficient of HNO_2, this only remains speculative for now.

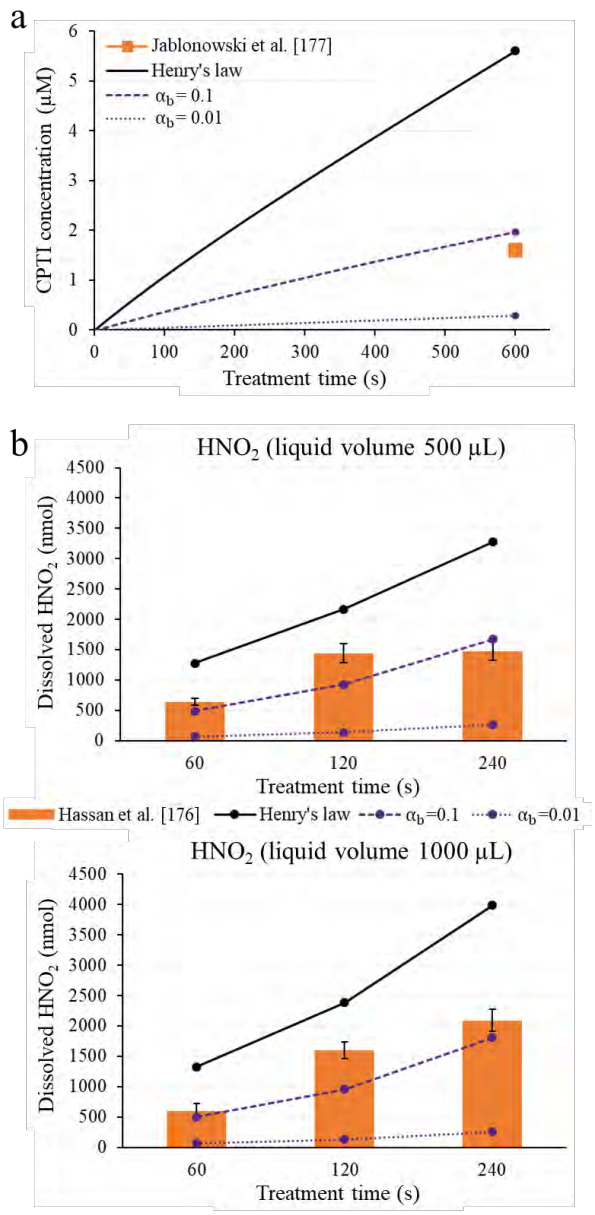

Figure 5-6. Model results for reacting systems in the liquid using either Henry's law directly, or equation (E.5-7) for two values of α_b as the boundary condition on the gas-liquid interface. (a) Total formed CPTI over time, formed through reaction of CPTIO with ·NO and thus a measure of the amount of dissolved ·NO. Modelling results are compared to the experimental data reported in [177]. (b) Total amount of dissolved HNO_2 over time, for a liquid volume of either 500 µL or 1000 µL. Modelling results are compared to the experimental data reported in [176].

Taken together, our results indicate that many of the boundary conditions used in computational plasma-liquid research so far to describe the transfer of chemical species between the gas and liquid phase, are unable to reproduce experimental results for species with low solubility. By combining film theory and mass accommodation to describe transport at the interface, we reach a better agreement with experiments, at least for the RONS simulated in this chapter.

One should note that equation (E.5-7) is still a very simplified way of describing the dissolution process. Film theory was first proposed a century ago by Lewis and Whitman [194]. Since then, it has been expanded into more sophisticated descriptions such as Danckwerts' surface renewal theory [195], or the resistance model, which more formally separates the different transport processes near the interface [188]. Implementation of more sophisticated descriptions could result in even better correlation with experimental values. However, the lack of data for the mass accommodation coefficient for many RONS remains an obstacle in reaching a robust description of the dissolution process in plasma-liquid research.

Finally, it must be noted that the above discussion only applies directly to neutral RONS. For charged species, when actually included into the model, most works assume that the species are able to directly enter into the liquid phase without constraints [112-115, 118, 178, 180, 183]. It is difficult to test whether this approach is correct, as comparison to experimental data is not available for charged species. When the plasma is close to or in contact with the liquid, the transport of charged species towards the liquid can additionally be influenced by the electric field and the formed plasma sheath, further complicating the description of interfacial mass transport in plasma-liquid interaction [196].

4. Conclusion

In this chapter, we studied several interfacial boundary conditions to describe species transfer over the gas-liquid interface, as used in various published multidimensional plasma-liquid models. By comparing the results to experimental data, we show that the different expressions are unable to replicate measurements for all RONS. Specifically, we found that all formulas perform well for H_2O_2, which has high solubility, but severely overestimate the rate of dissolution for O_3, $\cdot NO$ and HNO_2, which have intermediate to low solubility. This discrepancy has likely gone unnoticed due to a lack in comparison

between modelling results and experimental data for poorly soluble species. Indeed, rigorous benchmarking of different aspects of a computational model is crucial to increase confidence in the model and thus improve our understanding of the simulated system. In the end, we proposed a first step towards a more accurate description of species dissolution, by combining film theory with the mass accommodation coefficient, for improved multidimensional computational modelling. We hope that this work can be used to investigate and enhance the description of RONS dissolution into water during plasma-liquid interaction even more in the future.

If we look back at the past three chapters, we have used our 2D-axisymmetric fluid model, explained and benchmarked in Chapter 2, to describe various aspects of the *in vitro* treatment of a liquid with a plasma jet. Specifically, we have applied our model to study examples where a lack of uniformity in literature can make results difficult to directly compare to one another, both for experimental and computational works, and studied to what degree the treatment might be affected by these parameters. While our model has proven useful to simulate and study the physical phenomena that occur in the studied systems, it is not suitable to elucidate the actual, biological effects that plasma treatment may induce in treated (cancer) cells. To gain insight into such effects, a different type of modelling is required. This will form the subject of the next chapter.

Chapter 6

Effect of plasma-induced oxidation on NK cell immune checkpoint ligands

The content of this chapter is based on:

Effect of plasma-induced oxidation on NK cell immune checkpoint ligands: A computational-experimental approach
Pepijn Heirman*, Hanne Verswyvel*, Mauranne Bauwens, Maksudbek Yusupov, Jorrit De Waele, Abraham Lin, Evelien Smits and Annemie Bogaerts
Redox Biology, 77, 103381 (2024)
https://doi.org/10.1016/j.redox.2024.103381

This is a shared chapter between myself and Hanne Verswyvel. We contributed to this research equally (respectively providing the computational and experimental data). Shared first authorship is indicated above (*).

In this chapter, we investigate the chemical and biological effects of CAP-induced oxidation on several key immune checkpoints of natural killer (NK) cell function. We use molecular dynamics (MD) simulations to investigate the effect of CAP-induced oxidative changes on the MHC-I complexes HLA-Cw4 and HLA-E. Our simulations indicate that these chemical alterations do not significantly affect the binding affinity of these markers to their corresponding NK cell receptor, which is supported with experimental read-outs of ligand expression on human head and neck squamous cell carcinoma cells after CAP application. Broadening our scope to other key ligands for NK cell reactivity, we demonstrate rapid reduction in CD155 and CD112, target ligands of the inhibitory TIGIT axis, and in immune checkpoint CD73 immediately after treatment. Besides these transient chemical alterations, the reactive species in CAP cause a cascade of downstream cellular reactions. This is underlined by the upregulation of the stress proteins MICA/B, potent ligands for NK cell activation, 24 h post treatment. Taken together, this data corroborates the immunomodulatory potential of CAP, and sheds light on the interaction mechanisms between CAP and cancer cells.

1. Introduction

Apart from the studies that show CAP can induce immunogenic cell death [56, 57, 62, 66], as discussed at length in Chapter 1, CAP treatment has shown positive effects on various immune cell types. Macrophages exhibit an improved response against plasma-treated cancer cells [54, 197], while dendritic cells indicate improved infiltration and antigen presentation after treatment *in vivo* [71]. On the other hand, the effect of CAP on other immune cells, such as the natural killer (NK) cells that play an important role in the body's cancer immunosurveillance [23], has not yet received much attention [66]. Because of their ability to directly recognize and kill cancer cells, they do however form an attractive target in immunotherapy [64, 198].

In previous work, we reported that treatment of skin cancer cells with CAP augmented NK cell-mediated toxicity *in vitro* [70]. Improved NK cell cytotoxicity was also shown *in vivo*, after treatment of melanoma tumours with CAP [71]. The *in vitro* effects were attributed to the observed change of surface ligand expression on the treated cancer cells. Indeed, NK cell activity relies on the balance between activating and inhibiting signals received through surface receptors, which bind to relevant ligands on the target cell membrane [25]. The interaction between these immune cells and cancer cells is complex, involving numerous ligand-receptor interactions that contribute to the delicate activating/inhibiting balance. Hence, a comprehensive analysis of several key tumour cell - NK cell axes would enhance our understanding of the signalling mechanisms underlying the improved NK cytotoxicity.

Among the key ligands that inhibit NK cells are MHC-I molecules (cf. Chapter 1). NK cells express several receptors that recognize MHC-I, with killer immunoglobulin-like receptors (KIR) recognizing the classical HLA-A, B and C ligands, and natural killing group 2, type A, (NKG2A) acting as an inhibitory receptor for the non-classical MHC-I complex HLA-E [24, 25, 199, 200]. In [70], we previously showed altered expression of both HLA-A/B/C and HLA-E on skin cancer cells after CAP treatment *in vitro*. The fact that CAP treatment is able to change the expression of surface ligands that are important for cancer – immune cell crosstalk is now observed in several studies, and is an appealing therapeutic characteristic for further investigation [69-71].

In addition to affecting the expression of ligands on the cancer cell surface, RONS can chemically interact directly with the ligands already expressed on the cells. In this way, CAP treatment can induce a broad range of post-translational modifications (PTMs) in

proteins [165]. Computational molecular dynamics (MD) simulations have proven a valuable tool to investigate the effects of these PTMs [94], which can lead to conformational changes and affect the ability of protein ligands to bind to their receptors [67, 138, 139]. On the other hand, oxidation does not necessarily disrupt normal protein function in all cases. Indeed, while Ghasemitarei *et al.* [201] found that oxidation of cysteine inside the protein channel of the xC- antiporter severely impaired cystine uptake by the channel, a similar oxidation did not have a strong effect on transport through the AQP1 channel, as shown by Yusupov *et al*. [136].

In this chapter, we employ non-reactive MD simulations to investigate the effect of CAP-induced oxidative changes on the MHC-I complexes HLA-Cw4 and HLA-E. Umbrella sampling (US) is used to determine the binding energy of these MHC-I complexes to their NK cell receptor, respectively KIR2DL1 and NKG2A/CD94. To complement these simulations with experiments, we analyse the expression of these ligands on three head and neck squamous cell carcinoma (HNSCC) cancer cell lines, a cancer type known for NK cell enrichment [202]. Both the *in silico* and *in vitro* approach reveal only limited effects of therapy-induced oxidation. Thus, we subsequently expand our focus to the expression of various NK-regulating ligands, including the T cell immunoreceptor with Ig and ITIM domains (TIGIT) receptor ligands CD155 and CD112 and immune checkpoint CD73, and discover a rapid reduction of these targets upon CAP exposure. Furthermore, the NK cell activating MICA/B proteins are found to be upregulated on the cellular membrane 24 h post-treatment. This demonstrates the complex chemical and biological interactions between CAP and cancer cells, with regard to NK cell recognition. Finally, the data in this chapter points out interesting targets for therapy-induced oxidation and can provide the groundwork for further research in the future.

2. Methods

2.1 Computational methods

2.1.1 Preparation of the model systems

Figure 6-1 illustrates the two NK cell inhibiting ligand-receptor protein complexes computationally investigated in this study, i.e., HLA-Cw4 – KIR2DL1 (left) and HLA-E – NKG2A/CD94 (right). MHC-I molecules consist of a variable α-chain that presents an intracellular peptide (shown in red), and the smaller β2-microglobulin (β2M, shown in orange) [22]. HLA-E is recognised by the NK cell inhibiting receptor NKG2A, which forms a heterodimer with CD94 in order to become a functional receptor. In contrast to HLA-E, which has a low degree of polymorphism [203], HLA-A, B and C are extremely diverse, as is the group of NK cell receptors that bind to them, i.e. KIR. As discussed by Parham [204], HLA-C is the most important classical MHC-I protein in humans. In addition, of the group of inhibitory KIRs that recognize the various types of HLA-C, KIR2DL1 is the most inhibitory to NK cells.

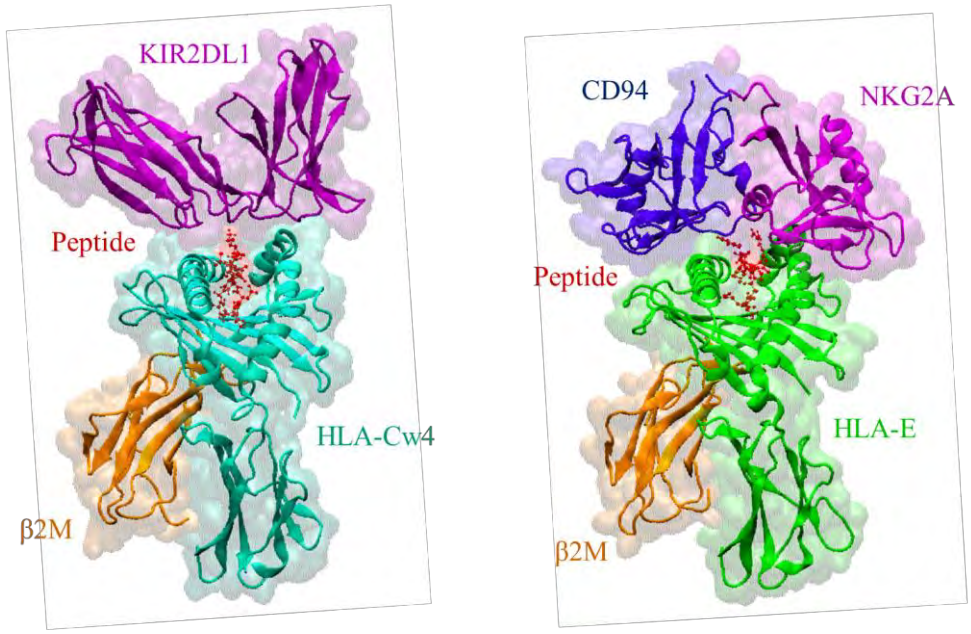

Figure 6-1. Schematic representation of the two protein complexes computationally studied, i.e., HLA-Cw4 – KIR2DL1 (left) and HLA-E – NKG2A/CD94 (right).

To elucidate the effect of oxidation on the binding of the investigated complexes, we performed non-reactive MD simulations. The simulations were performed with the

GROMACS software (version 2020.2) [205], employing the GROMOS 54A7 force field [206]. The crystal structures of both the NKG2A/CD94 – HLA-E complex and the KIR2DL1 – HLA-Cw4 complex were obtained from the Protein Data Bank (ID: 3CDG [207] and 1IM9 [208], respectively). Force field parameters for the oxidised amino acids were obtained from [209].

Each model system was prepared by placing the protein complex in a cubic simulation box with periodic boundary conditions applied in all Cartesian directions, and solvating in SPC water [210] containing a concentration of 150 mM NaCl. A minimum distance of 1 nm was ensured between the protein and the box sides to adhere to the minimum image criterion. The system was energy minimised using the steepest descent algorithm, followed by a 2 ns equilibration in the canonical (NVT) ensemble (i.e. a constant number of particles (N), volume (V) and temperature (T)) while applying position restraints with a force constant of 10 000 $kJ \cdot mol^{-1} \cdot nm^{-2}$ to the heavy atoms of the proteins. Afterwards, a series of equilibrations, totalling 10 ns, was performed in the isothermal-isobaric (NPT) ensemble (i.e. with a constant pressure (P) instead of a constant volume) while enforcing decreasingly strong position restraints (10 000 $kJ \cdot mol^{-1} \cdot nm^{-2}$ for 2 ns, 1000 $kJ \cdot mol^{-1} \cdot nm^{-2}$ for 2 ns, 200 $kJ \cdot mol^{-1} \cdot nm^{-2}$ for 6 ns). In this way, the complexes were gradually equilibrated. The equilibrations were performed at 310 K and 1.0 bar to mimic the conditions the proteins would experience in the body, employing the v-rescale thermostat [211] with a coupling constant of 0.1 ps and the Parrinello-Rahman barostat [212] with a compressibility and coupling constant of 4.5×10^{-5} bar^{-1} and 2 ps, respectively. Electrostatics in the system were treated using the reaction field (RF) method [213], while using a cutoff distance of 1.4 nm for the van der Waals and Coulomb interactions. All simulations were performed with a time step of 2 fs. A final equilibration, without enforcing any position restraints on the system, was performed for up to 350 ns, depending on the simulated system.

Each system was simulated in triplicate, with different initial velocities, meaning a total of 12 systems (2 protein complexes, both in native and oxidised states) were used for our investigation. The final equilibration of each system was used to calculate the root-mean-square deviation (RMSD) of the alpha-carbons (Cα atoms) of the protein complexes. In addition, the last 100 ns were used to investigate the root-mean-square fluctuations (RMSF) of the protein residues, as well as the secondary structure of the fully equilibrated complexes and the salt bridge connections between ligand and receptor. For the latter, the VMD software [214] was used.

2.1.2 Investigating the binding affinity of the complexes

To investigate the binding affinity of the complexes, the fully equilibrated protein complex was placed in a new, triclinic simulation box that was elongated in the z-direction, and again solvated in SPC water containing 150 mM NaCl. The complex itself was oriented along the z-axis, i.e., the contact plane between the ligand and receptor was made approximately perpendicular to the z-axis. Next, a new energy minimisation, NVT equilibration (2 ns) and NPT equilibration (30 ns) were performed, all while applying position restraints of 1000 $kJ \cdot mol^{-1} \cdot nm^{-2}$ to the heavy atoms of the protein.

The complex was then pulled apart by subjecting the NK cell receptor (i.e., NKG2A/CD94 or KIR2DL1) to a harmonic potential with a force constant of 1000 $kJ \cdot mol^{-1} \cdot nm^{-2}$, at a constant velocity of 0.1 nm/ns for 40 ns. The centre of mass of NKG2A/CD94 was pulled against the backbone atoms of Lys6, Tyr7, Phe8 and His9 of the HLA-E protein, while the centre of mass of KIR2DL1 was pulled against the backbone atoms of Gln96, Arg97, Met98 and Phe99 of the HLA-Cw4. The above residues were chosen for each complex because they are buried inside the protein under the ligand-receptor binding domain, are approximately centred around the z-axis, and exhibit minimal fluctuations compared to other residues in the protein. To prevent movement of the ligand while retaining its flexibility, position restraints were applied to the Cα atoms of Phe36, Cys101, Phe116 and Cys203 (for HLA-E) and Glu63, Tyr118, Tyr159 and Ala205 (for HLA-Cw4). These residues were again chosen as they are buried inside the protein and exhibit low fluctuation. Finally, to prevent movement of the pulled protein (i.e. NKG2A/CD94 or KIR2DL1) in the xy-plane, so-called flat-bottomed position restraints were applied with a radius of 0.05 nm and a force constant of 500 $kJ \cdot mol^{-1} \cdot nm^{-2}$.

Along the reaction coordinate of each pulling simulation, 40 frames (later supplemented up to 53 frames to ensure adequate sampling) separated by 0.1 nm were isolated to serve as the initial structure in US simulations [215] to sample conformational space in a window at that pulled distance. For the native systems, US was performed for 50 ns, while for the oxidised complexes the US was performed for 75 ns. The last 25 ns of each US simulation were used for data collection (while the first part of the US was used to equilibrate the frame). To make sure that sampling adequately covered the reaction coordinate of the pulling simulations, we plotted the histograms of the US simulations. The plots can be found in Appendix D, showing a good overlap between neighbouring windows. To extract the free energy profiles along the pulling coordinate, the weighted histogram analysis method (WHAM) was employed [216].

2.1.3 Building the oxidised structures

The oxidised version of both investigated protein complexes was constructed with the Vienna-PTM web server [217] by replacing relevant native amino acids with their oxidised form. Which amino acids would be oxidised by CAP treatment was determined based on two factors: (i) the susceptibility of different amino acids to oxidation, and (ii) the accessibility of these amino acids in the investigated proteins to the solvent, and thus to plasma-produced RONS.

Different amino acids have different susceptibility to PTM after plasma treatment. Takai *et al*. [218] experimentally investigated the chemical modification of amino acids in solution through treatment with a plasma jet. A similar study was performed by Zhou *et al*. [219]. Wenske *et al*. [165, 220] reported the PTMs caused by plasma treatment, with both the kINPen and COST-jet, in different peptides, representing a more realistic environment for the different amino acids. It is clear that the amino acids that are most susceptible to plasma-induced PTM are the sulphur-containing methionine and cysteine. They are followed by the aromatic amino acids tryptophan, tyrosine and phenylalanine. Though CAP-induced modifications have been reported for most of the remaining amino acids, they exhibit a far lower susceptibility, e.g. only showing signs of PTM after lengthy CAP treatment. Which PTM occurs depends on various factors, including the plasma working gas, the plasma device, and the amino acid environment. The most common PTM induced by plasma, however, seems to be oxidation of the amino acid side chains [165]. Based on this, Figure 6-2 shows the plasma-induced PTMs we considered in our investigation.

To determine which of these amino acids specifically in our investigated complexes would be available for oxidation by plasma treatment, we analysed the solvent accessible surface area (SASA) of the proteins. For this, we repeated all simulation steps outlined in Section 2.1 for only the ligands of the complexes, i.e. HLA-E and HLA-Cw4. Indeed, in an experimental setting, plasma treatment of cancer cells would cause oxidation of only the ligands expressed on the cancer cells. The last 20 ns of the equilibrations were used for the SASA analysis. By comparing the SASA to the hydrophilic surface area of the amino acids in question [221], we can determine which amino acids can be easily reached by the solvent, and thus, by plasma-produced RONS.

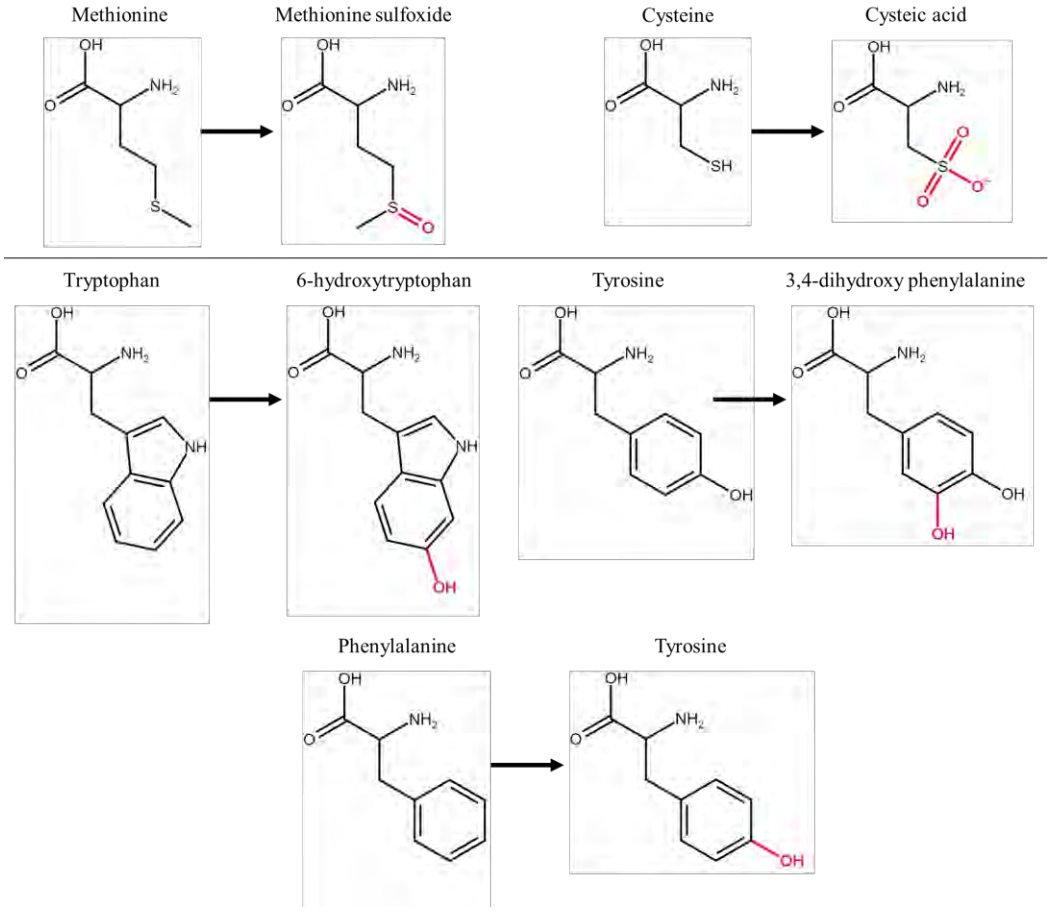

Figure 6-2. Chemical structures of sulphur-containing (top) and aromatic (bottom) amino acids with their oxidised forms (i.e. structures with atoms in red).

2.2 Experimental methods

2.2.1 Cell culture

Three human head and neck squamous cell carcinoma cell lines, Cal27, SCC61 and SCC22B, were used in this study. The Cal27 cell line was obtained from American Type Culture Collection (ATCC, Rockville, MD, USA), the SCC61 cell line was kindly provided by Prof. Dr. Sandra Nuyts (University Hospital Leuven, Leuven, Belgium), and SCC22B cells were kindly provided by Prof. Dr. Olivier De Wever (Laboratory of Experimental Cancer Research, Ghent University Hospital, Ghent, Belgium). Cell lines were commercially available and no ethical approval was required. Cells were cultured in Dulbecco's Modified Eagle Medium (DMEM, Life Technologies), supplemented with 10% fetal

bovine serum (FBS, Life Technologies), 1% L-glutamine (Life Technologies), and 1% Penicillin/Streptomycin (P/S; Life Technologies). Cell cultures were incubated in a humidified atmosphere at 37°C and 5% CO_2 conditions, and passaged when 80% confluence was reached to maintain exponential growth. Cell identity was confirmed via short tandem repeat profiling, and regular checks for mycoplasma infection were performed.

2.2.2 CAP treatment

A microsecond-pulsed dielectric barrier discharge (DBD) system, described in [67, 71, 222, 223], was used for the experimental part of this work. The set-up comprises a microsecond-pulsed power supply (Megaimpulse Ltd, Russia), with a round-bottom dielectrically covered electrode, providing an electrically and thermally stable plasma [71]. Detailed operation parameters can be found in Table 6-1.

Table 6-1. Experimental parameters for DBD-CAP application

Electrical and Operating Parameters	
Pulse voltage amplitude	30 kV
Pulse rise time	1-1.5 µs
Pulse width	2 µs
Pulse frequency	200 and 500 Hz
Treatment time	10 s
Application distance	1 mm

For all experiments, this microsecond-pulsed DBD system was used to treat HNSCC cells in 24-well plates when a confluence of 80% was reached, one day after experimental seeding. Cell culture medium was removed immediately prior to CAP application and the 24-well DBD probe was lowered into the well to the treatment distance (1 mm), using a z-positioner. Right after treatment, cells were overlayed with fresh culture medium. Plates were incubated for a day at 37°C and 5% CO_2 for 24 h post-treatment analysis, or processed right after treatment for immediate (0 h) analysis.

2.2.3 Flow cytometry analysis of NK ligands on HNSCC tumour cells

The NK ligands included in this study were measured individually via a dual staining of a viability stain (LIVE/DEAD™ Fixable Near-IR, APC-Cy7), and a monoclonal antibody against the target ligand (PE anti-HLA-C, anti-HLA-E, anti-CD155, anti-CD122, anti-CD73, or anti-MICA/B). Ligand expression was measured at two distinct time points to establish

a clear temporal separation between immediate chemical and later biological effects at 24 hours. In short, cells were washed with phosphate buffer saline (PBS), detached with accutase (Sigma-Aldrich), spun down and resuspended in FACS buffer (sheath buffer (BD Biosciences), with 0.1% BSA and 0.05% NaN_3). Cell density of untreated controls and CAP-treated samples was set at $5x10^5$ cells/mL. Samples were incubated with 1 µL of LIVE/DEAD™ Fixable Near-IR (L10119, ThermoFisher Scientific), and a single stain for a target ligand: anti-HLA-C (5 µL, Cat. No. 566372, BD), anti-HLA-E (5 µL, 12-9953-42, Invitrogen), anti-CD155 (5 µL, 566718, BD), anti-CD112 (5 µL, 337410, BioLegend), anti-CD73 (5 µL, 12-0739-42, Invitrogen), or anti-MICA/B (20 µL, 558352, BD). Fluorescence Minus One (FMO) gating controls were included for all cell lines and treatment conditions. After 30 minutes of incubation in the dark at 4°C, cells were washed twice with FACS buffer, and resuspended in 100 µL FACS buffer for read-outs. Sample acquisition was performed on the NovoCyte Quanteon (Agilent Technologies). Experimental data was gated and analysed using the FlowJo software version 10.8.1 (FlowJo LLC, Ashland, OR, USA) (see Appendix D).

2.2.4 Statistical analysis

Prior to statistical calculations, the Grubbs' Test was performed to detect significant outliers in the experimental data. Afterwards, the linear mixed model in JMP Pro17 (SAS Software, Tervuren, Belgium) was used to analyse statistical differences between treatment conditions. CAP exposure was designated as the fixed effect, while the different experimental repeats and the interaction between experiments and the date they were performed were considered as random effects. The random slope model was only retained when the treatment-date interaction was significant ($p \leq 0.05$). Statistical difference by the fixed effect was determined, and the post-hoc Dunnett's test was used to calculate adjusted p values of the treatments compared to untreated controls. P values equal or less than 0.05 were considered as statistically significant. Data in the experimental graphs is represented as mean ± SEM, with individual values shown as dots in the bar plots.

3. Results

3.1 Oxidation affects the protein complex structure, but not the binding free energy

To gain insight into how CAP-induced oxidation affects the MHC-I complexes HLA-Cw4 and HLA-E, we performed non-reactive MD simulations for both the native and oxidised version of both protein complexes. To construct the oxidised versions of the ligands, we chose to implement the oxidation products of only the amino acids that are known to be most susceptible to CAP-oxidation, i.e. Met, Cys, Trp, Tyr, and Phe, that additionally have a high solvent accessibility in the simulated proteins, meaning they can be reached by RONS dissolved in the surrounding liquid during CAP treatment. Table 6-2 indicates which amino acids were oxidised in our simulated systems. Notably, all cysteine residues in both HLA-Cw4 and HLA-E have a very low solvent accessibility, thus preventing oxidation of the disulfide bonds present in the protein complexes.

Table 6-2. List of amino acids used to construct the oxidised forms of the ligands (i.e. HLA-Cw4 and HLA-E).

	KIR2DL1 – HLA-Cw4	**NKG2A/CD94 – HLA-E**
HLA	Met98, Trp14, Trp133, Trp147, Trp204, Tyr 84, Tyr159, Phe8, Phe99, Phe116, Phe241	Met98, Trp51, Trp60, Trp204, Trp244, Tyr84, Tyr159, Phe8, Phe109, Phe116
β2M	Met0, Trp60, Tyr10, Tyr63, Phe22, Phe56, Phe62	Met0, Trp60, Tyr10, Tyr63, Phe22, Phe56, Phe62
peptide	/	Met2

Figure 6-3a shows the calculated RMSD of the simulated protein complexes in both native and oxidised form. Protein oxidation has been reported to cause conformational changes and to result in higher protein flexibility [94], as evident from larger (fluctuations in) RMSD. The oxidised versions of the simulated MHC-I complexes converge to an RMSD that is on average higher than the native structures. For HLA-Cw4 – KIR2DL1, the RMSD of the oxidised structure converges to an average value of 0.52 nm (averaged over the three replicas), compared to 0.38 nm for the native structure, while for HLA-E – NKG2A/CD94, the average converged RMSD is 0.44 nm for the oxidised

structure, compared to 0.32 nm for the native structure, indicating that the oxidised proteins indeed equilibrated to a different conformation.

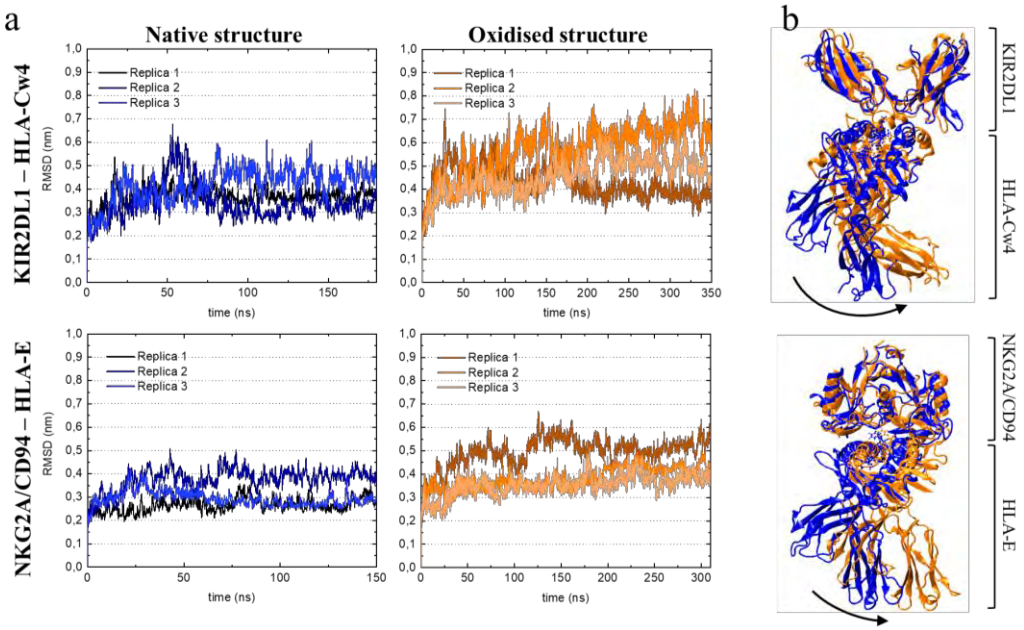

Figure 6-3. Oxidation-induced structural changes in the proteins. (a) RMSD of the Cα atoms of the native and oxidised protein complexes. (b) Cartoon view of representative frames (i.e., one of their replicas) for the native (blue) and oxidised (orange) protein complexes, aligned based on the non-oxidised receptors. The arrows highlight how the ligands have shifted in the oxidised structure.

On the other hand, the RMSD fluctuations do not exhibit a clear difference, which indicates that the flexibility of the ligands is not affected to a large degree by the oxidative changes. This is supported by the calculated RMSF of the ligands, as shown in Figure 6-4. For HLA-E, the RMSF is nearly unchanged after oxidation. For HLA-Cw4, the RMSF of the oxidised system is slightly higher in some regions, particularly near the oxidised residues, indicating a slightly increased local flexibility. Notably, the native HLA-Cw4 was calculated to already be more flexible than HLA-E.

While the RMSD of both simulated MHC-I complexes suggests they undergo a change in conformation after CAP-induced oxidation, they almost completely retain their secondary structure. Analysis of the secondary structure of the ligands is shown in Table 6-3. In the case of HLA-Cw4, the most prominent alteration in the secondary structure is a decrease in the turn structure, accompanied by an increase in random coil structures.

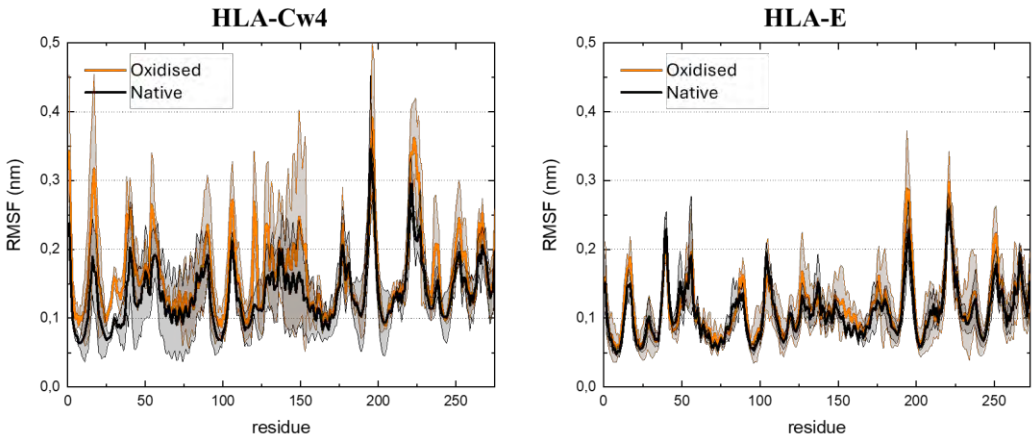

Figure 6-4. Protein flexibility is not significantly changed in the oxidised structures. The graphs show the RMSF of the residues of the native and oxidised ligands (i.e. HLA-Cw4 and HLA-E), averaged over the three replicas for each structure. Errors associated with sampling are shaded accordingly.

Table 6-3. Secondary structure analysis of the native and oxidised ligands (i.e. HLA-Cw4 and HLA-E). The values given indicate the relative occurrence (in %) of different conformations.

	HLA-Cw4		HLA-E	
	Native	**Oxidised**	**Native**	**Oxidised**
Turn	25.2 ± 1.2	22.1 ± 1.2	23.7 ± 1.2	23.4 ± 1.2
β-sheet/ β-bridge	41.0 ± 1.0	39.8 ± 1.1	41.8 ± 0.8	41.1 ± 0.8
Helix	17.6 ± 0.8	18.4 ± 0.8	18.2 ± 0.7	17.7 ± 0.6
Random coil	16.2 ± 1.2	19.7 ± 1.3	16.3 ± 1.0	17.8 ± 1.0

For HLA-E, the most notable change in secondary structure is a slight decrease in the helical structure, again accompanied by an increase of random coils. Visual inspection indicated that this change is caused by denaturation of the helix between residues 49 and 54, likely as a result of the two tryptophan oxidations (Trp51 and Trp60) in this region. Visual inspection also revealed that the most notable conformational change of the oxidised proteins compared to their native structure is a pivot of the ligand with respect to the domain that binds to the receptor. This occurs for both simulated protein complexes, and explains the higher average RMSD, although the precise extent of the

pivot differed over time (during the simulation, as the protein conformation fluctuates) and between the simulation replicas. The pivot is clearest when aligning the native and oxidised version of the protein based on only the receptor chains, i.e. the protein chains that were not oxidised, which is shown in Figure 6-3b.

To investigate if the oxidation affects the binding affinity of the investigated protein complexes, we performed pulling simulations followed by US simulations to determine the free energy profiles along the binding coordinate for each complex. One can see in Figure 6-5 that the oxidation of the ligands had minimal effect on the profiles. The binding free energy, i.e. the depth of the potential well, was calculated to be -82 ± 4 kJ/mol for HLA-Cw4 – KIR2DL1 in its native form, changing to -89 ± 5 kJ/mol when oxidised. For the HLA-E – NKG2A/CD94 complex, the calculated binding energies of the native and oxidised forms are -138 ± 12 kJ/mol and -122 ± 19 kJ/mol, respectively. Our simulations thus predict that, given the errors associated with the energy profiles, both investigated ligands respectively have similar binding affinity to their NK cell receptor regardless of being subjected to oxidation through plasma treatment.

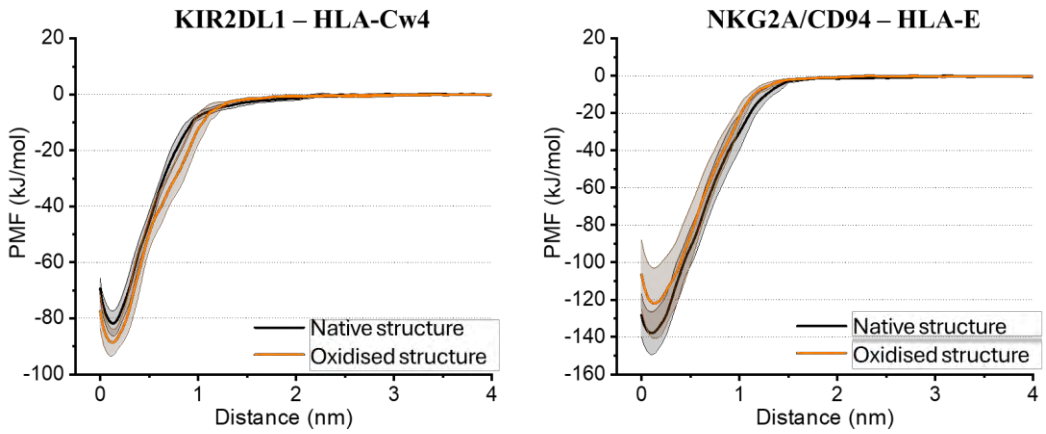

Figure 6-5. Oxidation does not affect the binding affinity of the protein complexes. Free energy profiles (i.e. potential of mean force, PMF) of the native and oxidised protein complexes. Errors associated with sampling are shaded accordingly.

3.2 A closer look at the connections between the ligands and receptors

The binding of HLA-E to NKG2A/CD94 is dominated by polar interactions mediated by several hydrogen bonds and a number of salt bridges. The crystal structure of HLA-E – NKG2A/CD94 exhibits five salt bridges [207]. Table 6-4 shows the binding persistence for the salt bridges found in our simulations, i.e. the percentage of time in which the amino acids that form the salt bridge are actually interacting. To consider a salt bridge as "interacting", we employed a distance threshold of 4.5 Å [224]. In addition, we only included interactions with a binding persistence of over 5%, unless specified otherwise. The salt bridges that are present in the crystal structure are highlighted. Notably, two of these salt bridges ($Asp163^{CD94}$ – $Arg75^{HLA\text{-}E}$ and $Arg137^{NKG2A}$ – $Glu154^{HLA\text{-}E}$) had a very low binding persistence in our simulations. On the other hand, several salt bridges not reported to be present in the crystal structure are predicted by our simulations to be (transiently) present in solvated state.

For the interaction between HLA-E and CD94, the most notable change in the oxidised state is a weaker binding of the salt bridge $Arg168^{CD94}$ – $Asp68^{HLA\text{-}E}$, as evidenced by the 21% decrease in binding persistence. Some of the salt bridges that contribute to the interaction between HLA-E and NKG2A seemingly exhibit a decrease in binding for the oxidised state as well, though this is mostly accompanied by an increase in binding to another amino acid close by. The reduced binding of $Asp162^{HLA\text{-}E}$ to $Arg215^{NKG2A}$ is accompanied by an enhanced binding to $Lys199^{NKG2A}$, while the lower binding of $Lys217^{NKG2A}$ to $Glu161^{HLA\text{-}E}$ coincides with increased binding to $Asp162^{HLA\text{-}E}$. Finally, the binding of salt bridge $Lys199^{NKG2A}$ – $Glu166^{HLA\text{-}E}$ is increased for the oxidised complex. However, unlike for the other salt bridges, this changed behaviour was present in only one simulation replicate in which this interaction was very significant, while not being significantly present (<10%) in any of the other replicates.

Table 6-4. Binding persistence (i.e. percentage of time that the N-O distances are below 4.5 Å) of the salt bridges that play an important role in the ligand-receptor complex systems, during the last 100 ns of the three replicate simulations. The salt bridges that are present in the crystal structure of the complexes are written in italic.

		Salt bridge binding	
HLA-E	**CD94**	**Native**	**Oxidised**
Arg68	Glu164	29%	20%
Arg68	Asp168	51%	30%
Asp69	*Arg171*	*26%*	*20%*
Arg75	*Asp163*	*1%*	*4%*
Arg75	Glu164	9%	4%
Arg79	Asp163	26%	19%
HLA-E	**NKG2A**		
Asp149	Arg137	8%	5%
Glu154	*Arg137*	*6%*	*7%*
Glu161	Lys217	28%	8%
Asp162	*Lys199*	*37%*	*47%*
Asp162	Arg215	17%	6%
Asp162	*Lys217*	*15%*	*20%*
Glu166	Lys199	4%	34%

		Salt bridge binding	
HLA-Cw4	**KIR2DL1**	**Native**	**Oxidised**
Arg69	Glu21	12%	0%
Lys80	Asp183	42%	25%
Lys80	*Glu187*	*47%*	*68%*
Arg145	*Asp135*	*18%*	*5%*
Lys146	Asp135	0%	31%
Lys146	*Asp183*	*90%*	*2%*
Lys146	Glu187	15%	10%
Lys8 (peptide)	Glu187	30%	30%

Compared to NKG2A/CD94, KIR receptors have a smaller interaction surface with MHC-I molecules. This is accompanied by fewer interactions between the receptor and its ligand, which is reflected in the lower calculated binding energy (Figure 6-5). The interaction between HLA-Cw4 and KIR2DL1 is again dominated by polar interactions, including three salt bridges that are found in the crystal structure of the complex [208]. Two of these salt bridges ($Asp135^{KIR2DL1}$ – $Arg145^{HLA\text{-}Cw4}$ and $Asp183^{KIR2DL1}$ – $Lys146^{HLA\text{-}Cw4}$) are conserved across HLA-C molecules, while the third ($Glu187^{KIR2DL1}$ – $Lys80^{HLA\text{-}Cw4}$) is unique to KIR2DL1, and plays an especially important role in the binding of this complex [204]. As shown in Table 6-4, the oxidation of HLA-Cw4 was found to affect these salt bridges in different ways. The $Glu187^{KIR2DL1}$ – $Lys80^{HLA\text{-}Cw4}$ salt bridge was calculated to have an increased binding persistence, implying a stronger interaction. Meanwhile, the binding of the other two salt bridges decreases. Both distance changes correspond logically to the observed pivot of oxidised HLA-Cw4 with respect to KIR2DL1, shown earlier in Figure 6-3. When looking at the calculated binding free energy, these effects (i.e. the stronger $Glu187^{KIR2DL1}$ – $Lys80^{HLA\text{-}Cw4}$ interaction and weaker $Asp135^{KIR2DL1}$ – $Arg145^{HLA\text{-}Cw4}$/ $Asp183^{KIR2DL1}$ – $Lys146^{HLA\text{-}Cw4}$ interaction) however seem to cancel out, as we observed no significant effect of the investigated oxidations on the binding free energy. In addition to the salt bridges discussed above, a few additional salt bridges were found to be transiently present in our simulations. Except for the salt bridge $Glu21^{KIR2DL1}$ – $Arg69^{HLA\text{-}Cw4}$, these additional salt bridges are the result of promiscuous interactions between the amino acids that already form salt bridges in the crystal structure. A special case is the salt bridge $Asp183^{KIR2DL1}$ – $Lys146^{HLA\text{-}Cw4}$. These amino acids did not interact in any of the simulations, as their relative distance was too large, except in replicate 2 of the oxidised system, where a salt bridge formed with a persistence of 92% in the equilibrated part of the simulation. This replicate underwent the largest pivot of HLA-Cw4 with respect to KIR2DL1, also evident from its RMSD (see Figure 6-3a), allowing formation of this new interaction.

In summary, our simulations indicate that CAP-induced oxidations alter the structure of the investigated ligand-receptor complexes, but do not affect their binding strength. To complement these computational results experimentally, we monitored the expression status of these protein complexes following plasma treatment of cancer cells *in vitro*.

3.3 MHC-I complexes HLA-C and HLA-E are moderately altered after CAP application

To determine the immediate oxidative effects of CAP on the MHC-I complex molecules HLA-C and HLA-E in an experimental setting, different HNSCC cell lines were exposed to CAP and immediately analysed for ligand expression (0 h analysis). While no significant differences in mean fluorescence intensity (normalised ΔMFI) were reported for HLA-E across all cell lines (Figure 6-6b), detection of HLA-C decreased significantly compared to untreated controls in the SCC61 cell line (Figure 6-6a, middle panel). At a CAP regime of 200 Hz, HLA-C expression was reduced by 1.4-fold, which further diminished to more than a 2-fold reduction in expression levels with a 500 Hz regime (0.69 and 0.44, respectively; $p \leq 0.0317$).

Besides immediate oxidative effects at the cell surface, CAP exerts more pleiotropic and downstream effects on cancer cells [71, 139, 225, 226]. Therefore, the expression levels of these MHC-I molecules were also measured 24 h after CAP application. This time point was selected with the specific aim of differentiating between the immediate chemical effects (e.g., oxidative) of plasma treatment and the subsequent biological response of the cells at 24 hours. Indeed, including an intermediate time point (e.g., 4 or 12 hours) would complicate this distinction, as it would likely reflect a mixture of diminishing chemical, but also early biological responses, making it challenging to delineate the independent contributions of each. Cellular responses in HLA-C and HLA-E expression toward CAP were limited for all cell lines, except for a significant upregulation in HLA-E expression (3.07; $p = 0.0455$) at a low CAP regimen in the Cal27 cell line (Figure 6-6b, left panel).

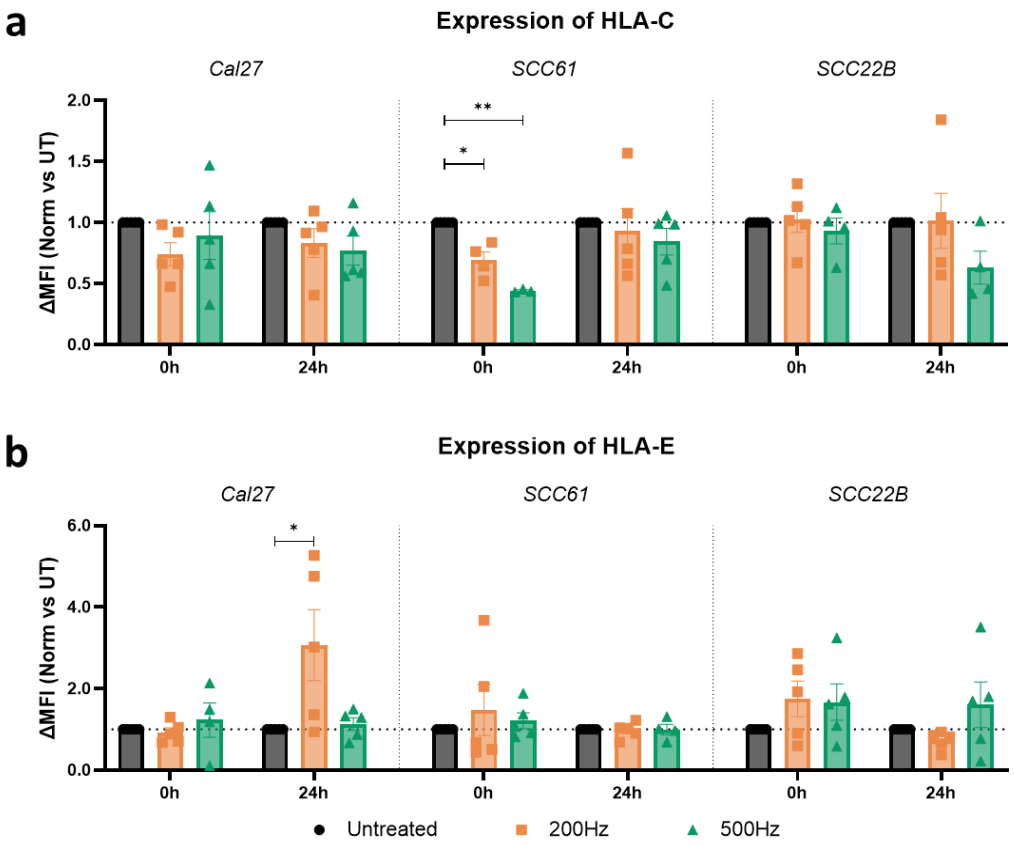

Figure 6-6. Exposure to CAP results in moderate expressional changes of the MHC-I complexes HLA-C and HLA-E in several HNSCC cell lines. Quantification of (a) HLA-C and (b) HLA-E expression after exposure to different regimes of CAP. Results are depicted as mean fluorescence intensity (MFI) minus FMO control, normalised to untreated controls (normalised (Norm) ΔMFI), immediate (0 h) and one day (24 h) post-treatment for all three HNSCC cell lines. Data are represented as mean ± SEM, with individual values shown (n = 5). Statistical significance between untreated cells and the treated conditions was determined using the generalised linear mixed model with post hoc Dunnett's test (* $p \leq 0.05$; ** $p \leq 0.01$). Outliers were calculated with the Grubbs' Test.

3.4 Key targets in the TIGIT axis are downregulated by CAP-induced ligand oxidation

As NK functionality is determined by the integration of complex activation and inhibition signals rather than a single interaction impulse [227-229], we subsequently investigated a panel of key tumour ligands of the TIGIT receptor, a major inhibitory pathway for NK functionality [227, 230]. CD155 and CD112 are inhibition signals for this highly immunosuppressive axis, though CD115 is the dominant antigen while the binding with CD112 is weaker [230, 231]. As recent studies indicated that targeting of CD155 and CD73 works synergistically and surpasses the failure in overcoming NK cell dysfunction by CD155 monotherapy [230], we also included this immune checkpoint in the analysis (Figure 6-7).

Immediate CAP-induced oxidation of the target ligand resulted in significantly reduced expression of both CD155 and CD112, in the Cal27 and SCC61 cell line with the higher treatment regime (0 h; 500 Hz), as shown in Figure 6-7a,b. Both ligands were diminished with 21.9% and 24.8%, respectively. for the Cal27 cell line, while 12-15% reduction was noted for SCC61 ($p \leq 0.0304$). These effects became even more pronounced for the immune checkpoint CD73 with a strong decline in ΔMFI, around 36%, for both cell lines (Figure 6-7c). It needs to be stated that these oxidative effects are transient, as 24 h later, expression levels stabilised again to baseline. It is apparent that both cell lines responded very similar to therapeutic oxidation, while the SCC22B cell line exploits a more robust, oxidation-resistant phenotype. Although a trend in decreased CD155-ΔMFI could be observed (1 vs 0,77; $p = 0.094$), this was not captured in the immediate CD122 and CD73 expression profile (Figure 6-7a-c, right panel). Nevertheless, a dose-dependent decrease in CD112 was observed 24 h after treatment, thus suggesting a downstream, stress-induced cellular response in target downregulation, rather than instant oxidative effects of the applied CAP in this cell line.

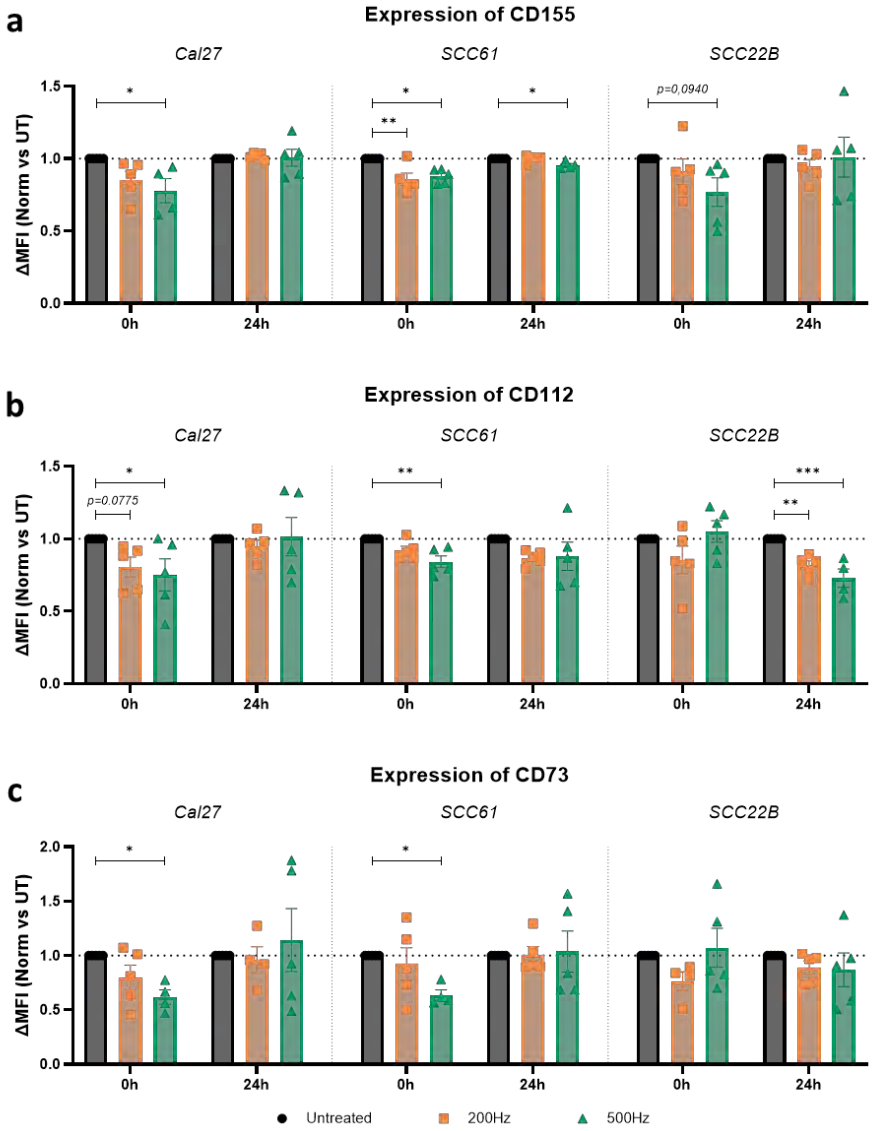

Figure 6-7. CAP reduces the expression of key targets in the TIGIT axis and CD73 immediately after treatment exposure. Flow cytometric quantification of the TIGIT receptor ligands (a) CD155 and (b) CD112, and (c) immune checkpoint CD73. Expression levels are depicted as mean fluorescence intensity minus FMO control, normalised to untreated controls (Norm ΔMFI), immediate (0 h) and one day (24 h) post-treatment for all three HNSCC cell lines. Data are represented as mean ± SEM, with individual values shown (n = 5). Statistical significance between untreated cells and the treated conditions was determined using the generalised linear mixed model with post hoc Dunnett's test (* $p \leq 0.05$; ** $p \leq 0.01$; *** $p \leq 0.001$). Outliers were calculated with the Grubbs' Test.

3.5 CAP stimulates expression of activating NK ligand MICA/B

Lastly, to further evaluate the delicate balance between activating/inhibiting signals on NK cells following CAP treatment, we evaluated the influence of CAP on the activating NK ligand MICA/B. Our data showed that oxidation-induced effects, immediately after application, were limited (Figure 6-8). Ligand expression decreased by 28% (1 vs 0.72; *p = 0.0415*) after 500 Hz application in the Cal27 cell line, while these effects were not measured in the other two cell lines.

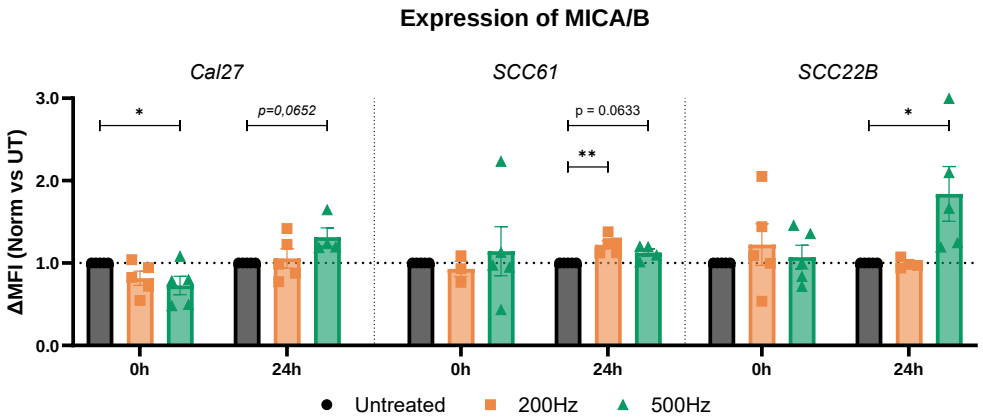

Figure 6-8. CAP stimulates the expression of the activating NK ligand MICA/B 24 h post CAP treatment. HNSCC cell lines were treated with different regimes of CAP, and expression of the MICA/B ligands was analysed with flow cytometry. The amount of MICA/B expression on the cell surface is represented as mean fluorescence intensity minus FMO control, normalised to untreated controls (normalised (Norm) ΔMFI), immediate (0 h) and one day (24 h) post-treatment. Data are represented as mean ± SEM, with individual values shown (n = 5). Statistical significance between untreated cells and the treated conditions was determined using the generalised linear mixed model with post hoc Dunnett's test (* $p \leq 0.05$; ** $p \leq 0.01$). Outliers were calculated with the Grubbs' Test.

Since MICA/B proteins are recognised as stress proteins, induced in tumour cells encountering DNA damage [232], we hypothesised augmentation of ligand expression profile in the different HNSCC cell lines one day post CAP exposure. Indeed, CAP treatment effects mostly manifested in 24 h, with an upregulation of MICA/B on the cellular membrane of all three cell lines compared to untreated controls. Once again, this trend was more pronounced for the higher treatment regimen. Interestingly, the SCC22B cell line, which exhibited the least expressional changes for the inhibitory ligand panel, was strongly positive for MICA/B expression with an 84% increase in ΔMFI compared to baseline (1 vs 1.84; *p = 0.0297*), as displayed in Figure 6-8 (right panel).

4. Discussion

In this chapter, we investigated the effects of CAP on different tumour-associated immune checkpoint ligands for NK cells. We used computational methods to gain insight into the effect of CAP-induced chemical changes on MHC Class I molecules HLA-Cw4 and HLA-E, and how the resulting conformational changes affect biological properties like receptor-ligand binding affinity. Furthermore, we experimentally investigated the oxidation-induced effects of CAP on these cell surface molecules, and broadened our scope to other key immune checkpoints affecting NK cell functioning, providing valuable information for subsequent immunological studies. We distinguished between immediate oxidation effects and downstream cellular responses in the cancer cells. Immediate modifications (0 h analysis) to expression profiles were attributed to oxidation-induced effects, as literature delineates this as the most proficient chemical modification [67, 139, 165, 233]. Besides these transient chemical alterations, the reactive species in CAP cause a cascade of downstream cellular reactions, including metabolic alterations, dysregulation of the anti-oxidant system, and changes in genetic and phenotypic expression profiles (24 h analysis) [62, 222, 234, 235].

Employing MD simulations and umbrella sampling, we aimed to investigate the interaction of MHC-I proteins HLA-Cw4 and HLA-E with their receptors, respectively KIR2DL1 and NKG2A/CD94, and the effect of CAP-induced oxidative changes thereon. The interaction of both is dominated by polar interactions. Several salt bridges were found to be present in our simulations apart from those reported to be present in the crystal structure of the proteins. Notably, for HLA-E, the most prominent salt bridge ($Arg168^{CD94}$ – $Asp68^{HLA\text{-}E}$) is not among those present in the crystal structure, although it was previously indicated to be important in other condensed-phase simulations [236]. Meanwhile, some salt bridges important in the crystal structure were not prominent in our simulations, either due to different interactions taking the upper hand for the participating amino acids ($Asp163^{CD94}$ – $Arg75^{HLA\text{-}E}$), or due to the amino acids simply not interacting much when allowed to move over time ($Arg137^{NKG2A}$ – $Glu154^{HLA\text{-}E}$). In the latter case, indeed, it was found experimentally that prohibiting the formation of this salt bridge through mutation did not affect protein binding [237]. For HLA-Cw4, most salt bridges present in our simulation resulted from promiscuous interactions between the amino acids that form salt bridges in the crystal structure.

Oxidation of the protein ligands did not significantly affect their stability in the simulations. The secondary structure was almost completely retained, and the oxidations did not impact the flexibility of the protein. It has previously been reported that plasma-induced oxidations can affect the protein structure, or even induce partial denaturation. These effects were however mostly observed for (small) proteins with solvent-accessible disulfide bridges [138, 139, 238]. Both MHC-I complexes contain disulfide bridges, important for structural stability, but as these are buried inside the protein, they are unavailable to breakage by CAP-induced oxidation. Although the oxidations do cause the ligands to pivot with respect to their receptor (see Figure 6-3b), the binding domain itself remains nearly unaffected, and the calculated binding free energy of the complexes did not change significantly after oxidation. Indeed, most of the solvent accessible amino acids prone to oxidation in the protein complex were found to be located in the α3 region of both HLA-Cw4 and HLA-E, and in β2M. Furthermore, of the amino acids likely oxidised by plasma treatment that are situated in the binding domain of the complex, none play a direct role in the actual interaction between the HLA proteins and their receptors. In our simulations, we determined which amino acids would be available for oxidation by plasma treatment based on the SASA of the native proteins. While structural changes after oxidation were found to be limited, it is possible that new amino acids are hereby made available to the solvent and thus to oxidations. It may thus be interesting in future simulations to investigate the SASA of the proteins in an iterative way in order to investigate the effects of more substantial protein oxidation. Furthermore, in-depth analysis of the chemical alterations in protein structure using mass spectrometry could be a valuable subsequent step to shed light on these observations, and could potentially unravel additional post-translational modifications (e.g. nitration or nitrosylation).

In accordance with our computational results, we experimentally observed only minor changes in the expression status of HLA-C and HLA-E by CAP oxidation. A significant decrease in the detection of HLA-C directly after treatment was solely observed in the SCC61 cell line (Figure 6-6). In contrast, CAP caused a rapid reduction of the two TIGIT ligands CD155 and CD112, and immune checkpoint CD73 in two out of three tested cell lines (Figure 6-7). It is clear that some immune checkpoints are more vulnerable to therapeutic oxidation, and linking this vulnerability to the structure of these proteins forms an interesting avenue for future computational analysis. Even so, it is essential to recognize some nuances in this context, because the experimental approach of binding a monoclonal antibody for fluorescence staining to the target ligand only partially

approximates the complete ligand-receptor interaction *in vivo*. Indeed, the binding mechanism of the antibody can be [67], but is not necessarily, the same as that of the biological receptor. Still, far-leading structural changes due to (CAP-induced) oxidation would affect the binding to both antibody and receptor.

24 h after CAP application, the ΔMFI of HLA-C and HLA-E remained around baseline (Figure 6-6). The same is true for ligands CD155, CD112, and CD73, indicating that the effects observed immediately after treatment were transient. However, CAP did stimulate the cellular upregulation of the activating NK ligands MICA/B (Figure 6-8). This aligns with previous reports, highlighting MICA/B as important stress proteins in response to cellular imbalance and DNA damage, which are key mechanisms of action of CAP treatment [225, 239]. Moreover, we can conclude that the CAP treatment investigated in this study modulated expression levels rather than the absolute positivity of tumour cells, as indicated by the Overton analysis (see Appendix D). Apart from MICA/B, other stress-induced proteins are also known to contribute to NK cell activation, such as ULBPs [24] and membrane-bound HSP70 [240, 241]. Investigating the effect of CAP treatment on the expression of such stress-induced membrane proteins would further expand our understanding of how CAP can modulate the recognition of cancer cells by NK cells, and forms an interesting candidate for the subject of future research. In addition, deeper exploration of the underlying pathways can be built on the work we presented here. For example, a detailed temporal analysis of ligand expression over a series of time points would provide valuable insights into the kinetic profile and dynamics of the treatment's pleiotropic effects. While oxidative modifications likely play a role in later biological observation as well, it is expected that a complex network of biological mechanisms takes place over time, moving from the immediate chemical character to 24 hours post-treatment, such as protein degradation (e.g., via proteasomal pathways) and alterations in protein trafficking to and from the cell membrane [67, 139, 242]. Furthermore, oxidative stress can trigger signalling pathways that regulate the stability and localisation of membrane proteins. CAP treatment can also modulate gene expression, leading to changes in the synthesis of key proteins that disrupt membrane lipid organisation and impact the localisation of proteins associated with lipid rafts [71, 222].

It is apparent that sensitivity to CAP and the resulting outcome varied between the studied cell lines. While Cal27 and SCC61 were derived from tongue lesions [243, 244], the SCC22B cell line, originated from a metastatic lymph node in the neck [244]. Interestingly, the expression profiles of Cal27 and SCC61 cells clustered together,

whereas the SCC22B cells exhibited a markedly distinct therapeutic response, particularly for the expression of CD112 and CD73. To underline this, we repeated the analysis for CD47, an innate immune cell checkpoint which was previously studied in our lab [67], for the cell lines investigated in the present paper. Indeed, CAP treatment modulated CD47 expression differently across the cell lines (see Appendix D). The fact that different behaviours can be seen immediately after treatment indicates that biological effects beyond purely the chemical protein alterations are at play. Further studies investigating underlying mechanisms (e.g., genetic profile, tumour subsite, disease stage) are necessary to fully elucidate the implications and biological relevance of these observations.

The results presented in this chapter build upon previous work performed in PLASMANT combining experimental and computational methods [67, 139] and broaden our knowledge on crucial aspects of the interaction between CAP, cancer cells, and immune cells. Indeed, our research on the cytotoxic capacities of NK cells following CAP application has previously demonstrated enhanced NK cell-mediated killing in both *in vitro* and *in vivo* melanoma models [70, 71]. The objective of this chapter was to build further on these functional observations, while specifically highlighting the effects of CAP on key tumour cell-NK cell signalling axes. Our results demonstrate a significant impact of CAP application on different inhibitory and activating ligands and pathways, critical for NK cell functioning, but also indicate that these effects are dependent on both the specific protein and cell type. This data corroborates the immunomodulatory potential of CAP. Specifically, it broadens the understanding that CAP not only enhances tumour immunogenicity through the induction of immunogenic cancer cell death [62, 234], but also encompasses the modulation of crucial immune checkpoints within the tumour microenvironment. Hence, the compelling character of the highly reactive yet localised treatment profile of the complex mixture of species in CAP may render it an attractive candidate as a combination partner to bolster existing immune therapies facing critical challenges such as ligand shedding and immune evasion [232, 245, 246]. Nevertheless, further research is needed to fully understand the clinical relevance of the results in this chapter, and to further investigate the effects of CAP on NK cell-mediated cytotoxicity, for both HNSCC as well as other cell lines.

5. Conclusion

Using both *in silico* and *in vitro* methods, in this chapter we investigated the effects of CAP treatment on different tumour-associated immune checkpoint ligands for NK cells. Taken together, our computational results indicate that MHC Class I molecules HLA-Cw4 and HLA-E are not significantly affected by CAP-induced oxidative changes. Although the structure of the ligand-receptor complexes was altered, this did not result in a changed binding strength. Accordingly, we experimentally observed only minor alterations in the expression status of HLA-C and HLA-E, both immediately after treatment and 24 h later. In contrast, CAP caused a rapid reduction of the two TIGIT ligands CD155 and CD112, and immune checkpoint CD73. Meanwhile, the well-known stress proteins and activating NK cell ligands MICA/B were upregulated 24 h after treatment. Taken together, our results demonstrate that CAP affects different ligands important for NK cell functioning, but also that these effects are dependent on both the specific protein and cellular background. Further research is necessary to broaden our understanding of these effects. At the same time, expanding the scope of this combined computational and experimental approach to more immune checkpoints will aid in corroborating the immunomodulatory potential of CAP.

Chapter 7

General conclusions and outlook

In this thesis, we used computational modelling on both macro- and microscopic scales to gain a deeper insight into different aspects of *in vitro* treatment of cancer cells with a plasma jet. Indeed, while *in vivo* research is crucial to progress the field of plasma medicine in a clinical setting, *in vitro* research still lies at the basis of understanding the possible effects of plasma treatment on cells. In turn, modelling can provide fundamental insight into underlying mechanisms that are out of reach with experimental methods. To investigate transport phenomena that occur during treatment of a well plate with a plasma jet on the macroscopic scale, we developed a computational 2D-axisymmetric fluid model, and applied this model to study examples where a lack of uniformity in plasma medicine research, both experimental and computational, hinders the direct comparison of results. Furthermore, to investigate the biological effects of CAP treatment on a microscopic scale, we used MD modelling, with a focus on the immunotherapeutic potential of CAP.

In the first section of this chapter, we will summarize the conclusions that can be drawn from the research presented in this thesis. Afterwards, we will provide a personal outlook on the future of this research field.

1. General conclusions

The computational fluid model developed for this thesis, which was used for much of the research in the subsequent chapters, was presented in **Chapter 2**. By comparing results from the model to experimental data published in literature, we were able to gain confidence that the model can accurately describe fluid flow, heat transfer and transport of chemical species throughout the simulated system and can provide insight into yet unknown aspects of the system.

In **Chapter 3**, we applied our model to investigate the influence of the geometry of the treatment setup, more specifically the chosen well type and the use of a shielding gas around the plasma jet. We focussed on the mixing of the plasma jet effluent with the ambient N_2, O_2 and H_2O, as these molecules drive RONS formation in the plasma, i.e. the main effectors of CAP treatment. The results suggest that caution must be taken when comparing results obtained with different setup geometries, even if the operating parameters are the same. Indeed, the chosen well size will determine the flow field of the gas and influence how much of the ambient is able to mix with the jet effluent in the well. At the same time, the backflow induced by the well causes a self-shielding effect, eliminating the influence of different ambient humidities. The ambient temperature does still influence the amount of H_2O that is able to mix with the effluent, as it affects the evaporation of the treated liquid.

Using a gas shield can negate the effect caused by different well sizes, by controlling the environment that mixes with the jet effluent (though evaporated water from the treated well still plays a role). However, caution is still necessary. First, the amount of gas that mixes with the plasma effluent changes when a gas shield is used. This is especially important when comparing diagnostics in the presence of a gas shield to experiments without a gas shield, as they do not entail the same (quantitative) conditions in the active plasma zone. Second, depending on the well size, the gas shield may not perform as intended, and even cause unintended effects on the neighbouring wells.

The results in **Chapter 4** further emphasize that a lack of uniformity in the treatment setups of different experimental works may complicate comparing their results. In a systematic study on the design of the shielding gas device, we found that this choice substantially affects both the conditions in the effluent and its efficacy in shielding the effluent from the ambient. The largest effect was seen for the radial position of the

shielding gas nozzle, while minor effects (but effects nonetheless) were found for its axial position and width, as well as the flow direction of the shielding gas.

Chapter 5 makes it clear that a lack in uniformity can not only arise in experimental work, but also in computational models, and can be detrimental to comparability and accuracy. By comparing computational results to experimental data, we showed that none of the tested interfacial boundary conditions that describe dissolution of RONS into a treated liquid, as used in various published multidimensional plasma-liquid models, are able to reproduce experimental measurements for all species. Specifically, we found that agreement is easily reached for highly soluble species like H_2O_2, but dissolution is severely overestimated for species with a lower solubility such as O_3, ·NO and HNO_2. Consequently, we proposed a first step toward a more accurate description of this phenomenon by combining film theory with the mass accommodation coefficient.

Finally, in **Chapter 6**, we used molecular dynamics simulations to investigate the effect of CAP-induced oxidation on HLA-E and HLA-Cw4, two protein ligands that are important for the crosstalk between cancer cells and NK cells. The computational results revealed that, while the oxidations caused conformational changes in the simulated complexes, their binding affinity was not affected. The latter could also be deduced from experiments. Nevertheless, the experiments did predict CAP-induced changes on a range of other NK cell ligands. This demonstrates the complex chemical and biological interactions between CAP and cancer cells, with regard to NK cell recognition, and provides an interesting starting point for further research. Taken together, the results in this chapter demonstrate that CAP can affect different ligands important for NK cell functioning, but also that these effects are dependent on both the specific protein and cellular background.

2. Outlook

This final section will provide a personal outlook on the future of the field, rooted in the results presented in this thesis. We will split our view over *(i)* the importance of standardisation to progress the field, *(ii)* the future of fluid modelling to understand treatment with a plasma jet, and *(iii)* the immunotherapeutic potential of CAP treatment and the role of MD simulations.

The importance of standardisation to progress plasma oncology

Although much research has been performed in both plasma oncology and related fields, the use of CAP in cancer treatment is still in the early stages of development. Much more research, especially *in vivo* is needed for the application to establish itself clinically. On the other hand, *in vitro* research will likely remain crucial to provide a basic understanding of the possible effects of CAP on treated cells. In turn, to understand these possible effects *in vitro*, more standardization is necessary, or at the very least a deep understanding of the various parameters that influence the treatment. Indeed, while experimentation remains important to find new research avenues and treatment strategies, the need for more standardisation is becoming increasingly recognised [36, 82]. This applies to both treatment setups and conditions, as well as CAP devices used in research.

We saw in Chapter 3 that even the choice of the treated well size can influence the conditions in the effluent of a plasma jet and, by extension, the treatment. It is highly unlikely that this finding will cause the entire field to start using only a single well type, starting now. It is, however, important to keep this effect in mind as a source of variation in experiments, along with other determining parameters, both when conducting and when comparing experiments.

To eliminate this variation caused by the chosen well plate, in addition to variation caused by the surrounding atmosphere, using a gas shield is considered a straightforward solution. As became clear from Chapter 4, however, a standardised design of the shielding gas device would clearly be beneficial here. From the effects of the four geometrical parameters that we investigated, we can distil a general recommendation. Most importantly, the radial distance between the plasma jet nozzle and the gas shield nozzle should be small enough to prevent the development of a recirculation zone, while the axial position gave the best results when (slightly) below that of the jet nozzle. While a broader width of the gas shield results in better shielding,

this also causes a severe effect of the backflow from the treated well. Therefore, a smaller width will in most cases be the better choice for *in vitro* treatment. Finally, an important result from Chapter 3 was that one must take caution when comparing plasma jet diagnostics in the presence of a gas shield to experiments without a gas shield, as they have different conditions in the active plasma zone. We can, however, see from the results in Chapter 4 that this comparability improves (though a difference remains, especially when treating a well) when the shielding gas is directed towards the plasma effluent, compared to having a parallel flow direction. Interestingly enough, this description pretty much leads us to the original design of the gas shield reported by Reuter *et al*. in 2012 [108]. This once again underlines the importance of critical comparison between methods.

It is important to note that it remains to be seen how important the variation caused by different ambient conditions actually are in an *in vivo* setting. In addition, as mentioned in Chapter 3, a second approach to reduce variation is to add admixtures to the feed gas. Indeed, admixed species play a larger role compared to ambient species that mix with the plasma effluent [159]. Humidifying the feed gas would likely also decrease effects from evaporated water from the treated well. Still, admixtures will change the discharge itself, while most experimental research with the kINPen has been performed using pure Ar as the feed gas, leading again to reduced comparability.

The future of modelling in vitro treatment with a plasma jet

While computational modelling represents only a minor part of plasma medicine research, simulations can offer important insights that are not feasible to obtain experimentally. So far, multidimensional modelling studies (mostly in 2D) have mostly chosen one of two approaches: either *(i)* the discharge and resulting plasma chemistry is taken into account, but the model is solved for only a very short time, or *(ii)* transport of species throughout the simulated system is simulated on longer timescales, but the plasma chemistry itself is not resolved. In the latter, limited (neutral) reaction sets have been included, while RONS were introduced into the system with concentrations based on either literature or 0D modelling.

For the fluid model developed in this thesis, we took the second approach. Our goal was to reach a more accurate description of the physical phenomena in the system, compared to previous models developed within PLASMANT. The results of this were outlined in Chapter 2. Meanwhile, our research focus was on the transport phenomena that determine both mixing of the jet effluent with the surrounding atmosphere

(Chapters 3 and 4), and the transport and accumulation of RONS into the treated liquid (Chapter 5). To progress the modelling of this system, the challenge remains to merge the two approaches above, to be able to evaluate the transport of RONS throughout the system based on the full, multidimensional description of the plasma discharge.

A second challenge is the accurate description of dissolution of various RONS into the treated liquid. Chapter 5 clearly illustrates the importance of benchmarking a model that describes plasma-liquid interaction against data for species with different solubilities. Although we proposed a first step toward a more accurate description of the dissolution process in a fluid model, the limited and variable data that is available in literature on the used mass accommodation coefficient may remain an obstacle in reaching a robust description of the dissolution process. A general recommendation based on the results in Chapter 5, is to implement the boundary condition as presented at the end of this chapter (equation E.5-7) into future models, and to use a mass accommodation coefficient α_b of 0.05 for species where data is unavailable. Indeed, we saw that species with a high solubility are unaffected by the use of α_b, while for species with a low solubility this value prevents a large overestimation of the dissolution. Using this value will of course still be an approximation, but we believe that this will still provide more realistic results compared to not using α_b at all.

In any case, more research is needed to investigate this aspect of plasma-liquid modelling. Furthermore, investigating the use of more sophisticated models that have been developed since film theory may lead to more accurate descriptions still.

The immunotherapeutic potential of CAP and the role of MD modelling

If the use of CAP in cancer treatment is still in the early stages of development, then the exploration of the immunotherapeutic effects of CAP treatment is at an even earlier stage. Still, results are promising, both in its ability to induce immunogenic cell death and its effects on immune proteins. In Chapter 6, we saw that CAP affects the expression of several immune checkpoint ligands for NK cells, on both a short and longer timescale. In the experiments, we chose the two investigated timepoints to distinguish between immediate chemical effects (0 h analysis) and downstream biological effects (24 h analysis) of the treatment. It is clear, however, that this hypothesis needs to be adjusted. The fact that the immediate effects depend on the treated cell type, suggests that other effects apart from the purely chemical modification of membrane proteins are at play. Deeper insights are necessary here and can be gained through more detailed analysis over a series of time points, of not only the effect of CAP on ligand expression but also

on underlying mechanisms that lead to expression, such as gene transcription. In addition, investigating the effects on other immunological proteins would further expand our understanding of how CAP can modulate the recognition of cancer cells by NK cells, and forms an interesting subject for future research. Interesting examples are a wider range of stress-induced proteins, such as ULBPs [24] and membrane-bound HSP70 [240, 241], or established immunological targets such as the PD-1/PD-L1 axis.

It remains to be seen what the clinical relevance of the effects of CAP on immune ligands will be, insight which can only be gained by rigorous *in vivo* research and assessment of the actual effects on immune cells. Still, fundamental understanding of the effects CAP on these proteins remains important. For this purpose, MD simulations are a valuable tool, as presented in Chapter 6. However, two limitations have held back these simulations so far, that present challenges for future research.

First, MD simulations of proteins have been limited by their very long calculation times. This has limited not only the range of proteins that have been investigated so far, but also the number of replicate simulations that have been performed per protein. Many of the MD simulations in plasma medicine have simulated only a single replicate. The simulation results of these studies can thus only be considered as indicative. Recently, some studies have investigated up to four replicates, including our own (Chapter 6) which included three replicates. However, even three replicates were shown by Knapp *et al*. [247] to be insufficient for investigating the true average behaviour of protein systems, and this should be investigated more deeply to increase our confidence in the reliability of the simulation results. Within PLASMANT, this matter is being addressed by testing the increased parallelization, made possible by offloading parts of the MD simulations onto recent, powerful GPUs.

Second, the oxidative changes implemented into simulated proteins, to investigate the effect of CAP treatment, have so far been based mostly on approximate methods to determine the post-translational modifications induced by CAP treatment. These include the treatment of individual amino acids or short peptides, while it is known that in a complete protein the surrounding amino acids can significantly influence the induced oxidations. More accurate methods of investigating the chemical changes induced by plasma treatment, such as mass spectrometry of complete proteins, offer a clear path to improve MD simulations and enhance our understanding of how CAP can affect proteins and, by extension, the immune response against cancer cells.

3. Final conclusion

Altogether, the findings presented in this thesis have provided a deeper insight into the *in vitro* treatment of cancer cells with a plasma jet on both a macroscopic and microscopic scale. We investigated various ways in which the chosen setup geometry can influence the treatment itself. It is important to keep these effects in mind as a source of variation in experiments, along with other determining parameters, both when conducting experiments and when comparing them among each other. Moreover, the importance of benchmarking and comparison between computational results was highlighted. Finally, we shed some light onto the immunotherapeutic potential of CAP treatment, and pointed toward possible paths for future research.

Appendix

A. Further details on the 2D model

A.1 Turbulence model equations and parameters

The turbulent kinetic energy source term P, as used in the transport equation for turbulent kinetic energy, is calculated in the SST turbulence model as [145]:

$$P = \min(P_k, 10\rho\beta_0^* k\omega) \qquad \text{with } P_k = \mu_t\left(\nabla\vec{u} : (\nabla\vec{u} + (\nabla\vec{u})^T)\right)$$

The characteristic magnitude of the mean velocity gradients S is calculated as

$$S = \sqrt{2\boldsymbol{S}:\boldsymbol{S}}$$

with **S** the strain-rate tensor, defined as:

$$\mathbf{S} = \frac{1}{2}(\nabla\vec{u} + (\nabla\vec{u})^T)$$

The blending functions f_{v1} and f_{v2} that are used in both the transport equation for the specific dissipation rate and in the calculation of the turbulent dynamic viscosity are defined as follows:

$$f_{v1} = \tanh\left(\left(min\left[max\left[\frac{\sqrt{k}}{\beta_0^*\omega y}, \frac{500\mu}{\rho\omega y^2}\right], \frac{4\rho\sigma_{\omega 2}k}{CD_{k\omega}y^2}\right]\right)^4\right)$$

$$f_{v2} = \tanh\left(\left(max\left(\frac{2\sqrt{k}}{\beta_0^*\omega y}, \frac{500\mu}{\rho\omega y^2}\right)\right)^2\right)$$

With $CD_{k\omega} = max\left(\frac{2\rho\sigma_{\omega 2}}{\omega}\nabla\omega\cdot\nabla k, 10^{-10}\right)$ and y the distance to the nearest wall. Blending function f_{v1} is additionally used for the calculation of the turbulence modelling parameters β, γ, σ_k and σ_ω (each generally represented in the formula below as "α") as follows:

$$\alpha = \alpha_1 f_{v1} + \alpha_2(1 - f_{v1})$$

The constants $\alpha_{1,2}$, as well as the turbulence modelling constants β_0^* and a_1 are given in Table A-1.

Table A-1. Constants used in the SST turbulence model.

Constant	value
$\boldsymbol{\beta_1}$	3/40
$\boldsymbol{\beta_2}$	0.0828
$\boldsymbol{\gamma_1}$	5/9
$\boldsymbol{\gamma_2}$	0.44
$\boldsymbol{\sigma_{k,1}}$	0.85
$\boldsymbol{\sigma_{k,2}}$	1.0
$\boldsymbol{\sigma_{\omega,1}}$	0.5
$\boldsymbol{\sigma_{\omega,2}}$	0.856
$\boldsymbol{\beta_0^*}$	0.09
$\boldsymbol{a_1}$	0.31

A.2 Temperature and species transport

A.2.1 Species-specific parameters

The binary diffusion coefficients that are used to calculate the mixture-averaged diffusion coefficients in the gas phase are calculated using the following formula [147, 148, 248]:

$$D_{ij} = 2.6628 \cdot 10^{-22} \sqrt{\frac{T^3}{2 \cdot 10^3} \frac{\left(M_i + M_j\right)}{\left(M_i M_j\right)}} \cdot \frac{1}{p \sigma_i \sigma_j \Omega_{D,ij}}$$

Where $\Omega_{D,ij}$ is a dimensionless quantity called the collision integral for diffusion. It is calculated using the empirical formula:

$$\Omega_D = \frac{c_1}{(T^*)^{c_2}} + \frac{c_3}{e^{c_4 T^*}} + \frac{c_5}{e^{c_6 T^*}} + \frac{c_7}{e^{c_8 T^*}} \qquad with\ T^* = T \frac{k_B}{\sqrt{\varepsilon_i \varepsilon_j}}$$

Here, $c_{1\text{-}8}$ are empirical constants, and k_B is the Boltzmann constant. σ_i and ε_i are, respectively, the characteristic length (m) and the potential energy minimum for the Lennard-Jones potential of species i. They are specified for each species that is present in the model throughout this thesis in Table A-2.

Table A-2. Lennard-Jones parameters of the species present in the model throughout this thesis, as used for calculation of the binary diffusion constants. (1) Due to a lack of data, the same coefficients were used here as for H_2O_2 as an approximation.

Species	L-J parameters		Ref.
	σ (m)	**$\frac{\varepsilon}{k_B}$ (K)**	
Ar	3.33×10^{-10}	136.5	[249]
He	2.576×10^{-10}	10.2	[249]
N_2	3.621×10^{-10}	97.53	[249]
O_2	3.458×10^{-10}	107.4	[249]
H_2O	2.605×10^{-10}	572.4	[249]
H_2O_2	3.458×10^{-10}	107.4	[249]
O_3	3.875×10^{-10}	208.4	[250]
NO	3.621×10^{-10}	97.53	[249]
HNO_2	3.458×10^{-10}	107.4	(1)

The heat capacity of the mixture in the gas phase is calculated using the individual heat capacities of the present species:

$$C_p = \sum_i \omega_i \frac{C_{p,i}}{M_i}$$

These can be calculated using the 7-term NASA polynomials (these are sufficient to calculate C_p at the temperatures where our model is applied, compared to the more recent 9-term polynomials [251]) [252]:

$$C_p = R(a_1 + a_2 T + a_3 T^2 + a_4 T^3 + a_5 T^4)$$

With R the ideal gas constant. The polynomial coefficients $a_{1\text{-}5}$ are provided for each species used in our model in Table A-3. Using the heat capacities, we additionally calculate the individual thermal conductivities [148, 253]:

$$\kappa_i = \frac{\mu_i}{M_i}\left(1.15 C_{p,i} + 0.88R\right)$$

Which are then used to determine the thermal conductivity of the mixture in the gas phase:

$$\kappa = \frac{1}{2}\left(\sum_i x_i k_i + \frac{1}{\sum_i \frac{x_i}{k_i}}\right)$$

Table A-3. Polynomial coefficients of the species present in the model throughout this thesis, as used for calculation of their heat capacity. The coefficients shown are those valid between 200 K and 1000 K. For more complete data (at higher temperatures, as well as the sixth and seventh polynomial coefficient), see the respective sources. (1) Due to a lack of data, the same coefficients were used here as for H_2O_2 as an approximation.

Species	Polynomial coefficients					Ref.
	a_1	a_2 (× 10^{-3} 1/K)	a_3 (× 10^{-5} 1/K^2)	a_4 (× 10^{-8} 1/K^3)	a_5 (× 10^{-12} 1/K^4)	
Ar	2.5	0	0	0	0	[249]
He	2.5	0	0	0	0	[252]
N_2	3.298677	1.4082404	-0.3963222	0.5641515	-2.444854	[249]
O_2	3.78245636	-2.99673416	0.984730201	-0.968129509	3.24372837	[249]
H_2O	4.19864056	-2.0364341	0.652040211	-0.548797062	1.77197817	[249]
H_2O_2	4.27611269	-0.542822417	1.67335701	-2.15770813	8.62454363	[249]
O_3	3.40738221	2.05379063	1.38486052	-2.23311542	9.76073226	[252]
NO	4.2184763	-4.638976	1.1041022	-9.3361354	2.803577	[249]
HNO_2	4.27611269	-0.542822417	1.67335701	-2.15770813	8.62454363	(1)

A.2.2 Accounting for turbulence

To account for turbulent heat transport, a turbulent thermal conductivity is used that is calculated using the turbulent Prandtl number Pr_T. In turn, Pr_T is calculated as follows [146, 254]:

$$Pr_T = \left(\frac{1}{2Pr_{T\infty}} + \frac{0.3}{\sqrt{Pr_{T\infty}}} \frac{C_p \mu_T}{k} - \left(0.3 \frac{C_p \mu_T}{k}\right)^2 \left(1 - e^{-\frac{k}{0.3 C_p \mu_T \sqrt{Pr_{T\infty}}}}\right) \right)^{-1}$$

Similarly, the turbulent diffusivity used to account for turbulent mass transport is calculated using the turbulent Schmidt number Sc_T, which is calculated by COMSOL by assuming that the turbulent transport of heat and mass behave analogously:

$$Sc_T = \left(\frac{1}{2Sc_{T\infty}} + \frac{0.3}{\sqrt{Sc_{T\infty}}} \frac{\mu_T}{\rho D_{m,i}} - \left(0.3 \frac{\mu_T}{\rho D_{m,i}}\right)^2 \left(1 - e^{-\frac{\rho D_{m,i}}{0.3 \mu_T \sqrt{Sc_{T\infty}}}}\right) \right)^{-1}$$

Both the turbulent Prandtl number at infinity $Pr_{T\infty}$ and the turbulent Schmidt number at infinity $Sc_{T\infty}$ are equal 0.85.

A.2.3 Transport data in the liquid phase

In the liquid phase of our model, we assume that the whole phase has the properties of the solvent (water) and that these properties are not affected by the dilute solutes that enter the phase through the gas-liquid interphase. These properties were adopted from the built-in material library in COMSOL [140], and are consequently calculated as follows:

The dynamic viscosity (valid between 273.15 K and 413.15 K):

$$\begin{aligned} \mu_{H_2O} = {} & 1.3799566804 - 0.021224019151 \cdot T + 1.3604562827 \cdot 10^{-4} \cdot T^2 \\ & - 4.6454090319 \cdot 10^{-7} \cdot T^3 + 8.9042735735 \cdot 10^{-10} \cdot T^4 \\ & - 9.0790692686 \cdot 10^{-13} \cdot T^5 + 3.8457331488 \cdot 10^{-16} \cdot T^6 \end{aligned}$$

Which gives, at 293.15 K, a dynamic viscosity of 1.0094 × 10^{-3} Pa·s.

The heat capacity (valid between 273.15 K and 553.15 K):

$$\begin{aligned} C_{p\ H_2O} = {} & 12010.1471 - 80.4072879 \cdot T + 0.309866854 \cdot T^2 \\ & -5.38186884 \cdot 10^{-4} \cdot T^3 + 3.62536437 \cdot 10^{-7} \cdot T^4 \end{aligned}$$

The density (valid between 273.15 K and 373.15 K):

$$\rho_{H_2O}\,(T < 293.15\,K) = 0.000063092789034 \cdot T^3 - 0.060367639882855 \cdot T^2 + 18.9229382407066 \cdot T - 950.704055329848$$

$$\rho_{H_2O}\,(T > 293.15\,K) = 0.000010335053319 \cdot T^3 - 0.013395065634452 \cdot T^2 + 4.969288832655160 \cdot T - 432.257114008512$$

The thermal conductivity (valid between 273.15 K and 553.15 K):

$$\kappa_{H_2O} = -0.869083936 + 0.00894880345 \cdot T - 1.58366345 \cdot 10^{-5} \cdot T^2 + 7.97543259 \cdot 10^{-9} \cdot T^3$$

For the species that are present in the liquid phase, diffusive transport is described by Fick's law. The diffusion coefficients are listed in Table A-4.

Table A-4. Fickian diffusion coefficients of the species present in the liquid phase of the model throughout this thesis. (1) Due to a lack of data, approximative diffusion coefficients were used (i.e. the order of magnitude of the known coefficients).

Species	D_l (m²/s)	Ref.
N_2	2.6×10^{-9}	[255]
O_2	2.3×10^{-9}	[255]
H_2O_2	1.7×10^{-9}	[124]
O_3	1.76×10^{-9}	[256]
NO	2.2×10^{-9}	[257]
HNO_2	2.5×10^{-9}	[124]
NO_2	1.85×10^{-9}	[124]
NO_2^-	1.85×10^{-9}	[124]
H^+	7×10^{-9}	[124]
CPTIO	1×10^{-9}	(1)
CPTI	1×10^{-9}	(1)
$CPTIO^+$	1×10^{-9}	(1)

B. Supplementary figures for model benchmarking

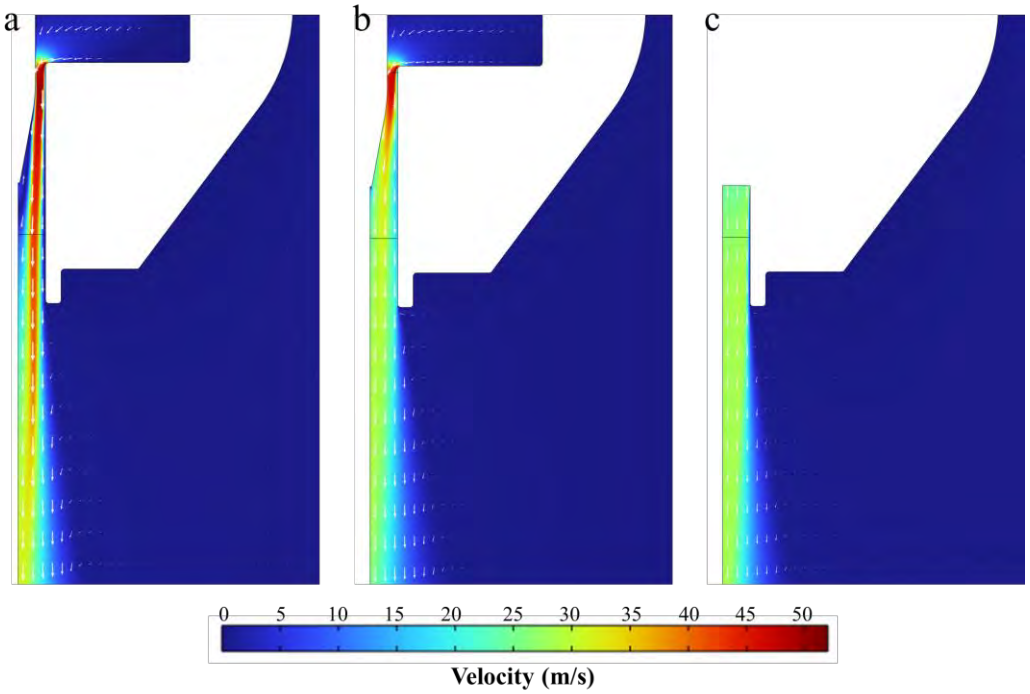

Figure B-1. Flow field in the jet (flow rate of 3 SLM) as calculated (a) using the SST turbulence model, compared to (b) using the k-ε turbulence model. Comparison is also shown to (c) using the SST turbulence model but ignoring the internal structure of the jet, which is done in some published models, but is shown here to have a significant effect.

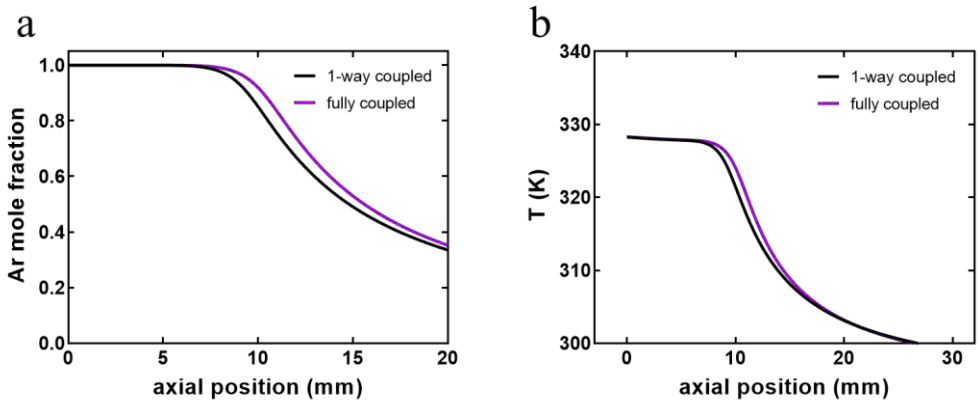

Figure B-2. Model results when the stationary solution of the flow field is used as input for the time-dependent simulation of the heat transfer and species transport in the system (1-way coupled approach), compared to the results when calculating the flow field as a function of time together with the transport of heat and chemical species (fully coupled approach). The comparison is made for (a) the Ar mole fraction and (b) the gas temperature, both as a function of distance from the jet nozzle. The results show that the 1-way coupled approach is, for the system modelled here, a good approximation, with the benefit of much faster calculation.

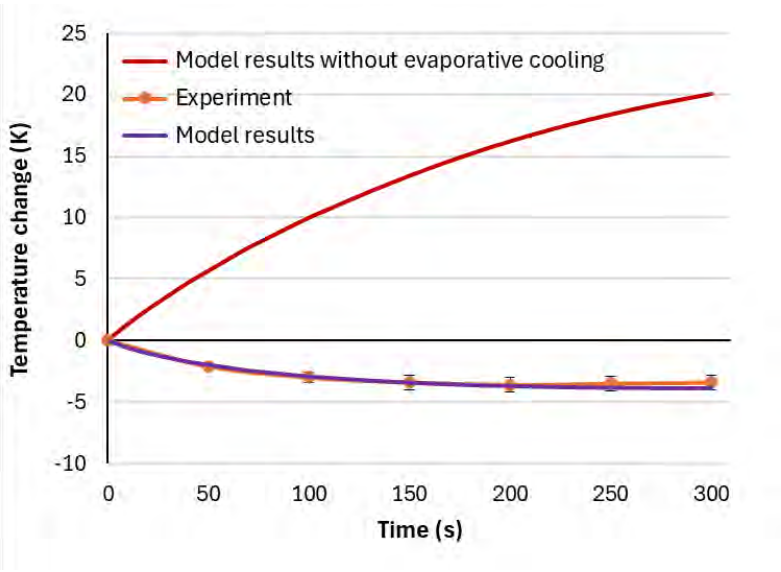

Figure B-3. Temperature of the treated liquid (2 mL in a 12-well plate, a gas flow of 3 SLM and a treatment gap of 3 cm) as measured experimentally and as calculated by the model. Comparison is shown with the model when evaporative cooling is ignored, showing clearly that it is important to account for this phenomenon even if the temperature decrease appears limited.

C. Supplementary information for Chapters 3 and 4

C.1 The difference between model versions

While the final version of the computational 2D-axisymmetric fluid model developed for this thesis, as presented in Chapter 2, was constructed in COMSOL version 6.2, the research in Chapters 3 and 4 was performed with a previous version of the model, built in COMSOL version 6.0. The 6.2 model was improved over the 6.0 model in several ways. Most relevant for the results in Chapters 3 and 4 is that the 6.0 model leads to a larger overestimation of the distance from the jet nozzle where the jet effluent starts mixing significantly with the surrounding gas. This is illustrated in Figure C-1a and b for the Ar mole fraction and gas temperature. In addition, Figure C-1d and f show how the model results, for the density of N_2 and H_2O as calculated with the 6.2 model, compare to the results of the 6.0 model shown previously in Figures 3-2a and 3-3a for the jet without gas shield above a 24-wellplate (repeated here in Figure C-1c and e for convenience). Indeed, we see that the mixing behaviour is shifted closer to the jet nozzle, with larger differences for the centre of the effluent.

In practice, while the 6.2 model agrees better with experimental data (cf. Chapter 2) and thus describes the simulated system more accurately, the differences between both model versions do not affect the conclusions drawn in Chapters 3 and 4. The differences between the mixing behaviour calculated using the 6.0 model and the 6.2 model are purely quantitative, while both in Chapter 3 and Chapter 4 our focus was on differences between various setup geometries. Indeed, for some cases we repeated our simulations with the 6.2 model and found the same conclusions.

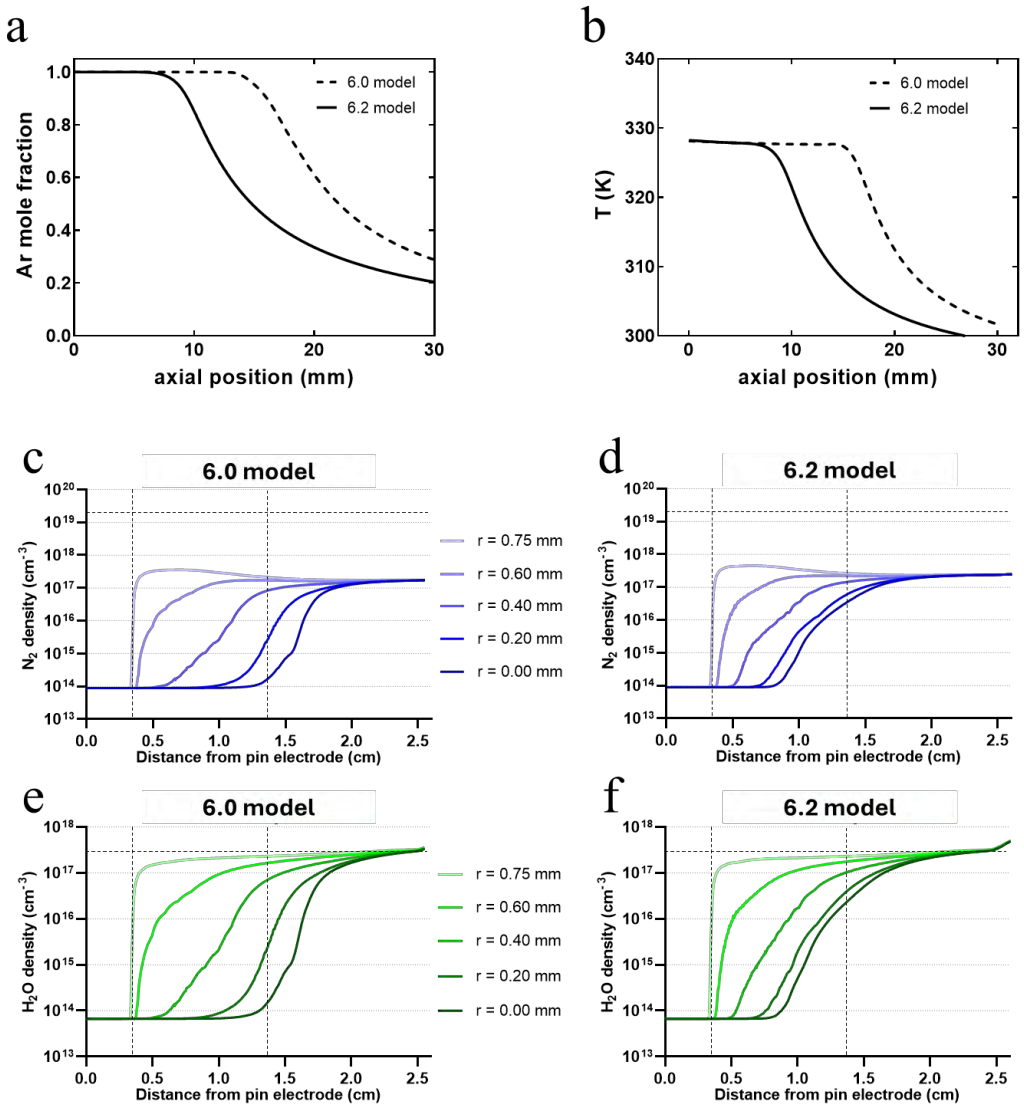

Figure C-1. Comparison of the computational model built in COMSOL 6.0 with that in COMSOL 6.2. Comparison is made for (a) the calculated Ar mole fraction and (b) the gas temperature, both as function of the distance from the jet nozzle. In addition, the N_2 density (c, d) and H_2O density (e, f) in the jet effluent are compared. In all cases, we see that the 6.0 model predicts a larger axial distance at which the feed gas starts mixing with the surrounding gas. This leads to a worse agreement with experimental data. Still, the differences are purely quantitative and thus do not compromise the conclusions that were drawn with the 6.0 model.

C.2 A closer look at the gas shield vortex

We found that the culprit for the bad gas shield performance, when the gas shield nozzle is at a large radial distance compared to the jet nozzle, is the development of a vortex in the flow field between these two nozzles. In this section, we will take a closer look at what drives the mixing in this vortex.

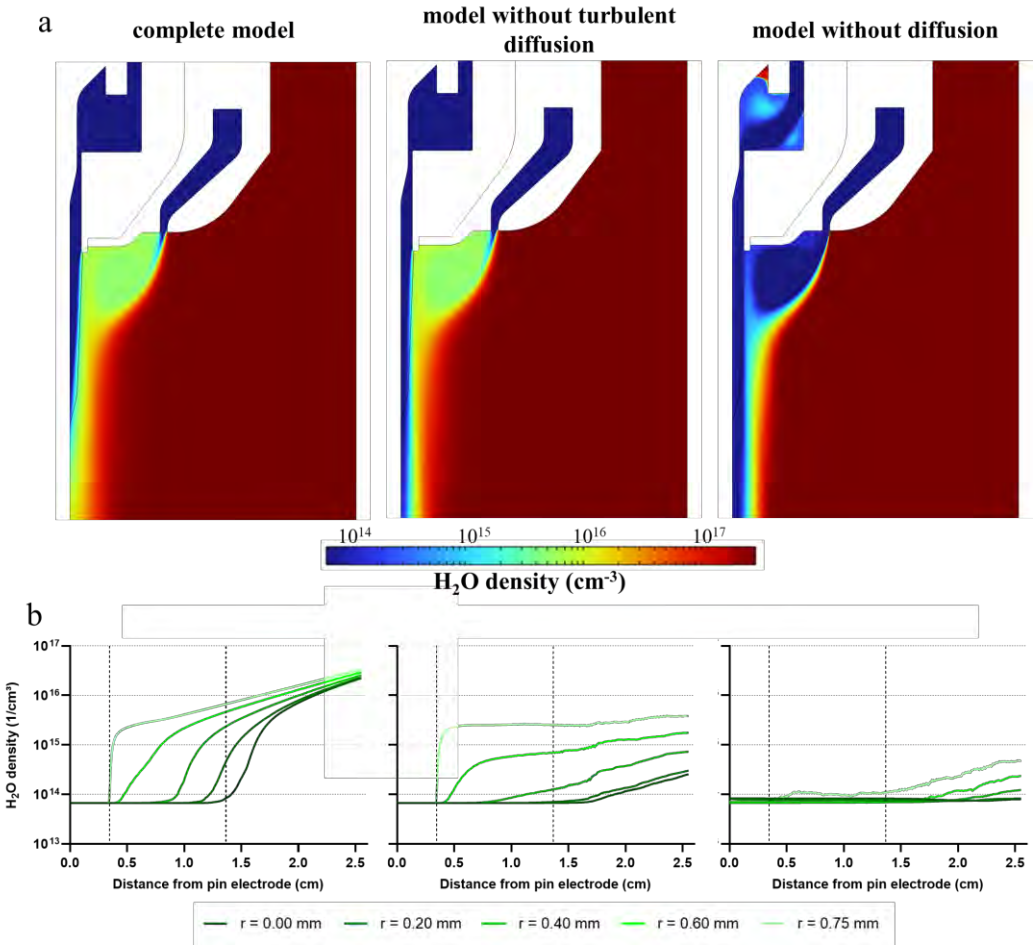

Figure C-2. Model results compared to when either turbulent diffusion or diffusive transport as a whole are not accounted for. (a) The H_2O density in the system. (b) The H_2O density as a function of distance from the pin electrode, for different radial positions. The comparison shows that while normal diffusive transport is responsible for the entrainment of ambient gas into the vortex, turbulence is the main driver for transport of this gas into the jet effluent.

The vortex effectively “pulls in” species towards the jet effluent. In other words, ambient gas is entrained in the vortex, which in turn facilitates the mixing of this gas with the jet effluent. This mixing can happen either through diffusion, perpendicular to the flow direction, or through turbulence (the effect of which is modelled via a so-called turbulent diffusivity, cf. Chapter 2). To investigate the contribution of both transport phenomena, we performed simulations where either turbulent diffusion was not accounted for, or diffusive transport was turned off completely (done in practice by setting all diffusion constants to an extremely low value). The results are shown in Figure C-2.

The results show that when turbulent diffusion is not accounted for, the conditions in the vortex are unchanged. However, mixing of gas with the jet effluent is significantly reduced, especially in the centre of the effluent. Meanwhile, when neglecting diffusive transport as a whole, no ambient H_2O is entrained into the vortex, and the effluent of the jet stays free of ambient gas. This indicates that while normal diffusive transport is responsible for the entrainment of ambient gas into the vortex between the jet nozzle and gas shield nozzle, diffusive transport towards the jet effluent (i.e. into the discharge region) is too weak compared to the strong convective flux to induce much mixing. Instead, the mixing of ambient gas into the jet effluent is mostly driven by turbulent diffusion.

D. Supplementary data for Chapter 6

D.1 Computational data

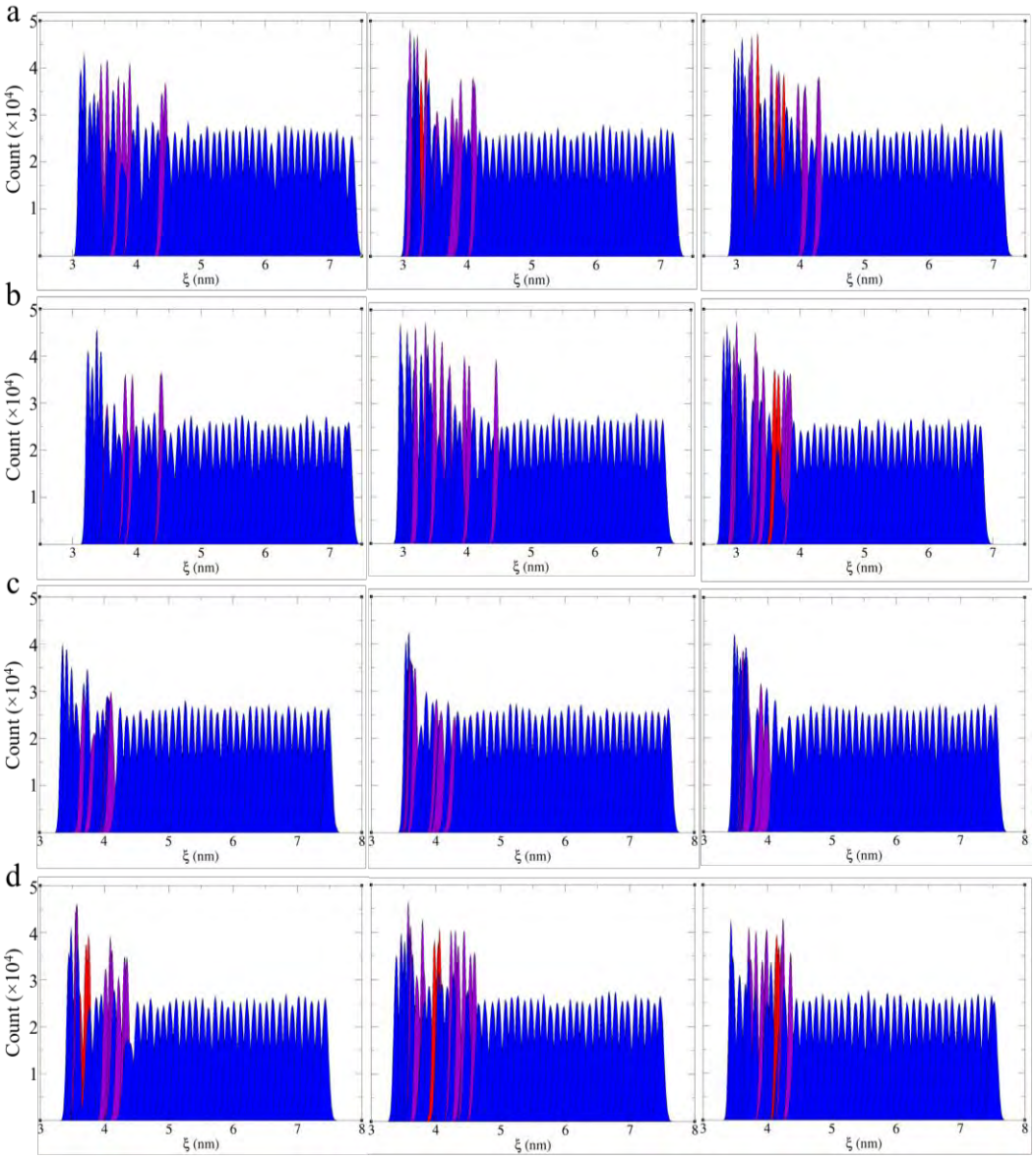

Figure D-1. Histograms of the umbrella sampling simulations, along the reaction coordinate ξ of the pulling simulations, for (a) native and (b) oxidized NKG2A/CD94 – HLA-E, and (c) native and (d) oxidized KIR2DL1 – HLA-Cw4. Blue histograms represent the initial 40 simulated windows, while purple and red histograms are those of the additional sampling simulations.

D.2 Experimental data

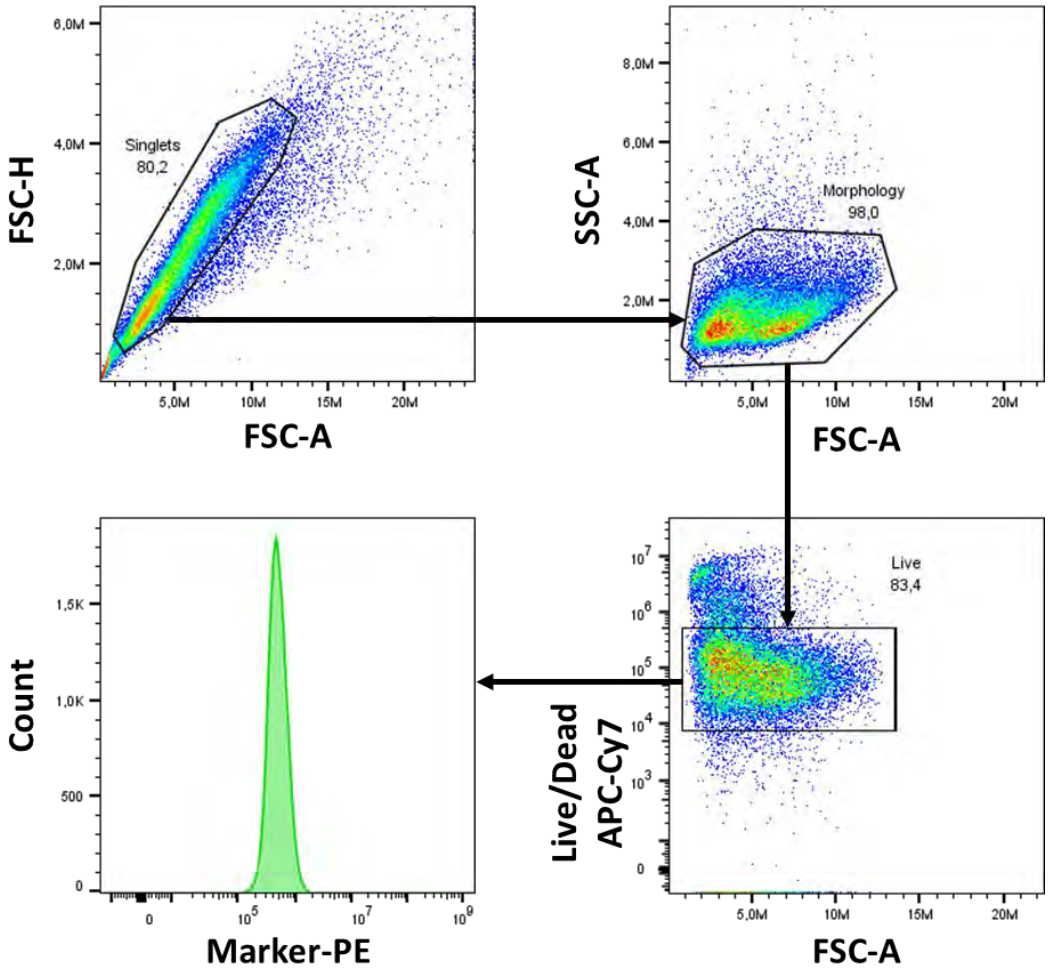

Figure D-2. Flow cytometry plots of untreated Cal27 HNSCC cells, representing the gating strategy of all treatment conditions and cell lines throughout the experiment. HNSCC cell lines (Cal27, SCC61, and SCC22B) were stained for the target (anti-HLA-C, anti-HLA-E, anti-CD155, anti-CD122, anti-CD73, or anti-MICA/B) in the PE channel, and counterstained with a live-dead stain (LIVE/DEAD™ Fixable Near-IR, APC-Cy7). A single cell population was obtained by doublet removal in the forward scatter height and area (FSC-H vs FSC-A) plot, whereafter singlets were gated on morphology in the forward and side scatter area (FSC-A vs SCC-A) plot. Expression of the target-PE was determined in the APC-Cy7$^-$ live cell population.

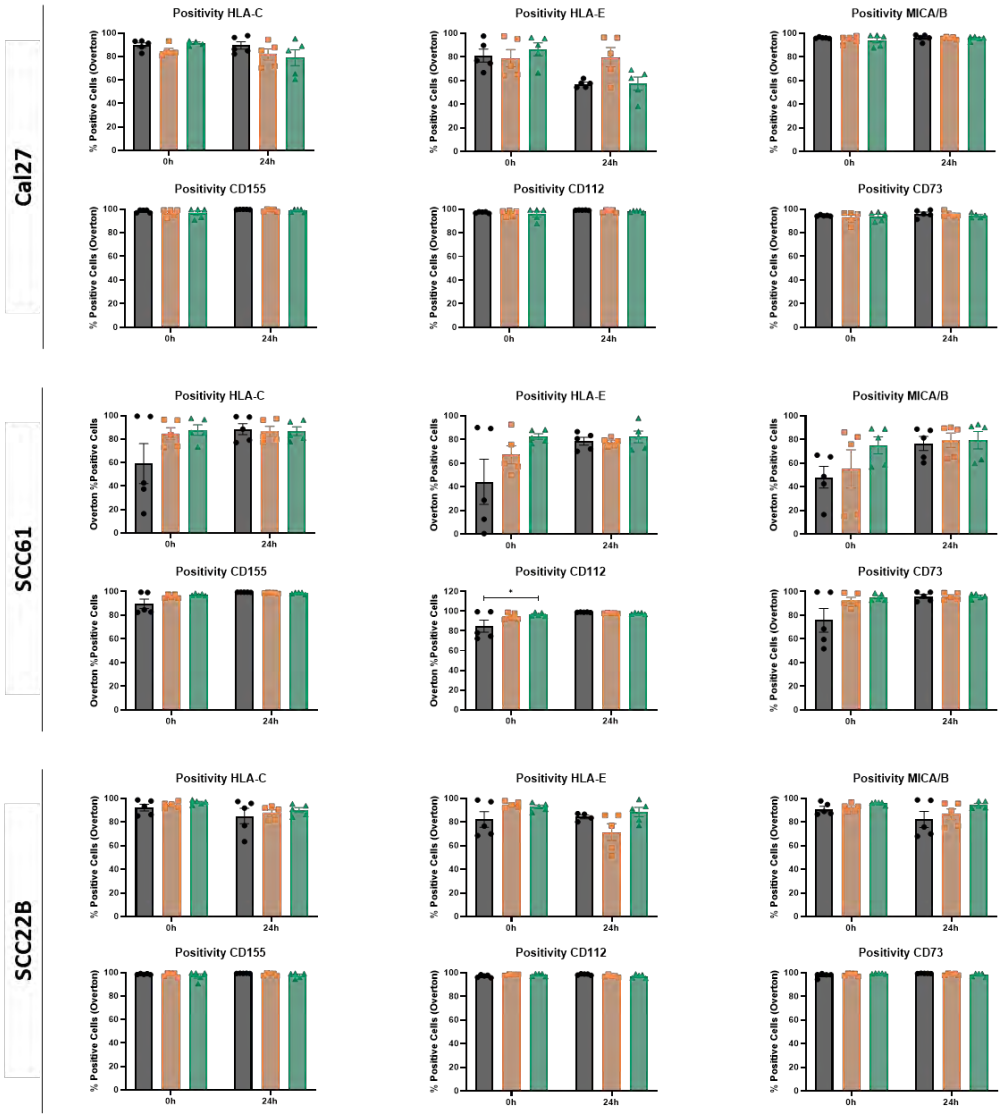

Figure D-3. NTP treatment does not affect the percentage of tumour cells positive for the evaluated immune checkpoints. Quantification of the percentage positive cells after exposure to different NTP intensities, compared to FMO control. Results are depicted as Overton %, immediate (0 h) and one day (24 h) post-treatment for all 3 HNSCC cell lines. Data are represented as mean ± SEM, with individual values shown (n = 5). Statistical significance between untreated cells and the treated conditions was determined using the generalised linear mixed model with post hoc Dunnett's test (* $p \leq 0.05$). Outliers were calculated with the Grubbs' Test.

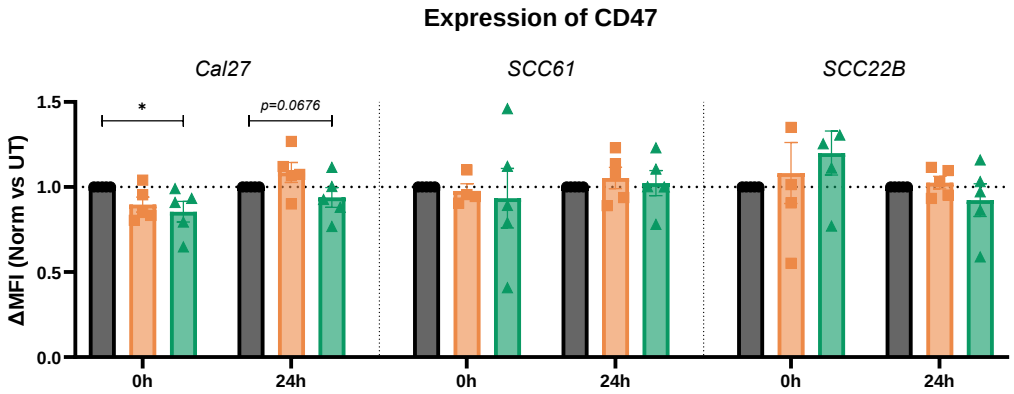

Figure D-4. NTP application results in minor changes in CD47 expression in several HNSCC cell lines. Quantification of the amount of CD47 expression after exposure to different regimes of NTP. Results are depicted as mean fluorescence intensity minus FMO control, normalised to untreated controls (normalised (Norm) ΔMFI), immediate (0 h) and one day (24 h) post-treatment for all 3 HNSCC cell lines. Data are represented as mean ± SEM, with individual values shown (n = 5). Statistical significance between untreated cells and the treated conditions was determined using the generalised linear mixed model with post hoc Dunnett's test (* $p \leq 0.05$). Outliers were calculated with the Grubbs' Test.

References

[1]. Boulos MI, Fauchais PL, Pfender E. Handbook of Thermal Plasmas. Cham: Springer International Publishing; 2023 2023.

[2]. Murphy AB. A perspective on arc welding research: the importance of the arc, unresolved questions and future directions. Plasma Chemistry and Plasma Processing. 2015;35(3):471-89.

[3]. Raiser J, Zenker M. Argon plasma coagulation for open surgical and endoscopic applications: state of the art. Journal of Physics D: Applied Physics. 2006;39(16):3520.

[4]. Nijdam S, Desai KV, Park S-J, Sun PP, Sakai O, Lister G, et al. Foundations of plasma photonics: lamps, lasers, and electromagnetic devices. Plasma Sources Science and Technology. 2023;31(12):123001.

[5]. Kogelschatz U. Dielectric-barrier discharges: their history, discharge physics, and industrial applications. Plasma chemistry and plasma processing. 2003;23(1):1-46.

[6]. Gromov M, Gorbanev Y, Vervloessem E, Morent R, Snyders R, De Geyter N, et al. Electrification of fertilizer production via plasma-based nitrogen fixation: a tutorial on fundamentals. RSC sustainability. 2025.

[7]. Snoeckx R, Bogaerts A. Plasma technology–a novel solution for CO 2 conversion? Chemical Society Reviews. 2017;46(19):5805-63.

[8]. Foster JE. Plasma-based water purification: Challenges and prospects for the future. Physics of Plasmas. 2017;24(5).

[9]. Bekeschus S, von Woedtke T, Emmert S, Schmidt A. Medical gas plasma-stimulated wound healing: Evidence and mechanisms. Redox biology. 2021;46:102116.

[10]. Keidar M. Plasma cancer therapy: Springer; 2020.

[11]. Pecorino L. Molecular biology of cancer: mechanisms, targets, and therapeutics: Oxford university press; 2012.

[12]. Sung H, Ferlay J, Siegel RL, Laversanne M, Soerjomataram I, Jemal A, et al. Global cancer statistics 2020: GLOBOCAN estimates of incidence and mortality

worldwide for 36 cancers in 185 countries. CA: a cancer journal for clinicians. 2021;71(3):209-49.

[13]. Hanahan D, Weinberg RA. The hallmarks of cancer. cell. 2000;100(1):57-70.

[14]. Hanahan D, Weinberg RA. Hallmarks of cancer: the next generation. cell. 2011;144(5):646-74.

[15]. Hanahan D. Hallmarks of cancer: new dimensions. Cancer discovery. 2022;12(1):31-46.

[16]. Bekeschus S, Clemen R. Plasma, cancer, immunity. Journal of Physics D: Applied Physics. 2022;55(47):473003.

[17]. Thariat J, Hannoun-Levi J-M, Sun Myint A, Vuong T, Gérard J-P. Past, present, and future of radiotherapy for the benefit of patients. Nature reviews Clinical oncology. 2013;10(1):52-60.

[18]. Dolmans DE, Fukumura D, Jain RK. Photodynamic therapy for cancer. Nature reviews cancer. 2003;3(5):380-7.

[19]. Chabner BA, Roberts Jr TG. Chemotherapy and the war on cancer. Nature Reviews Cancer. 2005;5(1):65-72.

[20]. A. Baudino T. Targeted cancer therapy: the next generation of cancer treatment. Current drug discovery technologies. 2015;12(1):3-20.

[21]. Ribas A, Wolchok JD. Cancer immunotherapy using checkpoint blockade. Science. 2018;359(6382):1350-5.

[22]. Murphy K, Weaver C. Janeway's immunobiology: Garland science; 2016.

[23]. Vivier E, Di Santo J, Moretta A. Natural killer cells: Springer; 2016.

[24]. Waldhauer I, Steinle A. NK cells and cancer immunosurveillance. Oncogene. 2008;27(45):5932-43.

[25]. Vivier E, Ugolini S, Blaise D, Chabannon C, Brossay L. Targeting natural killer cells and natural killer T cells in cancer. Nature Reviews Immunology. 2012;12(4):239-52.

[26]. Guillerey C, Smyth MJ. NK cells and cancer immunoediting. Natural killer cells. 2016:115-45.

[27]. Laroussi M. Sterilization of contaminated matter with an atmospheric pressure plasma. IEEE Transactions on plasma science. 1996;24(3):1188-91.

[28]. Laroussi M. Plasma medicine: a brief introduction. Plasma. 2018;1(1):47-60.

[29]. Stoffels E, Kieft I, Sladek R. Superficial treatment of mammalian cells using plasma needle. Journal of Physics D: Applied Physics. 2003;36(23):2908.

[30]. Yonson S, Coulombe S, Leveille V, Leask R. Cell treatment and surface functionalization using a miniature atmospheric pressure glow discharge plasma torch. Journal of Physics D: Applied Physics. 2006;39(16):3508.

[31]. Fridman G, Shereshevsky A, Jost MM, Brooks AD, Fridman A, Gutsol A, et al. Floating electrode dielectric barrier discharge plasma in air promoting apoptotic behavior in melanoma skin cancer cell lines. Plasma Chemistry and Plasma Processing. 2007;27:163-76.

[32]. Laroussi M. From Killing Bacteria to Destroying Cancer Cells: 20 Years of Plasma Medicine. Plasma Processes & Polymers. 2014;11(12).

[33]. Vandamme M, Robert E, Pesnel S, Barbosa E, Dozias S, Sobilo J, et al. Antitumor effect of plasma treatment on U87 glioma xenografts: preliminary results. Plasma processes and polymers. 2010;7(3-4):264-73.

[34]. Scholtz V, Pazlarova J, Souskova H, Khun J, Julak J. Nonthermal plasma—A tool for decontamination and disinfection. Biotechnol Adv. 2015;33(6):1108-19.

[35]. Boeckmann L, Schäfer M, Bernhardt T, Semmler ML, Jung O, Ojak G, et al. Cold atmospheric pressure plasma in wound healing and cancer treatment. Applied Sciences. 2020;10(19):6898.

[36]. Bekeschus S. Medical gas plasma technology: Roadmap on cancer treatment and immunotherapy. Redox Biology. 2023:102798.

[37]. Privat-Maldonado A, Schmidt A, Lin A, Weltmann K-D, Wende K, Bogaerts A, et al. ROS from physical plasmas: Redox chemistry for biomedical therapy. Oxidative medicine and cellular longevity. 2019;2019.

[38]. Martin K, Barrett J. Reactive oxygen species as double-edged swords in cellular processes: low-dose cell signaling versus high-dose toxicity. Human & experimental toxicology. 2002;21(2):71-5.

[39]. Szili EJ, Harding FJ, Hong S-H, Herrmann F, Voelcker NH, Short RD. The hormesis effect of plasma-elevated intracellular ROS on HaCaT cells. Journal of Physics D: Applied Physics. 2015;48(49):495401.

[40]. Mattson MP. Hormesis defined. Ageing research reviews. 2008;7(1):1-7.

[41]. Graves DB. The emerging role of reactive oxygen and nitrogen species in redox biology and some implications for plasma applications to medicine and biology. Journal of Physics D: Applied Physics. 2012;45(26):263001.

[42]. Blaser H, Dostert C, Mak TW, Brenner D. TNF and ROS crosstalk in inflammation. Trends in cell biology. 2016;26(4):249-61.

[43]. Sies H, Jones DP. Reactive oxygen species (ROS) as pleiotropic physiological signalling agents. Nature reviews Molecular cell biology. 2020;21(7):363-83.

[44]. Keidar M, Walk R, Shashurin A, Srinivasan P, Sandler A, Dasgupta S, et al. Cold plasma selectivity and the possibility of a paradigm shift in cancer therapy. British journal of cancer. 2011;105(9):1295-301.

[45]. Yan D, Sherman JH, Keidar M. Cold atmospheric plasma, a novel promising anti-cancer treatment modality. Oncotarget. 2017;8(9):15977.

[46]. Trachootham D, Alexandre J, Huang P. Targeting cancer cells by ROS-mediated mechanisms: a radical therapeutic approach? Nature reviews Drug discovery. 2009;8(7):579-91.

[47]. Keidar M. Plasma for cancer treatment. Plasma Sources Science and Technology. 2015;24(3):033001.

[48]. Yan D, Talbot A, Nourmohammadi N, Sherman JH, Cheng X, Keidar M. Toward understanding the selective anticancer capacity of cold atmospheric plasma—A model based on aquaporins. Biointerphases. 2015;10(4).

[49]. Van der Paal J, Neyts EC, Verlackt CC, Bogaerts A. Effect of lipid peroxidation on membrane permeability of cancer and normal cells subjected to oxidative stress. Chemical science. 2016;7(1):489-98.

[50]. Van der Paal J, Verheyen C, Neyts EC, Bogaerts A. Hampering effect of cholesterol on the permeation of reactive oxygen species through phospholipids bilayer: possible explanation for plasma cancer selectivity. Scientific reports. 2017;7(1):1-11.

[51]. Bauer G, Graves DB. Mechanisms of selective antitumor action of cold atmospheric plasma-derived reactive oxygen and nitrogen species. Plasma processes and polymers. 2016;13(12):1157-78.

[52]. Biscop E, Lin A, Van Boxem W, Van Loenhout J, De Backer J, Deben C, et al. The influence of cell type and culture medium on determining cancer selectivity of cold atmospheric plasma treatment. Cancers. 2019;11(9):1287.

[53]. Bekeschus S, Liebelt G, Menz J, Berner J, Sagwal SK, Wende K, et al. Tumor cell metabolism correlates with resistance to gas plasma treatment: The evaluation of three dogmas. Free Radical Biology and Medicine. 2021;167:12-28.

[54]. Lin A, Truong B, Pappas A, Kirifides L, Oubarri A, Chen S, et al. Uniform nanosecond pulsed dielectric barrier discharge plasma enhances anti-tumor effects by induction of immunogenic cell death in tumors and stimulation of macrophages. Plasma processes and polymers. 2015;12(12):1392-9.

[55]. Galluzzi L, Buqué A, Kepp O, Zitvogel L, Kroemer G. Immunogenic cell death in cancer and infectious disease. Nature Reviews Immunology. 2017;17(2):97-111.

[56]. Lin A, Truong B, Patel S, Kaushik N, Choi EH, Fridman G, et al. Nanosecond-pulsed DBD plasma-generated reactive oxygen species trigger immunogenic cell death in A549 lung carcinoma cells through intracellular oxidative stress. International journal of molecular sciences. 2017;18(5):966.

[57]. Bekeschus S, Mueller A, Miller V, Gaipl U, Weltmann K-D. Physical plasma elicits immunogenic cancer cell death and mitochondrial singlet oxygen. IEEE Transactions on Radiation and Plasma Medical Sciences. 2017;2(2):138-46.

[58]. Bekeschus S, Rödder K, Fregin B, Otto O, Lippert M, Weltmann K-D, et al. Toxicity and immunogenicity in murine melanoma following exposure to physical plasma-derived oxidants. Oxidative medicine and cellular longevity. 2017;2017(1):4396467.

[59]. Lin AG, Xiang B, Merlino DJ, Baybutt TR, Sahu J, Fridman A, et al. Non-thermal plasma induces immunogenic cell death in vivo in murine CT26 colorectal tumors. Oncoimmunology. 2018;7(9):e1484978.

[60]. Mizuno K, Yonetamari K, Shirakawa Y, Akiyama T, Ono R. Anti-tumor immune response induced by nanosecond pulsed streamer discharge in mice. Journal of Physics D: Applied Physics. 2017;50(12):12LT01.

[61]. Mahdikia H, Saadati F, Freund E, Gaipl US, Majidzadeh-a K, Shokri B, et al. Gas plasma irradiation of breast cancers promotes immunogenicity, tumor reduction, and an abscopal effect in vivo. Oncoimmunology. 2021;10(1):1859731.

[62]. Lin A, Gorbanev Y, De Backer J, Van Loenhout J, Van Boxem W, Lemière F, et al. Non-thermal plasma as a unique delivery system of short-lived reactive oxygen

and nitrogen species for immunogenic cell death in melanoma cells. Advanced Science. 2019;6(6):1802062.

[63]. Bekeschus S, Clemen R, Nießner F, Sagwal SK, Freund E, Schmidt A. Medical gas plasma jet technology targets murine melanoma in an immunogenic fashion. Advanced Science. 2020;7(10):1903438.

[64]. Miller V, Lin A, Fridman A. Why target immune cells for plasma treatment of cancer. Plasma Chemistry and Plasma Processing. 2016;36(1):259-68.

[65]. Bekeschus S, Clemen R, Metelmann H-R. Potentiating anti-tumor immunity with physical plasma. Clinical Plasma Medicine. 2018;12:17-22.

[66]. Živanić M, Espona-Noguera A, Lin A, Canal C. Current state of cold atmospheric plasma and cancer-immunity cycle: therapeutic relevance and overcoming clinical limitations using hydrogels. Advanced Science. 2023;10(8):2205803.

[67]. Lin A, Razzokov J, Verswyvel H, Privat-Maldonado A, De Backer J, Yusupov M, et al. Oxidation of innate immune checkpoint CD47 on cancer cells with non-thermal plasma. Cancers. 2021;13(3):579.

[68]. Clemen R, Freund E, Mrochen D, Miebach L, Schmidt A, Rauch BH, et al. Gas plasma technology augments ovalbumin immunogenicity and OT-II T cell activation conferring tumor protection in mice. Advanced Science. 2021;8(10):2003395.

[69]. Moritz J, Metelmann H-R, Bekeschus S. Physical plasma treatment of eight human cancer cell lines demarcates upregulation of CD112 as a common immunomodulatory response element. IEEE Transactions on Radiation and Plasma Medical Sciences. 2019;4(3):343-9.

[70]. Clemen R, Heirman P, Lin A, Bogaerts A, Bekeschus S. Physical plasma-treated skin cancer cells amplify tumor cytotoxicity of human natural killer (NK) cells. Cancers. 2020;12(12):3575.

[71]. Lin A, De Backer J, Quatannens D, Cuypers B, Verswyvel H, De La Hoz EC, et al. The effect of local non-thermal plasma therapy on the cancer-immunity cycle in a melanoma mouse model. Bioengineering & Translational Medicine. 2022;7(3):e10314.

[72]. Weltmann KD, Kindel E, von Woedtke T, Hähnel M, Stieber M, Brandenburg R. Atmospheric-pressure plasma sources: Prospective tools for plasma medicine. Pure and Applied Chemistry. 2010;82(6):1223-37.

[73]. Laroussi M, Lu X, Keidar M. Perspective: The physics, diagnostics, and applications of atmospheric pressure low temperature plasma sources used in plasma medicine. Journal of Applied Physics. 2017;122(2).

[74]. Lu X, Laroussi M, Puech V. On atmospheric-pressure non-equilibrium plasma jets and plasma bullets. Plasma Sources Science and Technology. 2012;21(3):034005.

[75]. Iséni S, Reuter S, Weltmann K-D. NO2 dynamics of an Ar/Air plasma jet investigated by in situ quantum cascade laser spectroscopy at atmospheric pressure. Journal of Physics D: Applied Physics. 2014;47(7):075203.

[76]. Lietz AM, Kushner MJ. Molecular admixtures and impurities in atmospheric pressure plasma jets. Journal of Applied Physics. 2018;124(15):153303.

[77]. Reuter S, Tresp H, Wende K, Hammer MU, Winter J, Masur K, et al. From RONS to ROS: tailoring plasma jet treatment of skin cells. IEEE Transactions on Plasma Science. 2012;40(11):2986-93.

[78]. Lin A, Gromov M, Nikiforov A, Smits E, Bogaerts A. Characterization of non-thermal dielectric barrier discharges for plasma medicine: from plastic well plates to skin surfaces. Plasma Chemistry and Plasma Processing. 2023;43(6):1587-612.

[79]. Bekeschus S, Schmidt A, Weltmann K-D, von Woedtke T. The plasma jet kINPen–A powerful tool for wound healing. Clinical Plasma Medicine. 2016;4(1):19-28.

[80]. Reuter S, von Woedtke T, Weltmann K-D. The kINPen—a review on physics and chemistry of the atmospheric pressure plasma jet and its applications. Journal of Physics D: Applied Physics. 2018;51(23):233001.

[81]. Bekeschus S, Freund E, Spadola C, Privat-Maldonado A, Hackbarth C, Bogaerts A, et al. Risk assessment of kINPen plasma treatment of four human pancreatic cancer cell lines with respect to metastasis. Cancers. 2019;11(9):1237.

[82]. Tornin J, Labay C, Tampieri F, Ginebra M-P, Canal C. Evaluation of the effects of cold atmospheric plasma and plasma-treated liquids in cancer cell cultures. Nature Protocols. 2021;16(6):2826-50.

[83]. Dubuc A, Monsarrat P, Virard F, Merbahi N, Sarrette J-P, Laurencin-Dalicieux S, et al. Use of cold-atmospheric plasma in oncology: A concise systematic review. Therapeutic advances in medical oncology. 2018;10:1758835918786475.

[84]. Metelmann H-R, Seebauer C, Miller V, Fridman A, Bauer G, Graves DB, et al. Clinical experience with cold plasma in the treatment of locally advanced head and neck cancer. Clinical Plasma Medicine. 2018;9:6-13.

[85]. Stratmann B, Costea T-C, Nolte C, Hiller J, Schmidt J, Reindel J, et al. Effect of cold atmospheric plasma therapy vs standard therapy placebo on wound healing in patients with diabetic foot ulcers: a randomized clinical trial. JAMA network open. 2020;3(7):e2010411-e.

[86]. Schmidt-Bleker A, Bansemer R, Reuter S, Weltmann KD. How to produce an NOx-instead of Ox-based chemistry with a cold atmospheric plasma jet. Plasma Processes and Polymers. 2016;13(11):1120-7.

[87]. Bruggeman PJ, Kushner MJ, Locke BR, Gardeniers JG, 981 07, Sweden, Graham W, Graves DB, et al. Plasma–liquid interactions: a review and roadmap. Plasma sources science and technology. 2016;25(5):053002.

[88]. Vanraes P, Bogaerts A. Plasma physics of liquids—A focused review. Applied Physics Reviews. 2018;5(3).

[89]. Huang Z, Xiao A, Liu D, Lu X, Ostrikov K. Plasma-water-based nitrogen fixation: Status, mechanisms, and opportunities. Plasma Processes and Polymers. 2022;19(4):2100198.

[90]. Hansen L, Schmidt-Bleker A, Bansemer R, Kersten H, Weltmann K-D, Reuter S. Influence of a liquid surface on the NOx production of a cold atmospheric pressure plasma jet. Journal of Physics D: Applied Physics. 2018;51(47):474002.

[91]. Kovačević VV, Sretenović GB, Slikboer E, Guaitella O, Sobota A, Kuraica MM. The effect of liquid target on a nonthermal plasma jet—imaging, electric fields, visualization of gas flow and optical emission spectroscopy. Journal of Physics D: Applied Physics. 2018;51(6):065202.

[92]. Neyts EC, Yusupov M, Verlackt CC, Bogaerts A. Computer simulations of plasma–biomolecule and plasma–tissue interactions for a better insight in plasma medicine. Journal of Physics D: Applied Physics. 2014;47(29):293001.

[93]. Bogaerts A, Khosravian N, Van der Paal J, Verlackt CC, Yusupov M, Kamaraj B, et al. Multi-level molecular modelling for plasma medicine. Journal of Physics D: Applied Physics. 2015;49(5):054002.

[94]. Ghasemitarei M, Ghorbi T, Yusupov M, Zhang Y, Zhao T, Shali P, et al. Effects of Nitro-Oxidative Stress on Biomolecules: Part 1—Non-Reactive Molecular Dynamics Simulations. Biomolecules. 2023;13(9):1371.

[95]. Alves L, Bogaerts A, Guerra V, Turner M. Foundations of modelling of nonequilibrium low-temperature plasmas. Plasma Sources Science and Technology. 2018;27(2):023002.

[96]. Van Gaens W, Bogaerts A. Kinetic modelling for an atmospheric pressure argon plasma jet in humid air. Journal of Physics D: Applied Physics. 2013;46(27):275201.

[97]. Van Gaens W, Iseni S, Schmidt-Bleker A, Weltmann K-D, Reuter S, Bogaerts A. Numerical analysis of the effect of nitrogen and oxygen admixtures on the chemistry of an argon plasma jet operating at atmospheric pressure. New Journal of Physics. 2015;17(3):033003.

[98]. Van Gaens W, Bogaerts A. Reaction pathways of biomedically active species in an Ar plasma jet. Plasma Sources Science and Technology. 2014;23(3):035015.

[99]. Van Gaens W, Bruggeman PJ, Bogaerts A. Numerical analysis of the NO and O generation mechanism in a needle-type plasma jet. New Journal of Physics. 2014;16(6):063054.

[100]. Schmidt-Bleker A, Winter J, Iseni S, Dünnbier M, Weltmann K, Reuter S. Reactive species output of a plasma jet with a shielding gas device—combination of FTIR absorption spectroscopy and gas phase modelling. Journal of Physics D: Applied Physics. 2014;47(14):145201.

[101]. Schmidt-Bleker A, Winter J, Bösel A, Reuter S, Weltmann K-D. On the plasma chemistry of a cold atmospheric argon plasma jet with shielding gas device. Plasma Sources Science and Technology. 2015;25(1):015005.

[102]. Lietz AM, Kushner MJ. Air plasma treatment of liquid covered tissue: long timescale chemistry. Journal of Physics D: Applied Physics. 2016;49(42):425204.

[103]. Van Boxem W, Van der Paal J, Gorbanev Y, Vanuytsel S, Smits E, Dewilde S, et al. Anti-cancer capacity of plasma-treated PBS: Effect of chemical composition on cancer cell cytotoxicity. Scientific reports. 2017;7(1):16478.

[104]. Batchelor GK. An introduction to fluid dynamics: Cambridge university press; 2000.

[105]. Reuter S, Winter J, Schmidt-Bleker A, Schroeder D, Lange H, Knake N, et al. Atomic oxygen in a cold argon plasma jet: TALIF spectroscopy in ambient air with modelling and measurements of ambient species diffusion. Plasma Sources Science and Technology. 2012;21(2):024005.

[106]. Dünnbier M, Schmidt-Bleker A, Winter J, Wolfram M, Hippler R, Weltmann K, et al. Ambient air particle transport into the effluent of a cold atmospheric-pressure argon plasma jet investigated by molecular beam mass spectrometry. Journal of Physics D: Applied Physics. 2013;46(43):435203.

[107]. Schmidt-Bleker A, Reuter S, Weltmann K. Quantitative schlieren diagnostics for the determination of ambient species density, gas temperature and calorimetric power of cold atmospheric plasma jets. Journal of Physics D: Applied Physics. 2015;48(17):175202.

[108]. Reuter S, Winter J, Schmidt-Bleker A, Tresp H, Hammer MU, Weltmann K-D. Controlling the ambient air affected reactive species composition in the effluent of an argon plasma jet. IEEE Transactions on Plasma Science. 2012;40(11):2788-94.

[109]. Rauf S, Kushner MJ. Dynamics of a coplanar-electrode plasma display panel cell. I. Basic operation. Journal of applied physics. 1999;85(7):3460-9.

[110]. Babaeva NY, Kushner MJ. Intracellular electric fields produced by dielectric barrier discharge treatment of skin. Journal of Physics D: Applied Physics. 2010;43(18):185206.

[111]. Babaeva NY, Kushner MJ. Reactive fluxes delivered by dielectric barrier discharge filaments to slightly wounded skin. Journal of Physics D: Applied Physics. 2012;46(2):025401.

[112]. Tian W, Kushner MJ. Atmospheric pressure dielectric barrier discharges interacting with liquid covered tissue. Journal of Physics D: Applied Physics. 2014;47(16):165201.

[113]. Tian W, Kushner MJ. Long-term effects of multiply pulsed dielectric barrier discharges in air on thin water layers over tissue: stationary and random streamers. Journal of Physics D: Applied Physics. 2015;48(49):494002.

[114]. Tian W, Lietz AM, Kushner MJ. The consequences of air flow on the distribution of aqueous species during dielectric barrier discharge treatment of thin water layers. Plasma Sources Science and Technology. 2016;25(5):055020.

[115]. Kruszelnicki J, Lietz AM, Kushner MJ. Atmospheric pressure plasma activation of water droplets. Journal of Physics D: Applied Physics. 2019;52(35):355207.

[116]. Norberg SA, Johnsen E, Kushner MJ. Formation of reactive oxygen and nitrogen species by repetitive negatively pulsed helium atmospheric pressure plasma jets propagating into humid air. Plasma Sources Science and Technology. 2015;24(3):035026.

[117]. Schmidt-Bleker A, Norberg SA, Winter J, Johnsen E, Reuter S, Weltmann K, et al. Propagation mechanisms of guided streamers in plasma jets: the influence of electronegativity of the surrounding gas. Plasma Sources Science and Technology. 2015;24(3):035022.

[118]. Norberg SA, Tian W, Johnsen E, Kushner MJ. Atmospheric pressure plasma jets interacting with liquid covered tissue: touching and not-touching the liquid. Journal of Physics D: Applied Physics. 2014;47(47):475203.

[119]. Mohades S, Lietz AM, Kruszelnicki J, Kushner MJ. Helium plasma jet interactions with water in well plates. Plasma Processes and Polymers. 2020;17(3):1900179.

[120]. Lin P, Zhang J, Nguyen T, Donnelly VM, Economou DJ. Numerical simulation of an atmospheric pressure plasma jet with coaxial shielding gas. Journal of Physics D: Applied Physics. 2020;54(7):075205.

[121]. Semenov I, Weltmann K. Modelling of turbulent reacting flow for a cold atmospheric pressure argon plasma jet. Plasma Sources Science and Technology. 2020;29(5):055001.

[122]. Yagi I, Ono R, Oda T, Takaki K. Two-dimensional LIF measurements of humidity and OH density resulting from evaporated water from a wet surface in plasma for medical use. Plasma Sources Science and Technology. 2014;24(1):015002.

[123]. Hirst AM, Frame FM, Arya M, Maitland NJ, O'Connell D. Low temperature plasmas as emerging cancer therapeutics: the state of play and thoughts for the future. Tumor Biology. 2016;37:7021-31.

[124]. Lindsay A, Anderson C, Slikboer E, Shannon S, Graves D. Momentum, heat, and neutral mass transport in convective atmospheric pressure plasma-liquid systems and implications for aqueous targets. Journal of Physics D: Applied Physics. 2015;48(42):424007.

[125]. Verlackt C, Van Boxem W, Bogaerts A. Transport and accumulation of plasma generated species in aqueous solution. Physical Chemistry Chemical Physics. 2018;20(10):6845-59.

[126]. Heirman P, Van Boxem W, Bogaerts A. Reactivity and stability of plasma-generated oxygen and nitrogen species in buffered water solution: a computational study. Physical Chemistry Chemical Physics. 2019;21(24):12881-94.

[127]. Semenov I, Weltmann K, Loffhagen D. Modelling of the transport phenomena for an atmospheric-pressure plasma jet in contact with liquid. Journal of Physics D: Applied Physics. 2019;52(31):315203.

[128]. Kamidollayev T, Trelles JP. Modeling of reactive species interphase transport in plasma jet impinging on water. Journal of Physics D: Applied Physics. 2023;56(50):505203.

[129]. Liu Y, Peng W, Liu D, Fu F. Comparison of the transportation of reactive species from He and Ar atmospheric-pressure plasma jets to aqueous solutions. Journal of Physics D: Applied Physics. 2024.

[130]. Scott DE, Bayly AR, Abell C, Skidmore J. Small molecules, big targets: drug discovery faces the protein–protein interaction challenge. Nature Reviews Drug Discovery. 2016;15(8):533-50.

[131]. Yusupov M, Wende K, Kupsch S, Neyts EC, Reuter S, Bogaerts A. Effect of head group and lipid tail oxidation in the cell membrane revealed through integrated simulations and experiments. Scientific reports. 2017;7(1):1-14.

[132]. Razzokov J, Yusupov M, Cordeiro RM, Bogaerts A. Atomic scale understanding of the permeation of plasma species across native and oxidized membranes. Journal of Physics D: Applied Physics. 2018;51(36):365203.

[133]. Oliveira MC, Yusupov M, Bogaerts A, Cordeiro RM. How do nitrated lipids affect the properties of phospholipid membranes? Archives of Biochemistry and Biophysics. 2020;695:108548.

[134]. Oliveira MC, Yusupov M, Cordeiro RM, Bogaerts A. Unraveling the permeation of reactive species across nitrated membranes by computer simulations. Computers in Biology and Medicine. 2021;136:104768.

[135]. Yusupov M, Yan D, Cordeiro RM, Bogaerts A. Atomic scale simulation of H2O2 permeation through aquaporin: Toward the understanding of plasma cancer treatment. Journal of Physics D: Applied Physics. 2018;51(12):125401.

[136]. Yusupov M, Razzokov J, Cordeiro RM, Bogaerts A. Transport of reactive oxygen and nitrogen species across aquaporin: A molecular level picture. Oxidative medicine and cellular longevity. 2019;2019.

[137]. Yusupov M, Van der Paal J, Neyts EC, Bogaerts A. Synergistic effect of electric field and lipid oxidation on the permeability of cell membranes. Biochimica et Biophysica Acta (BBA)-General Subjects. 2017;1861(4):839-47.

[138]. Yusupov M, Lackmann JW, Razzokov J, Kumar S, Stapelmann K, Bogaerts A. Impact of plasma oxidation on structural features of human epidermal growth factor. Plasma Processes and Polymers. 2018;15(8):1800022.

[139]. Yusupov M, Privat-Maldonado A, Cordeiro RM, Verswyvel H, Shaw P, Razzokov J, et al. Oxidative damage to hyaluronan–CD44 interactions as an underlying mechanism of action of oxidative stress-inducing cancer therapy. Redox biology. 2021;43:101968.

[140]. Comsol Multiphysics [Available from: www.comsol.com.

[141]. Van Rens JF, Schoof JT, Ummelen FC, Van Vugt DC, Bruggeman PJ, Van Veldhuizen E. Induced liquid phase flow by RF Ar cold atmospheric pressure plasma jet. IEEE Transactions on Plasma Science. 2014;42(10):2622-3.

[142]. Comsol Multiphysics CFD Module User's Guide [

[143]. Iseni S, Schmidt-Bleker A, Winter J, Weltmann K-D, Reuter S. Atmospheric pressure streamer follows the turbulent argon air boundary in a MHz argon plasma jet investigated by OH-tracer PLIF spectroscopy. Journal of Physics D: Applied Physics. 2014;47(15):152001.

[144]. Lee JHW, Chu VH. Turbulent Jets. In: Lee JHW, Chu VH, editors. Turbulent Jets and Plumes: A Lagrangian Approach. Boston, MA: Springer US; 2003. p. 21-54.

[145]. Menter FR, Kuntz M, Langtry R. Ten years of industrial experience with the SST turbulence model. Turbulence, heat and mass transfer. 2003;4(1):625-32.

[146]. Comsol Multiphysics Heat Transfer Module User's Guide [

[147]. Bird RB, Stewart WE, Lightfoot EN. Transport Phenomena: Wiley; 2006.

[148]. Comsol Multiphysics Chemical Reaction Engineering Module User's Guide [

[149]. Kee RJ, Coltrin ME, Glarborg P. Chemically reacting flow: theory and practice: John Wiley & Sons; 2005.

[150]. Thomson GW. The Antoine equation for vapor-pressure data. Chemical reviews. 1946;38(1):1-39.

[151]. Robert E, Sarron V, Darny T, Riès D, Dozias S, Fontane J, et al. Rare gas flow structuration in plasma jet experiments. Plasma Sources Science and Technology. 2014;23(1):012003.

[152]. Stancampiano A, Bocanegra PE, Dozias S, Pouvesle J-M, Robert E. Evidence, origin and impact of liquid flows in plasma medicine in vitro treatments with APPJs. Plasma Sources Science and Technology. 2021;30(1):015002.

[153]. Smith FL, Harvey AH. Avoid common pitfalls when using Henry's law. Chemical engineering progress. 2007;103(9):33-9.

[154]. Winter J, Wende K, Masur K, Iseni S, Dünnbier M, Hammer M, et al. Feed gas humidity: a vital parameter affecting a cold atmospheric-pressure plasma jet and plasma-treated human skin cells. Journal of Physics D: Applied Physics. 2013;46(29):295401.

[155]. Bekeschus S, Iseni S, Reuter S, Masur K, Weltmann K-D. Nitrogen shielding of an argon plasma jet and its effects on human immune cells. IEEE Transactions on Plasma Science. 2015;43(3):776-81.

[156]. Schmidt A, Bekeschus S, Jablonowski H, Barton A, Weltmann K-D, Wende K. Role of ambient gas composition on cold physical plasma-elicited cell signaling in keratinocytes. Biophysical Journal. 2017;112(11):2397-407.

[157]. Li J, Guo H, Zhang X-F, Li H-P. Numerical and experimental studies on the interactions between the radio-frequency glow discharge plasma jet and the shielding gas at atmosphere. IEEE Transactions on Plasma Science. 2018;46(8):2766-75.

[158]. Von Woedtke T, Metelmann HR, Weltmann KD. Clinical plasma medicine: state and perspectives of in vivo application of cold atmospheric plasma. Contributions to Plasma Physics. 2014;54(2):104-17.

[159]. Reuter S, Winter J, Iséni S, Schmidt-Bleker A, Dünnbier M, Masur K, et al. The influence of feed gas humidity versus ambient humidity on atmospheric pressure plasma jet-effluent chemistry and skin cell viability. IEEE Transactions on Plasma Science. 2014;43(9):3185-92.

[160]. Winter J, Tresp H, Hammer M, Iseni S, Kupsch S, Schmidt-Bleker A, et al. Tracking plasma generated H2O2 from gas into liquid phase and revealing its dominant impact on human skin cells. Journal of Physics D: Applied Physics. 2014;47(28):285401.

[161]. Hähnel M, von Woedtke T, Weltmann KD. Influence of the air humidity on the reduction of Bacillus spores in a defined environment at atmospheric pressure using a dielectric barrier surface discharge. Plasma processes and polymers. 2010;7(3-4):244-9.

[162]. Yan D, Talbot A, Nourmohammadi N, Cheng X, Canady J, Sherman J, et al. Principles of using cold atmospheric plasma stimulated media for cancer treatment. Scientific reports. 2015;5(1):18339.

[163]. Verreycken T, Mensink R, Van Der Horst R, Sadeghi N, Bruggeman PJ. Absolute OH density measurements in the effluent of a cold atmospheric-pressure Ar–H2O RF plasma jet in air. Plasma Sources Science and Technology. 2013;22(5):055014.

[164]. Gorbanev Y, Van der Paal J, Van Boxem W, Dewilde S, Bogaerts A. Reaction of chloride anion with atomic oxygen in aqueous solutions: can cold plasma help in chemistry research? Physical Chemistry Chemical Physics. 2019;21(8):4117-21.

[165]. Wenske S, Lackmann J-W, Busch LM, Bekeschus S, von Woedtke T, Wende K. Reactive species driven oxidative modifications of peptides—Tracing physical plasma liquid chemistry. Journal of Applied Physics. 2021;129(19).

[166]. Winter J, Sousa JS, Sadeghi N, Schmidt-Bleker A, Reuter S, Puech V. The spatio-temporal distribution of He (23S1) metastable atoms in a MHz-driven helium plasma jet is influenced by the oxygen/nitrogen ratio of the surrounding atmosphere. Plasma Sources Science and Technology. 2015;24(2):025015.

[167]. Neoplas. Optional accessories for kINPen®IND [Available from: www.neoplas.eu/en/accessorieskinpenind.html.

[168]. Tresp H, Hammer MU, Weltmann K-D, Reuter S. Effects of atmosphere composition and liquid type on plasma-generated reactive species in biologically relevant solutions. Plasma Medicine. 2013;3(1-2).

[169]. Tampieri F, Gorbanev Y, Sardella E. Plasma-treated liquids in medicine: Let's get chemical. Plasma Processes and Polymers. 2023:e2300077.

[170]. Roquemore W, Tankin R, Chiu H, Lottes S. A study of a bluff-body combustor using laser sheet lighting. Experiments in Fluids. 1986;4:205-13.

[171]. Tong Y, Liu X, Chen S, Li Z, Klingmann J. Effects of the position of a bluff-body on the diffusion flames: A combined experimental and numerical study. Applied Thermal Engineering. 2018;131:507-21.

[172]. Kapaldo J, Han X, Ptasinska S. Shielding-gas-controlled atmospheric pressure plasma jets: Optical emission, reactive oxygen species, and the effect on cancer cells. Plasma Processes and Polymers. 2019;16(5):1800169.

[173]. Gazzah MH, Belmabrouk H. Directed co-flow effects on local entropy generation in turbulent heated round jets. Computers & Fluids. 2014;105:285-93.

[174]. Sander R. Compilation of Henry's law constants (version 5.0. 0) for water as solvent. Atmospheric Chemistry and Physics. 2023;23(19):10901-2440.

[175]. Hassan ME, Janda M, Machala Z. Transport of gaseous hydrogen peroxide and ozone into bulk water vs. electrosprayed aerosol. Water. 2021;13(2):182.

[176]. Hassan ME, Janda M, Machala Z. Comparison of the Transport of Reactive Nitrogen Plasma Species into Water Bulk vs. Aerosolized Microdroplets. Plasma Chemistry and Plasma Processing. 2024:1-29.

[177]. Jablonowski H, Schmidt-Bleker A, Weltmann K-D, von Woedtke T, Wende K. Non-touching plasma–liquid interaction–where is aqueous nitric oxide generated? Physical Chemistry Chemical Physics. 2018;20(39):25387-98.

[178]. Chen C, Liu D, Liu Z, Yang A, Chen H, Shama G, et al. A model of plasma-biofilm and plasma-tissue interactions at ambient pressure. Plasma Chemistry and Plasma Processing. 2014;34:403-41.

[179]. Bissonnette-Dulude J, Heirman P, Coulombe S, Bogaerts A, Gervais T, Reuter S. Coupling the COST reference plasma jet to a microfluidic device: a computational study. Plasma Sources Science and Technology. 2024;33(1):015001.

[180]. Ikuse K, Hamaguchi S. Roles of the reaction boundary layer and long diffusion of stable reactive nitrogen species (RNS) in plasma-irradiated water as an oxidizing media—numerical simulation study. Japanese Journal of Applied Physics. 2022;61(7):076002.

[181]. Oinuma G, Nayak G, Du Y, Bruggeman PJ. Controlled plasma–droplet interactions: a quantitative study of OH transfer in plasma–liquid interaction. Plasma Sources Science and Technology. 2020;29(9):095002.

[182]. Nayak G, Oinuma G, Yue Y, Sousa JS, Bruggeman PJ. Plasma-droplet interaction study to assess transport limitations and the role of· OH, O·, H·, O2 (a 1Δg), O3, He (23 S) and Ar (1s 5) in formate decomposition. Plasma Sources Science and Technology. 2021;30(11):115003.

[183]. Ning W, Lai J, Kruszelnicki J, Foster JE, Dai D, Kushner MJ. Propagation of positive discharges in an air bubble having an embedded water droplet. Plasma Sources Science and Technology. 2021;30(1):015005.

[184]. Parsey G, Lietz AM, Kushner MJ. Guided plasma jets directed onto wet surfaces: angular dependence and control. Journal of Physics D: Applied Physics. 2020;54(4):045206.

[185]. Beltran FJ. Ozone reaction kinetics for water and wastewater systems: crc Press; 2003.

[186]. Liu Y, Liu D, Zhang J, Sun B, Luo S, Zhang H, et al. Fluid model of plasma–liquid interaction: The effect of interfacial boundary conditions and Henry's law constants. AIP Advances. 2021;11(5).

[187]. Kolb C, Cox RA, Abbatt J, Ammann M, Davis E, Donaldson D, et al. An overview of current issues in the uptake of atmospheric trace gases by aerosols and clouds. Atmospheric Chemistry and Physics. 2010;10(21):10561-605.

[188]. Davidovits P, Kolb CE, Williams LR, Jayne JT, Worsnop DR. Update 1 of: Mass Accommodation and Chemical Reactions at Gas−Liquid Interfaces. Chemical Reviews. 2011;111(4).

[189]. Garrett BC, Schenter GK, Morita A. Molecular simulations of the transport of molecules across the liquid/vapor interface of water. Chemical reviews. 2006;106(4):1355-74.

[190]. Morita A, Garrett BC. Molecular theory of mass transfer kinetics and dynamics at gas–water interface. Fluid dynamics research. 2008;40(7-8):459.

[191]. Burkholder J, Sander S, Abbatt J, Barker J, Cappa C, Crounse J, et al. Chemical kinetics and photochemical data for use in atmospheric studies; evaluation number 19. Pasadena, CA: Jet Propulsion Laboratory, National Aeronautics and Space …; 2020.

[192]. Hogg N. Detection of nitric oxide by electron paramagnetic resonance spectroscopy. Free Radical Biology and Medicine. 2010;49(2):122-9.

[193]. Goldstein S, Russo A, Samuni A. Reactions of PTIO and carboxy-PTIO with· NO,· NO2, and O 2.¯. Journal of Biological Chemistry. 2003;278(51):50949-55.

[194]. Lewis WK, Whitman WG. Principles of gas absorption. Industrial & Engineering Chemistry. 1924;16(12):1215-20.

[195]. Danckwerts P. Significance of liquid-film coefficients in gas absorption. Industrial & Engineering Chemistry. 1951;43(6):1460-7.

[196]. Vanraes P, Bogaerts A. The essential role of the plasma sheath in plasma–liquid interaction and its applications—A perspective. Journal of Applied Physics. 2021;129(22).

[197]. Mohamed H, Gebski E, Reyes R, Beane S, Wigdahl B, Krebs FC, et al. Differential effect of non-thermal plasma RONS on two human leukemic cell populations. Cancers. 2021;13(10):2437.

[198]. Chester C, Fritsch K, Kohrt HE. Natural killer cell immunomodulation: targeting activating, inhibitory, and co-stimulatory receptor signaling for cancer immunotherapy. Frontiers in immunology. 2015;6:601.

[199]. Pegram HJ, Andrews DM, Smyth MJ, Darcy PK, Kershaw MH. Activating and inhibitory receptors of natural killer cells. Immunology and cell biology. 2011;89(2):216-24.

[200]. Vivier E, Raulet DH, Moretta A, Caligiuri MA, Zitvogel L, Lanier LL, et al. Innate or adaptive immunity? The example of natural killer cells. science. 2011;331(6013):44-9.

[201]. Ghasemitarei M, Yusupov M, Razzokov J, Shokri B, Bogaerts A. Effect of oxidative stress on cystine transportation by xC^{-} antiporter. Archives of biochemistry and biophysics. 2019;674:108114.

[202]. Mandal R, Şenbabaoğlu Y, Desrichard A, Havel JJ, Dalin MG, Riaz N, et al. The head and neck cancer immune landscape and its immunotherapeutic implications. JCI insight. 2016;1(17).

[203]. Paech C, Albrecht V, Putke K, Schöfl G, Schöne B, Schmidt AH, et al. HLA-E diversity unfolded: Identification and characterization of 170 novel HLA-E alleles. Hla. 2021;97(5):389-98.

[204]. Parham P. MHC class I molecules and KIRs in human history, health and survival. Nature reviews immunology. 2005;5(3):201-14.

[205]. Abraham MJ, Murtola T, Schulz R, Páll S, Smith JC, Hess B, et al. GROMACS: High performance molecular simulations through multi-level parallelism from laptops to supercomputers. SoftwareX. 2015;1:19-25.

[206]. Schmid N, Eichenberger AP, Choutko A, Riniker S, Winger M, Mark AE, et al. Definition and testing of the GROMOS force-field versions 54A7 and 54B7. European biophysics journal. 2011;40(7):843-56.

[207]. Petrie EJ, Clements CS, Lin J, Sullivan LC, Johnson D, Huyton T, et al. CD94-NKG2A recognition of human leukocyte antigen (HLA)-E bound to an HLA class I leader sequence. The Journal of experimental medicine. 2008;205(3):725-35.

[208]. Fan QR, Long EO, Wiley DC. Crystal structure of the human natural killer cell inhibitory receptor KIR2DL1–HLA-Cw4 complex. Nature immunology. 2001;2(5):452-60.

[209]. Petrov D, Margreitter C, Grandits M, Oostenbrink C, Zagrovic B. A systematic framework for molecular dynamics simulations of protein post-translational modifications. PLoS computational biology. 2013;9(7):e1003154.

[210]. Berendsen H-J-C, Grigera J-R, Straatsma TP. The missing term in effective pair potentials. Journal of Physical Chemistry. 1987;91(24):6269-71.

[211]. Bussi G, Donadio D, Parrinello M. Canonical sampling through velocity rescaling. The Journal of chemical physics. 2007;126(1).

[212]. Parrinello M, Rahman A. Polymorphic transitions in single crystals: A new molecular dynamics method. Journal of Applied physics. 1981;52(12):7182-90.

[213]. Tironi IG, Sperb R, Smith PE, van Gunsteren WF. A generalized reaction field method for molecular dynamics simulations. The Journal of chemical physics. 1995;102(13):5451-9.

[214]. Humphrey W, Dalke A, Schulten K. VMD: visual molecular dynamics. Journal of molecular graphics. 1996;14(1):33-8.

[215]. Kästner J. Umbrella sampling. Wiley Interdisciplinary Reviews: Computational Molecular Science. 2011;1(6):932-42.

[216]. Hub JS, De Groot BL, Van Der Spoel D. g_wham・A Free Weighted Histogram Analysis Implementation Including Robust Error and Autocorrelation Estimates. Journal of chemical theory and computation. 2010;6(12):3713-20.

[217]. Margreitter C, Petrov D, Zagrovic B. Vienna-PTM web server: a toolkit for MD simulations of protein post-translational modifications. Nucleic acids research. 2013;41(W1):W422-W6.

[218]. Takai E, Kitamura T, Kuwabara J, Ikawa S, Yoshizawa S, Shiraki K, et al. Chemical modification of amino acids by atmospheric-pressure cold plasma in aqueous solution. Journal of Physics D: Applied Physics. 2014;47(28):285403.

[219]. Zhou R, Zhou R, Zhuang J, Zong Z, Zhang X, Liu D, et al. Interaction of atmospheric-pressure air microplasmas with amino acids as fundamental processes in aqueous solution. PloS one. 2016;11(5):e0155584.

[220]. Wenske S, Lackmann J-W, Bekeschus S, Weltmann K-D, Von Woedtke T, Wende K. Nonenzymatic post-translational modifications in peptides by cold plasma-derived reactive oxygen and nitrogen species. Biointerphases. 2020;15(6).

[221]. Lins L, Thomas A, Brasseur R. Analysis of accessible surface of residues in proteins. Protein science. 2003;12(7):1406-17.

[222]. Lin A, Sahun M, Biscop E, Verswyvel H, De Waele J, De Backer J, et al. Acquired non-thermal plasma resistance mediates a shift towards aerobic glycolysis and ferroptotic cell death in melanoma. Drug Resistance Updates. 2023;67:100914.

[223]. Verswyvel H, Deben C, Wouters A, Lardon F, Bogaerts A, Smits E, et al. Phototoxicity and cell passage affect intracellular reactive oxygen species levels and sensitivity towards non-thermal plasma treatment in fluorescently-labeled cancer cells. Journal of Physics D: Applied Physics. 2023;56(29):294001.

[224]. Debiec KT, Gronenborn AM, Chong LT. Evaluating the strength of salt bridges: a comparison of current biomolecular force fields. The Journal of Physical Chemistry B. 2014;118(24):6561-9.

[225]. Shaw P, Kumar N, Privat-Maldonado A, Smits E, Bogaerts A. Cold atmospheric plasma increases temozolomide sensitivity of three-dimensional glioblastoma spheroids via oxidative stress-mediated DNA damage. Cancers. 2021;13(8):1780.

[226]. Živanić M, Espona-Noguera A, Verswyvel H, Smits E, Bogaerts A, Lin A, et al. Injectable Plasma-Treated Alginate Hydrogel for Oxidative Stress Delivery to Induce Immunogenic Cell Death in Osteosarcoma. Advanced Functional Materials. 2024;34(14):2312005.

[227]. Ziegler AE, Fittje P, Müller LM, Ahrenstorf AE, Hagemann K, Hagen SH, et al. The co-inhibitory receptor TIGIT regulates NK cell function and is upregulated in

human intrahepatic CD56bright NK cells. Frontiers in immunology. 2023;14:1117320.

[228]. Xing S, Ferrari de Andrade L. NKG2D and MICA/B shedding: a 'tag game'between NK cells and malignant cells. Clinical & translational immunology. 2020;9(12):e1230.

[229]. Borst L, van der Burg SH, van Hall T. The NKG2A–HLA-E axis as a novel checkpoint in the tumor microenvironment. Clinical cancer research. 2020;26(21):5549-56.

[230]. Lupo KB, Yao X, Borde S, Wang J, Torregrosa-Allen S, Elzey BD, et al. synNotch-programmed iPSC-derived NK cells usurp TIGIT and CD73 activities for glioblastoma therapy. Nature Communications. 2024;15(1):1909.

[231]. Ge Z, Peppelenbosch MP, Sprengers D, Kwekkeboom J. TIGIT, the next step towards successful combination immune checkpoint therapy in cancer. Frontiers in immunology. 2021;12:699895.

[232]. Goulding J, Yeh W-I, Hancock B, Blum R, Xu T, Yang B-H, et al. A chimeric antigen receptor uniquely recognizing MICA/B stress proteins provides an effective approach to target solid tumors. Med. 2023;4(7):457-77. e8.

[233]. Clemen R, Arlt K, Miebach L, von Woedtke T, Bekeschus S. Oxidized proteins differentially affect maturation and activation of human monocyte-derived cells. Cells. 2022;11(22):3659.

[234]. Gkantaras A, Kotzamanidis C, Kyriakidis K, Farmaki E, Makedou K, Tzimagiorgis G, et al. Multi-Cohort Transcriptomic Profiling of Medical Gas Plasma-Treated Cancers Reveals the Role of Immunogenic Cell Death. Cancers. 2024;16(12):2186.

[235]. Lin L, Wang L, Liu Y, Xu C, Tu Y, Zhou J. Non-thermal plasma inhibits tumor growth and proliferation and enhances the sensitivity to radiation in vitro and in vivo. Oncology Reports. 2018;40(6):3405-15.

[236]. Prašnikar E, Perdih A, Borišek J. All-atom simulations reveal a key interaction network in the HLA-E/NKG2A/CD94 immune complex fine-tuned by the nonameric peptide. Journal of Chemical Information and Modeling. 2021;61(7):3593-603.

[237]. Sullivan LC, Clements CS, Beddoe T, Johnson D, Hoare HL, Lin J, et al. The heterodimeric assembly of the CD94-NKG2 receptor family and implications for human leukocyte antigen-E recognition. Immunity. 2007;27(6):900-11.

[238]. Ghasemitarei M, Privat-Maldonado A, Yusupov M, Rahnama S, Bogaerts A, Ejtehadi MR. Effect of cysteine oxidation in SARS-CoV-2 receptor-binding domain on its interaction with two cell receptors: Insights from atomistic simulations. Journal of chemical information and modeling. 2021;62(1):129-41.

[239]. Chang JW, Kang SU, Shin YS, Kim KI, Seo SJ, Yang SS, et al. Non-thermal atmospheric pressure plasma induces apoptosis in oral cavity squamous cell carcinoma: Involvement of DNA-damage-triggering sub-G1 arrest via the ATM/p53 pathway. Archives of biochemistry and biophysics. 2014;545:133-40.

[240]. Gross C, Schmidt-Wolf IG, Nagaraj S, Gastpar R, Ellwart J, Kunz-Schughart LA, et al. Heat shock protein 70-reactivity is associated with increased cell surface density of CD94/CD56 on primary natural killer cells. Cell stress & chaperones. 2003;8(4):348.

[241]. Yazdi M, Hasanzadeh Kafshgari M, Khademi Moghadam F, Zarezade V, Oellinger R, Khosravi M, et al. Crosstalk Between NK Cell Receptors and Tumor Membrane Hsp70-Derived Peptide: A Combined Computational and Experimental Study. Advanced Science. 2024;11(14):2305998.

[242]. Kim S-Y, Kim H-J, Kang SU, Kim YE, Park JK, Shin YS, et al. Non-thermal plasma induces AKT degradation through turn-on the MUL1 E3 ligase in head and neck cancer. Oncotarget. 2015;6(32):33382.

[243]. Gioanni J, Fischel J-L, Lambert J-C, Demard F, Mazeau C, Zanghellini E, et al. Two new human tumor cell lines derived from squamous cell carcinomas of the tongue: establishment, characterization and response to cytotoxic treatment. European Journal of Cancer and Clinical Oncology. 1988;24(9):1445-55.

[244]. Zhao M, Sano D, Pickering CR, Jasser SA, Henderson YC, Clayman GL, et al. Assembly and initial characterization of a panel of 85 genomically validated cell lines from diverse head and neck tumor sites. Clinical cancer research. 2011;17(23):7248-64.

[245]. Xavier FCA, Silva JC, Rodini CO, Rodrigues MFSD. Mechanisms of immune evasion by head and neck cancer stem cells. Frontiers in Oral Health. 2022;3:957310.

[246]. Horton JD, Knochelmann HM, Day TA, Paulos CM, Neskey DM. Immune evasion by head and neck cancer: foundations for combination therapy. Trends in cancer. 2019;5(4):208-32.

[247]. Knapp B, Ospina L, Deane CM. Avoiding false positive conclusions in molecular simulation: the importance of replicas. Journal of Chemical Theory and Computation. 2018;14(12):6127-38.

[248]. Brokaw RS. Predicting transport properties of dilute gases. Industrial & Engineering Chemistry Process Design and Development. 1969;8(2):240-53.

[249]. Smith GP, Golden DM, Frenklach M, Moriarty NW, Eiteneer B, Goldenberg M, et al. GRI-Mech 3.0 [Available from: www.me.berkeley.edu/gri_mech/.

[250]. Langenberg S, Carstens T, Hupperich D, Schweighoefer S, Schurath U. Determination of binary gas-phase diffusion coefficients of unstable and adsorbing atmospheric trace gases at low temperature–arrested flow and twin tube method. Atmospheric Chemistry and Physics. 2020;20(6):3669-82.

[251]. McBride BJ. NASA Glenn coefficients for calculating thermodynamic properties of individual species: National Aeronautics and Space Administration, John H. Glenn Research Center at Lewis Field; 2002.

[252]. Burcat A, Ruscic B. Third millenium ideal gas and condensed phase thermochemical database for combustion (with update from active thermochemical tables). Argonne National Lab.(ANL), Argonne, IL (United States); 2005.

[253]. Stiel LI, Thodos G. The thermal conductivity of nonpolar substances in the dense gaseous and liquid regions. AIChE Journal. 1964;10(1):26-30.

[254]. Kays WM. Turbulent Prandtl number. Where are we? ASME Journal of Heat Transfer. 1994;116(2):284-95.

[255]. Wise DL, Houghton G. The diffusion coefficients of ten slightly soluble gases in water at 10–60 C. Chem Eng Sci. 1966;21(11):999-1010.

[256]. Johnson PN, Davis RA. Diffusivity of ozone in water. Journal of Chemical & Engineering Data. 1996;41(6):1485-7.

[257]. Wise D, Houghton G. Diffusion coefficients of neon, krypton, xenon, carbon monoxide and nitric oxide in water at 10–60 C. Chem Eng Sci. 1968;23(10):1211-6.

List of publications

As first author

- **Heirman, P.**; Bogaerts, A. Critical comparison of interfacial boundary conditions in modelling plasma–liquid interaction. Journal of Physics D: Applied Physics 2024, 58, 085206. https://doi.org/10.1088/1361-6463/ad9c8f

- **Heirman, P.***; Verswyvel, H.*; Bauwens, M.; Yusupov, M.; De Waele, J.; Lin, A.; Smits, E.; Bogaerts, A. Effect of plasma-induced oxidation on NK cell immune checkpoint ligands: A computational-experimental approach. Redox Biology 2024, 77, 103381. https://doi.org/10.1016/j.redox.2024.103381

- **Heirman, P.**; Verloy, R.; Baroen, J.; Privat-Maldonado, A.; Smits, E.; Bogaerts, A. Liquid treatment with a plasma jet surrounded by a gas shield: effect of the treated substrate and gas shield geometry on the plasma effluent conditions. Journal of Physics D: Applied Physics 2023, 57, 115204. https://doi.org/10.1088/1361-6463/ad146b

- Clemen, R.*; **Heirman, P.***; Lin, A.; Bogaerts, A.; Bekeschus, S. Physical plasma-treated skin cancer cells amplify tumor cytotoxicity of human natural killer (NK) cells. Cancers 2020, 12, 3575. https://doi.org/10.3390/cancers12123575

- **Heirman, P.**; Van Boxem, W.; Bogaerts, A. Reactivity and stability of plasma-generated oxygen and nitrogen species in buffered water solution: a computational study. Physical Chemistry Chemical Physics 2019, 21, 12881-12894. https://doi.org/10.1039/C9CP00647H

(*) shared first author

As co-author

- Bissonnette-Dulude, J.; **Heirman, P.**; Coulombe, S.; Bogaerts, A.; Gervais, T.; Reuter, S. Coupling the COST reference plasma jet to a microfluidic device: a computational study. Plasma Sources Science and Technology 2024, 33, 015001. https://doi.org/10.1088/1361-6595/ad1421

Conference contributions

- Oral presentation: “Computational modelling of in vitro treatment with a plasma jet: elucidating the effects of the treatment setup”, at ICPM10/IWPCT9 (Portoroz, Slovenia, September 2024).
    - **Recipient of the ICPM10 Best Student Oral Presentation award**

- Oral presentation: “The effect of plasma-induced oxidation on the cancer – natural killer cell inhibitory axis: a computational-experimental approach”, at the PLASTHER COST Action 2nd annual meeting (Bologna, Italy, September 2023).

- Oral presentation: “Plasma-induced oxidation of the cancer – natural killer cell inhibitory axis: a computational-experimental approach”, at ISPC25 (Kyoto, Japan, May 2023).

- Poster presentation: “The efficacy of a gas shield in eliminating the effects of ambient conditions on the treatment of a liquid sample with a plasma jet”, at ISPC25 (Kyoto, Japan, May 2023).

- Poster presentation: “The effect of plasma-induced oxidation on the interaction of inhibitory NK cell receptors with their cancer cell ligands”, at CRF-ChemCYS (Blankenberge, Belgium, October 2022).
    - **3rd place for best poster presentation in the category “Chemistry Meets Biology”**


University
of Antwerp